

Kathrin Abstiens

**Heteromultivalent Nanoparticles for Selective Targeting of Renal
Cells**

Heteromultivalent Nanoparticles for Selective Targeting of Renal Cells

Dissertation zur Erlangung des Doktorgrades der
Naturwissenschaften
(Dr. rer. nat.)
der Fakultät für Chemie und Pharmazie
der Universität Regensburg



vorgelegt von
Kathrin Abstiens
aus Schwäbisch Gmünd

November 2018

Diese Arbeit entstand in der Zeit von November 2013 bis September 2017 am Lehrstuhl für Pharmazeutische Technologie der Universität Regensburg.

Die Arbeit wurde von Herrn Prof. Dr. Achim Göpferich angeleitet.

Promotionsgesuch eingereicht am: 30.11.2018

Tag der mündlichen Prüfung: 18.01.2019

Prüfungsausschuss:

- Prof. Dr. Jens Schlossmann (Vorsitzender)
- Prof. Dr. Achim Göpferich (Erstgutachter)
- Prof. Dr. Rainer Müller (Zweitgutachter)
- Prof. Dr. Frank-Michael Matysik (Drittprüfer)

Meiner Familie

Table of Contents

Heteromultivalent Nanoparticles for Selective Targeting of Renal Cells	1
Chapter 1 General Introduction	3
Chapter 2 Goals of the Thesis	19
Chapter 3 Microfluidic manufacturing improves polydispersity of multicomponent polymeric nanoparticles.....	23
Chapter 4 Interaction of functionalized nanoparticles with serum proteins and its impact on colloidal stability and cargo leaching	41
Chapter 5 Ligand density and linker length are critical factors for multivalent nanoparticle-receptor interactions.....	65
Chapter 6 Development and characterization of virus-mimetic heteromultivalent nanoparticles with enhanced selectivity towards mesangial cells.....	89
Chapter 7 Gold-tagged polymeric nanoparticles with spatially-controlled composition for enhanced detectability in biological environments.....	113
Chapter 8 Summary and Conclusion	133
References	139
Appendix	165
Supplementary Data.....	167
Abbreviation	175
Curriculum Vitae	179
List of Publications.....	181
Acknowledgements	183
Statement in Lieu of an Oath.....	185

Heteromultivalent Nanoparticles for Selective Targeting of Renal Cells

Es ist nicht genug zu wissen,
man muss es auch anwenden.

Es ist nicht genug zu wollen,
man muss es auch tun.

Johann Wolfgang von Goethe (1749-1832)

Chapter 1

General Introduction

1 Fundamental concepts of nanomedicine

1.1 Nanoparticle-based therapeutic systems

Nanomaterials have received growing attention as therapeutic systems due to their favorable pharmacokinetic and pharmacodynamic profiles [1-4] which are owed to their unique characteristics and their targeting capability. The increasing interest in the development of colloidal drug delivery systems is driven by the need for safer and more efficient therapeutics [5,6]. The use of conventional small-molecular drugs is often accompanied by undesired side effects deriving from their intrinsic toxicity and their non-specificity, which significantly limit their applicable dose and frequency of treatment [7,8]. In contrast, colloidal drug delivery systems provide essential advantages, such as improved drug solubility, controlled drug release, prolonged circulation times, reduced adverse effects and their potential to specifically target distinct tissues [1,9-11]. Nanoparticle-based therapeutic systems (Figure 1) are typically degradable, biodegradable or bioeliminable structures with a colloidal size up to 150 nm [12]. They can be loaded with a variety of payloads (e.g. small molecular drugs, peptides and proteins) which are usually entrapped within the particle core [13].

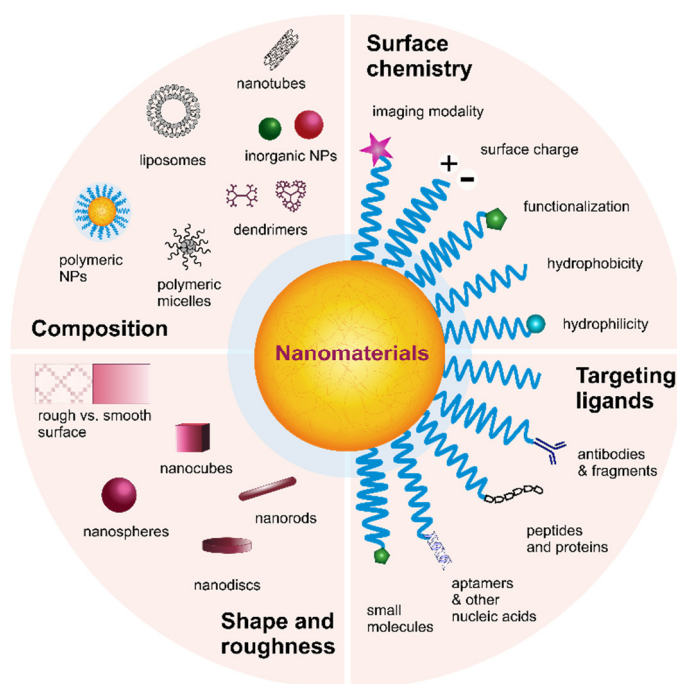


Figure 1. Parameters for the design of colloidal therapeutic systems. Adapted from [11].

An additional polymer shell can be used to endow nanocarriers with “stealth” properties and prolong their circulation time in the systemic blood stream [14,15]. Furthermore, these polymers can be functionalized with ligands or imaging modalities and can be used to control surface charge and hydrophobicity [11,16-18]. Their physicochemical properties, including composition, size, surface charge and chemistry, hydrophobicity or shape mainly determine their biodistribution and drug release profiles and have to be taken carefully into consideration for the development of nanoparticle-based therapeutic systems [19,20].

1.2 Biodistribution and pharmacokinetics of colloids

Upon intravenous administration, NPs enter the systemic blood circulation and are either excreted from the body *via* different clearance pathways or distributed to organs and peripheral tissues. NPs smaller than approximately 8 to 10 nm in size can pass the glomerular filtration barrier relatively unhindered and are rapidly removed from the blood *via* the urine [21-23]. In contrast, larger particles are subjected to biliary excretion and biodistribution into tissues [22,24,25]. Their circulation time in the blood stream mainly depends on the colloidal size and their ability to evade the reticuloendothelial system (RES) [11,26]. The RES, or mononuclear phagocyte system (MPS), consists of immune cells, including macrophages and monocytes, which are responsible for engulfing and eliminating pathogens, xenobiotic products or cell debris from the blood. Sequestration of NPs by these immune cells is mediated by presentation of distinct plasma complement factors and immunoglobulin proteins, also referred to as “opsonins” [27,28]. Upon entering the blood stream, numerous biomolecules instantly adsorb onto the colloidal surface forming a protein corona that bestows NPs with a new biological identity [29]. The identity and degree of opsonization is thereby dictated by physicochemical characteristics of colloids such as surface chemistry, material composition, size, charge, shape, hydrophobicity, or roughness [30-34]. For instance, larger particle sizes, correlating with larger radii of curvature, and a cationic surface charge favor opsonin adsorption and consequently enhance clearance by the RES [35]. To reduce recognition and uptake of colloids by immune cells of the RES it is essential to “stealth” NPs using highly hydrophilic antifouling polymers such as poly(ethylene glycol) (PEG) [26]. PEGylation significantly reduces adsorption of biomolecules and therefore, prolongs their circulation time which is considered a prerequisite for efficient accumulation of NPs in target tissues [14,15].

2 Targeting strategies

2.1 Passive tissue targeting

Passive targeting is widely exploited for the treatment of tumors because it facilitates accumulation of long-circulating NPs due to the pathophysiological differences compared to healthy tissues [36]. The basement membrane of pathological neovasculature is discontinuous or even absent, allowing macromolecules and NPs with a size smaller than 200 nm to extravasate and accumulate in the interstitium of the diseased tissue [37-40]. Furthermore, solid tumors lack a lymphatic system resulting in reduced drainage of accumulated colloids [38,41,42]. This ability of nanoscaled colloids to accumulate selectively and to be retained for a prolonged period of time in tumor tissue or other infarcted areas is commonly referred to as “enhanced permeation and retention” (EPR) effect [36]. As efficient EPR-mediated targeting requires a prolonged circulation half-life that allows time for NPs to passage from the systemic circulation into the diseased and permeable regions, passively targeted colloidal drug delivery systems are usually modified with hydrophilic polymers, such as PEG [15]. However, PEGylation at the same time, impedes endocytic uptake and endosomal escape of NPs in target cells, which consequently results in a significant loss in efficacy of the drug delivery system, also referred to as “PEG dilemma” [43,44]. Recent studies have indicated, that the EPR effect offers less than 2-fold increase in NP accumulation in the diseased tissue compared with critical healthy organs which often achieves no adequate dose for efficient therapeutic treatment [45].

2.2 Active tissue targeting

In contrast to passive targeting, which has been introduced in the previous section, active targeting relies on the affinity of ligands presented on the surface of long-circulating colloids for matrix proteins or antigen receptors expressed on target tissues [46]. The rationale for specific NP-cell interactions is based on significantly higher expression levels of antigenic receptors on the cellular membrane and the high specificity and high binding affinity of the ligand [11]. A general scheme of the active targeting concept is depicted in Figure 2. In the case of off-target cells, the receptor expression is low or even absent, impeding specific interactions with targeted colloids, whereas ligand-decorated NPs can specifically bind to the target receptors resulting in NP accumulation on the cellular membrane. Moreover, receptor-mediated targeting

can be used to trigger endocytosis into cells, which can enhance therapeutic efficacy as it can significantly increase intracellular concentration of drug carriers [47,48]. Internalized NP-receptor complexes end up in vesicles of endosomes, which progressively acidify and mature into late endosomes. Unless NPs are not able to escape the endosome, they will be subsequently degraded in lysosomes [49].

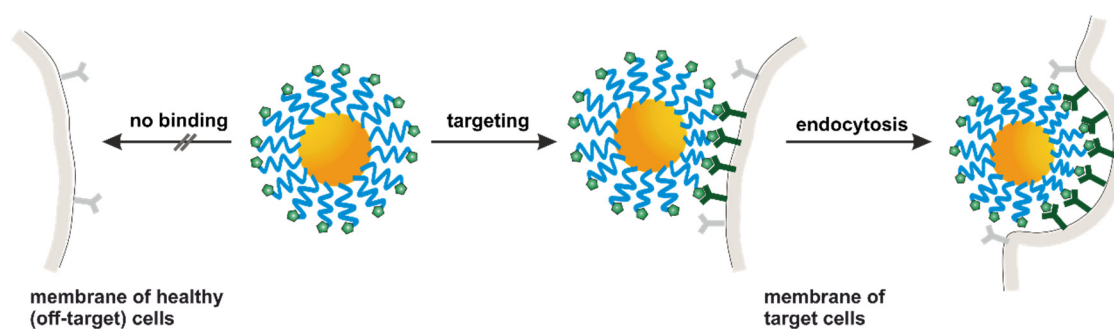


Figure 2. Schematic concept of active targeting using ligand-decorated NPs. Targeted NPs can selectively recognize and bind to their target cells followed by endocytosis. Concomitantly, interactions with off-target cells that express lower levels of the receptor can be minimized.

Active targeting can be further subdivided into homomultivalent, i.e., targeting using only a single type of ligand, and heteromultivalent targeting, i.e., targeting using multiple types of ligand which are simultaneously presented on a single particle. A complex example for heteromultivalent binding is the targeting sequence of viruses which often also includes time-dependent effects. All of these concepts will be introduced in the following sections.

2.2.1 Homomultivalent ligand presentation

In contrast to small molecular drugs, ligand-decorated NPs are capable of multivalent binding to their targets [50]. Multivalency describes simultaneous interactions of multiple ligands of one entity with multiple receptors of another one, which results in an increase in avidity compared to a single ligand-receptor interaction [51,52]. This mechanism can also be used to transform low-affinity monovalent ligands into a high-avidity multivalent construct [53]. A general obstacle originating from covalent ligand attachment is the considerable loss in binding affinity which can, on the one

Chapter 1: Introduction

hand, be attributed to steric hindrance deriving from the polymeric linker [54,55] or, on the other hand, be a result of chemical transformation of distinct functional groups that are peculiarly important for the interaction of the ligand with the complementary receptor binding-sites [56]. Therefore, multivalent ligand presentation can benefit from the avidity gain that was previously reported to overcompensate the loss in affinity deriving from ligand conjugation to PEG linkers [54].

Moreover, multivalency enhances selectivity towards the target site since multivalent binding requires a high receptor density, whereas the binding affinity is substantially alleviated with decreasing densities of the target receptor [57]. As a consequence, the intrinsic multivalent nature of colloids allows for discrimination between target surfaces with different receptor expression levels [58]. In the case of pathological tissues with upregulated receptor expression, the binding of multiligand-decorated NPs is enhanced while the interaction with healthy organs and cells expressing basal levels of the respective receptor is minimized [57,58]. For this reason, an adequate manufacturing process that allows for precise control over particle characteristics is key for the successful development of multivalent binding NPs. Pivotal design factors include the colloidal ligand density [59-61], the flexibility and length of the linker [62,63], and the size [64,65] of the particle that dictates the interfacial contact area.

Ligands that are employed for active targeting include a myriad of different synthetic and natural compounds including monoclonal antibodies (mAbs) and their fragments, proteins, peptides, aptamers, sugars and small molecular drugs [11,66].

Monoclonal antibodies are among the most commonly used targeting ligands and have been successfully utilized to enhance targeting efficiency of polymeric NPs. For example, decoration of NPs with rituximab and trastuzumab resulted in a 6-fold higher particle uptake compared to non-targeted NPs [67,68]. However, mAb-decorated NPs still encounter diverse challenges and limitations since antibodies show insufficient stability in organic solvents, are potentially immunogenic, severely affect surface hydrophobicity and “stealth” properties upon conjugation to the colloid, which enhances recognition by the RES and promote rapid NP clearance [69,70]. Moreover, due to their large size of approximately 150 kDa, corresponding to an average hydrodynamic size of about 15 nm, surface conjugation of mAb-moieties leads to a significant increase in overall colloidal size by up to 30 nm [47,71]. To overcome these limitations, antibody fragments, such as antigen-binding fragments and single chain variable fragments are preferably employed [72].

Many endogenous proteins can be used to accomplish selective binding to specific receptors on cell membranes, followed by receptor-mediated endocytosis. For example, the epidermal growth factor (EGF), which binds specifically to the EGF receptor, has been attached to different types of NPs for imaging or therapeutic purposes [73-75]. However, protein-decorated NPs suffer from severe drawbacks, such as an enhanced immunogenicity as well as a rapid clearance from the systemic circulation through several mechanisms in the body, which drastically limit their *in vivo* performance [11]. Moreover, cognate receptors are commonly expressed on healthy off-target tissues, increasing the chance of undesired side-effects [76].

Peptides have gained increasing popularity as targeting moieties because they are small in size, can be chemically synthesized and therefore, provide tailorable chemical functions which facilitate specific conjugation to polymers, lipids and colloids [77,78]. Moreover, peptides are significantly less immunogenic compared to proteins and possess a higher stability in both aqueous and organic solvents [79]. One of the most studied peptide sequences is Arg-Gly-Asp, also known as RGD, which targets $\alpha_v\beta_3$ integrin receptors highly upregulated in tumor cells or angiogenic endothelial cells [80-83]. However, $\alpha_v\beta_3$ integrin receptors are also expressed in normal tissues including endothelial cells of the healthy vascular system [11] or renal cells such as podocytes [84,85].

Aptamers are nucleic acid ligands [86] composed of either DNA, RNA or oligonucleotides folded into unique secondary structures which endows them with high specificity against their targets [87]. However, a change in this secondary structure due to heat or endonuclease and exonuclease degradation severely impairs their stability and targeting capability [88].

Small molecules constitute another class of targeting ligands. Due to their small size (< 1000 Da), high ligand densities can be obtained. Moreover, a wide range of different ligands are available possessing variable solubility and different functional groups that can be used for conjugation [17]. Their synthesis is scalable and requires less effort compared to e.g. the production of antibodies and moreover, they possess only low or even no immunogenic potential. For these reasons, small targeting molecules, such as folic acid [89,90] or methotrexate [91,92], which both target the folate receptor, have become a standard tool for targeted drug delivery systems.

2.2.2 Heteromultivalent ligand presentation

Owed to the massive increase in binding affinity, multivalent NPs can still interact with off-target tissues expressing lower levels of the complementary receptor if a certain density threshold is surpassed. Recent approaches have tried to overcome this limitation by simultaneous presentation of two different types of ligand [93-97].

Kluza and colleagues [97] prepared paramagnetic liposomes, decorated with cyclic RGD and angixin (Anx) for selective targeting of galectin-1 and $\alpha_v\beta_3$ integrin receptors, respectively. In contrast to their single-targeted counterparts decorated with either Anx- or RGD-ligands, dual-targeted liposomes displayed enhanced intracellular uptake and higher inhibitory effects for angiogenesis *in vitro*. In a further study by Kluza *et al.* [98], Anx/RGD-targeted liposomes were administered into melanoma-bearing mice. Interestingly, although the specificity for melanoma endothelium was increased, the tumor targeting efficacy of dual-targeted colloids was lower compared to liposomes decorated with RGD ligands which could be attributed to the cationic charge of Anx-ligands that facilitated recognition and clearance of dual targeted colloids. These findings emphasize that colloidal stability and clearance *in vivo* have great impact on the targeting efficacy of colloidal drug delivery systems.

Rangger and colleagues [99] constructed dual-targeted liposomes by combining RGD-ligands with substance P for concomitant targeting of $\alpha_v\beta_3$ integrins and neurokinin-a, respectively, aiming at increased specificity towards tumor tissue. Although the *in vitro* cellular uptake study displayed specific binding of single-targeted NPs towards two different cancer cell lines, decreased cellular binding was observed for heteromultivalent targeted liposomes. Moreover, *in vivo* biodistribution studies in an animal tumor model revealed only low accumulation in tumor xenografts using a dual-targeting approach. These results clearly demonstrate that the arrangement of two ligand types with regard to their densities and position play a pivotal role in synergistic targeting approaches and have to be optimized for each type of target.

These studies demonstrate that for the development of heteromultivalent targeted systems a variety of design parameters have to be considered to enhance targeting specificity and efficacy *in vivo*. These considerations particularly include an appropriate combination of ligands and optimized ligand densities on the colloidal surface, as well as a surface composition diminishing interactions with serum proteins

that potentially enhances NP clearance from the blood. Moreover, it is often overlooked that by involving multiple types of ligands also the number of off-target sites *in vivo* is increased. This is owed to the fact that circulating colloids can potentially encounter a higher number of cells or tissues that express only one of the respective target motifs but are earlier accessible than the target site.

2.2.3 Advanced targeting strategies of viruses

Viruses constitute prominent examples that have developed advanced strategies of recognizing and invading their host cells in a superselective fashion [100-102]. Virus binding to the cell surface and host cell entry is a highly orchestrated process that involves the consecutive binding of different receptor types, or even enzymatic on-site activation of a pro-ligand, followed by membrane fusion or receptor-mediated endocytosis [103-105].

For instance, the entry process of hepatitis C virus (HCV) requires a whole series of binding events to specific host factors [102,105,106]. The target cell is initially recognized through binding to two attachment factors: low-density lipoprotein receptors and glycosaminoglycans which are expressed on the basolateral surface of hepatocytes. The close proximity to the membrane allows the virus to subsequently bind to the four receptors scavenger receptor class B type I, tetraspanin CD81, the tight junction proteins claudin 1 and occludin followed by binding to several entry factors such as the EGF receptor, the ephrin receptor A2, the transferrin receptor 1 and cholesterol transporter Niemann-Pick C1-like 1.

Another prominent example is the influenza A virus [107,108], which possesses two envelope glycoproteins: hemagglutinin (HA) and neuraminidase (NA). While NA facilitates elution of virus replicates from the infected host cell, the trimeric glycoprotein HA serves as an anchor and mediates target cell adherence and virus entry in a unique fashion. The first step of target cell infection is the recognition of the target receptor molecule terminal α -sialic acid by HA [107]. Thereby, multivalent binding of HA moieties to multiple sialic acid receptors is mandatory to enable sufficiently tight attachment to the host membrane [109], because the monovalent interaction a single HA with sialic acid is known to be of low affinity [110]. In contrast, high-avidity binding of several receptor-ligand interactions results in strong binding of the virus particle to the host membrane. In a next step, HA must be cleaved by membrane-bound proteases to expose a distinct amino acid sequence that allows the

virus to fuse with the host membrane and enter the cytoplasm [111]. Cleavage of HA is a prerequisite for hijacking of host cells and serves as a checkpoint to confirm target cell identity [112]. For this reason, influenza A infection and replication in human is exclusively limited to the respiratory tract, since that is the only place where the respective protease is expressed.

Few studies have tried to transfer this advanced targeting strategy to colloidal drug delivery systems [113-116], yet the successful development of virus-mimicking NPs is still in its infancy.

3 The kidney as novel target for nanomedicines

NPs have been extensively investigated as therapeutic drug delivery systems aiming at specific targeting of diseased tissue sites. The majority of effort is dedicated to the development of nanoparticle-based therapeutic systems for cancer treatment due to the inherent tendency of NPs to accumulate in tumor tissues [1,22]. Although the kidney is severely affected in various diseases, such as diabetes mellitus [117], it has been largely overlooked as valuable target organ for NP-mediated drug delivery.

Diabetes mellitus has become one of the most common chronic diseases worldwide. Due to a change in lifestyle, e.g. low physical activity and increased obesity, the number of people suffering from this condition is expected to continuously raise [118]. Approximately one-third of all patients suffering from diabetes type 1 and 2 are affected by diabetic nephropathy (DN) [119], which has become the leading cause of end-stage renal disease (ESDR) and is predicted to become the seventh leading cause of death by 2030 [120,121]. Current therapies such as glycaemic control, blood pressure control and interception of the renin-angiotensin-aldosterone system (RAAS) aim at decelerating disease progression, however, the incidence of ESRD under therapy still remains unacceptably high [120]. For these reasons, there is a need for alternative therapeutic approaches with higher efficacy and fewer side effects. Targeted nanoparticle-based therapeutic systems would therefore be a valuable platform to improve treatment of various kidney diseases. However, due to the complex composition of the glomerular filtration barrier, colloids must possess distinct attributes that allows them to enter or transit distinct kidney areas [12,22].

3.1 Kidney anatomy and renal function

The kidneys are bean-shaped organs located at the posterior abdomen. They perform a variety of essential functions such as osmoregulation, maintenance of the fluid balance and secretion of hormones [12]. In addition, kidneys filter the plasma and thereby excrete metabolic waste products and toxins with the urine [122].

The functional unit of the kidney is the nephron. Each human kidney contains approximately one million nephrons [123]. The nephron is composed of a renal corpuscle and a hairpin shaped tubular system, consisting of the proximal convoluted tubule, the loop of Henle, a distal convoluted tubule and the collecting duct [122]. The renal corpuscle is composed of the glomerulus, a capillary tuft, and the Bowman's capsule that surrounds the glomerulus. The renal corpuscle comprises glomerular endothelial cells, a glomerular basement membrane (GBM), mesangial cells, podocytes and parietal epithelial cells [12,124]. Approximately 180 liters of plasma are filtered each day [125]. The primary urine is generated in the renal corpuscle by selective filtration of water, ions and small molecules from the blood and the filtrate is subsequently reabsorbed and concentrated in different sections of the tubule system to produce 1.5 liters of urine. The filtrate has a similar composition as plasma but is largely devoid of proteins due to the selective filtration of the glomerular barrier [125].

3.2 Components of the glomerular barrier

The glomerular filtration barrier has been intensively studied for decades, since it constitutes the most complex biological membrane being not only size- and but also charge-selective [125]. It is composed of three sequential layers that physically separate the vasculature from the urinary space and selectively filter blood components. These layers are (1) the glomerular endothelium [126], (2) the glomerular basement membrane (GBM) [127] and (3) podocytes with their foot processes [128] (Figure 3).

The glomerular endothelial cells form the capillaries within the glomerulus. They are unusually flattened with a height of 50 to 150 nm [125]. Moreover, they possess large fenestrated areas with a pore size of 50 to 100 nm [129], constituting 20 to 50% of the entire endothelial surface [130,131]. These fenestrations allow water and small solutes to pass unhindered from the vasculature into the glomerulus, but they effectively restrict the passage of blood cells [125]. Endothelial cells are coated by a negatively charged glycocalyx, consisting of proteoglycans and glycosaminoglycans, that restricts

Chapter 1: Introduction

negatively charged biomolecules (e.g. albumin) from entering the GBM by virtue of electrostatic repulsion [132].

The GBM is a 300 to 350 nm thick basal lamina which separates the endothelial from the epithelial layer [22]. It is mainly composed of type IV collagen and laminin, crosslinked with heparan sulfate and other charged proteoglycans such as agrin, perlecan and nidogen/entactin [22,125,133,134]. Due to its highly negative charge and the average pore size of 3 nm, the GBM selectively filters small molecules and colloids by their size and charge [135].

The third and outermost filtration barrier is represented by visceral epithelial cells also known as podocytes [136]. Podocytes and their extended foot processes enwrap the outer aspects of glomerular capillaries facing the urinary space [128,137]. Thereby, foot processes form filtration slits with an average width of 32 nm [22]. Adjacent foot processes are interconnected by a thin slit diaphragm, a specialized intercellular junction composed of unique membrane proteins (e.g. nephrin, podocin) and additional adherens junction proteins (e.g. P-cadherin) [138]. Both structures, podocyte foot processes and the slit diaphragm serve as the final filtration barrier that restricts proteins and macromolecules from reaching the urinary space.

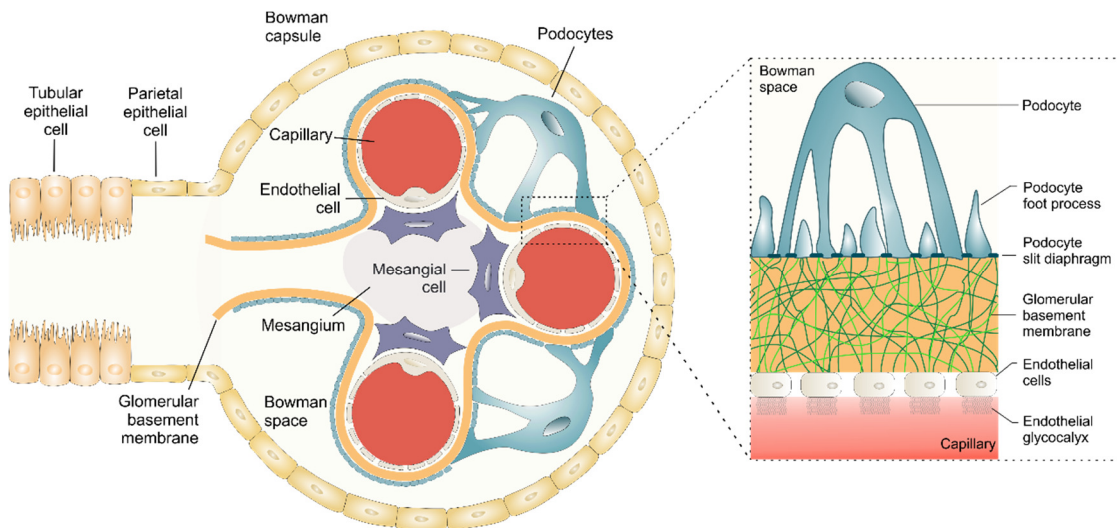


Figure 3. The kidney glomerulus and its filtration barrier consisting of the glomerular endothelium, the glomerular basement membrane (GBM), and podocytes with their foot processes and the slit diaphragm. Adapted from [12].

Although mesangial cells are not directly assigned to the glomerular filtration barrier, they are an essential part of glomerulus and mandatory to maintain its filter function [139]. Mesangial cells and their matrix provide substantial structural support for glomerular capillary loops [140]. Moreover, they are responsible for regulation of the filtration surface area and therefore are essential for the integrity of the renal filter [12,139]. Mesangial cells, podocytes and endothelial cells constitute a functional unit and communicate with each other *via* cytokine cross-talk [141]. Alteration in any of these three cell types can have severe impact on the others. For example, mesangial cell injury can result in podocyte foot process fusion and proteinuria, whereas podocyte injury can induce mesangial cell proliferation [139].

Impairment of either of these glomerular components can lead to proteinuria, which designates the presence of increased protein levels in the urine (> 300 mg in 24 hours) and constitutes a hallmark of glomerular diseases such as diabetic nephropathy [125].

3.3 Selective permeability

The overall effective size cutoff for molecules and colloids to pass the filtration barriers of the renal corpuscle and enter the urinary space is approximately 8 to 10 nm, referring to the hydrodynamic diameter [21-23]. Therefore, most of therapeutic colloids are not subject to kidney filtration as their size exceeds the size cutoff unless the filtration barrier is impaired by disease or particles are degraded into smaller fragments that fall below the kidney filtration threshold [12,22].

Colloids with a hydrodynamic diameter below 8 to 10 nm can pass the renal filter and are excreted into the urine [21-23]. In contrast, larger particles can enter the glomerulus from the afferent arteriole through the endothelial fenestrae, however their accumulation within the glomerulus is restricted to the mesangium and the extracellular matrix. Choi and colleagues [142] have recently investigated glomerular deposition of intravenously administered PEGylated gold NPs as a function of size. The total deposition of NPs below 100 nm was increased with larger particles size and was primarily controlled by NP uptake into mesangial cells, whereas larger particles (> 100 nm) were increasingly restricted from entering the mesangium due to the size limitation of endothelial fenestrations.

Charge selectivity is a second crucial parameter that influences the behavior of colloids within the glomerulus [125]. Choi and colleagues [142] have shown that anionic

Chapter 1: Introduction

PEGylated gold NPs do not deposit in the GBM or podocytes which could be attributed to the repulsive electrostatic forces of the negatively charged GBM. In contrast, positively charged polymer-based siRNA NPs of the same size (80 nm) were reported to accumulate within the GBM and the mesangium [143]. These findings were supported by Bennett *et al.* [144] who demonstrated that cationic ferritin-decorated NPs accumulate in the GBM after intravenous injection in rats. However, the concept of charge selectivity remains highly controversial. Kodaira and colleagues [145] found that negatively charged polyvinylpyrrolidone (PVP) derivatives could accumulate in the glomerulus after systemic administration. Paradoxically, a more pronounced negative charge of carboxylated PVP colloids resulted in enhanced accumulation in the kidney, with renal levels reaching approximately 30% of the administered dose. Interestingly, sulfonated PVP NPs could pass the glomerular filtration barrier and were rapidly excreted in the urine.

Another criterion for kidney filtration is particle geometry. Carbon nanotubes with high aspect ratios have been shown to paradoxically being filtered by the glomerulus [22,146,147] despite their average length of 100 to 500 nm, which exceeds the renal filtration threshold by a factor of 10 to 50. Ruggiero *et al.* [147] concluded that the long axis of single-walled carbon nanotubes was coordinated perpendicular to the GBM through hydrostatic forces, thereby orienting their short axis into the pores of the GBM. These results were further confirmed by Lacerda and colleagues [146] who used transmission electron microscopy (TEM) to demonstrate that the orientation of carbon nanotubes within the glomerulus corresponded to the predicted model.

The filtration threshold can be influenced by further particle characteristics including tensile strength and young's modulus which are primarily dictated by the NP composition. The role of flexibility on renal clearance was investigated using dendrimers possessing different degrees of intramolecular flexibility. Soft and flexible dendrimers with a hydrodynamic size of 18 nm showed renal excretion, whereas dendrimers with a rather rigid core but smaller size could not pass the glomerular filtration barrier [148-150].

In summary, particle size, surface charge, shape, and flexibility are all major determinants of NP deposition within the glomerulus. However, permeability restrictions only apply for healthy tissues and can be greatly altered in a diseased state.

3.4 Pathophysiological changes in diabetic nephropathy and targeting opportunities

DN constitutes a life-threatening complication and affects one-third of all patients suffering from diabetes [119]. Pathophysiological changes in DN progress rapidly and severely affect components of the glomerular filtration barrier [119]. For example, the thickness of the GBM increases by about 30% [151] and further worsens during disease progression. The number of podocytes is drastically reduced and podocytes start to detach from the GBM, leading to a loss of foot process and fusion [152]. Mesangial cells start to change their gene expression [153] and are also subject to cell proliferation and hypertrophy [140]. The relative increase in volume of the mesangium drastically impairs other structures within the glomerulus, resulting in reduction of the glomerular filtration area and segmental occlusion of glomerular capillaries [125]. Because pathological changes in the mesangium are among the earliest and most critical events found in DN [140], it would be highly beneficial to consider mesangial cells as therapeutic target for the treatment of renal diseases [154].

Due to the fact that mesangial cells are separated from the systemic blood stream only by fenestrated endothelial cells, they are accessible for colloids that fall below the endothelial pore size of 50 to 100 nm [129]. As aforementioned, recent studies have demonstrated that colloids can enter the mesangium *via* size-selective passive targeting which is similar to the EPR effect. For example, Choi and colleagues [142] found that PEGylated gold NPs with a size of 50 to 100 nm accumulated in the mesangium and were partly internalized by mesangial cells within 24 hours after intravenous injection, whereas larger particles (> 100 nm) were not able to access the mesangium due to steric restrictions at the endothelial fenestrations. In a different study by Pollinger and coworkers [155], it was demonstrated that PEGylated quantum dots (Qdots) with a hydrodynamic diameter of approximately 20 nm and distinct negative charge (-14.5 to -15.6 mV) displayed pronounced enrichment in the mesangium of healthy mice one hour after systemic administration. Although these studies provide important information about glomerular deposition of colloids as a function of their attributes (i.e. size), these inorganic nanomaterials are not suited as drug delivery system as their solid cores cannot be loaded with therapeutic drugs. Recently, Li and coworkers [156] combined the advantages of polymeric NPs and the size selectivity of renal glomerulus. To this end, they prepared dexamethasone acetate-loaded polymeric NPs which were injected into healthy rats. They found that drug-loaded polymeric NPs with a

Chapter 1: Introduction

hydrodynamic size of 90 nm accumulated in the kidney to a greater extent than free DiD solution. Thereby, drug-loaded NPs were primarily deposited within the glomerular mesangium.

These studies emphasize the feasibility of nanomedicines to target the mesangium, however, they exclusively rely on passive targeting strategies. Multivalent targeting would be the perfect strategy to enhance target selectivity and, in addition, trigger uptake into renal cells by receptor-mediated endocytosis. Scindia and colleagues [157] have used anti- α_8 -integrin ligands to enhance glomerular deposition of liposomal nanocarriers with a size of 70 to 130 nm in lupus glomerulonephritis susceptible mice. In contrast to control immunoglobulin-decorated liposomes, targeted colloids were capable of specific accumulation in the mesangium of diseased mice.

Furthermore, receptor expression of glomerular cells can be altered in a diseased state providing a promising opportunity for selective targeting. For example, $\alpha_v\beta_3$ integrin receptors are increasingly expressed on mesangial cells during the progression of diabetic nephropathy [158,159], whereas E-selectin expression in endothelial cells is upregulated at the onset of glomerulonephritis [160].

Biodegradable polymeric NPs constitute the ideal system for multivalent targeting of mesangial cells because they possess highly tunable physicochemical properties, which allows for exact tailoring of NP size, they can be modified with multiple targeting ligands of defined density, and provide the capacity to accommodate high amounts of hydrophobic drugs inside their colloidal core [10,11].

4 Conclusion

Multivalent NPs have shown tremendous potential for selective targeting because they can accumulate at target sites while sparing healthy off-target tissues. Although the kidney is severely affected in various diseases, such as diabetes mellitus, it has largely been overlooked as target for NP-mediated therapeutic intervention. In the diseased state, the renal filter integrity is severely impaired, allowing colloids to enter or even transit the glomerular filtration barrier. Precise tailoring of NP characteristics in terms of kidney retention and binding to distinct cell populations which are affected during disease progression (i.e. mesangial cells) can be exploited to develop novel therapeutic approaches for the treatment of renal diseases.

Chapter 2

Goals of the Thesis

Chapter 2: Goals of the Thesis

Maximizing drug concentration at the site of disease while minimizing systemic drug effects is regarded the ideal conception for pharmacotherapy. This is of particular importance when the therapeutic target is confined to a defined tissue which is the case for various cancers, vitreoretinal diseases or diabetic nephropathy. Targeted drug delivery is widely regarded the most potent tool to make this vision come true. In particular, polymeric nanoparticles (NPs) have tremendous potential for targeted delivery as they are biocompatible, degradable, possess unique and highly tunable physicochemical properties and can be loaded with high amounts of cargo.

As they provide extremely high flexibility in their design, polymeric NPs can be precisely engineered to suit a wide range of therapeutic applications. Although polymeric NPs possess tremendous potential, their bench to bedside transition proceeds slowly. This is attributed to several limiting factors such as: (1) lack of manufacturing platforms that allow for a controlled and scalable synthesis of NPs with high batch-to-batch consistency, (2) inadequate knowledge of events at the nano-bio interface both *in vitro* and *in vivo*, (3) the limited understanding of their fate in the body, organs and at cellular levels due to their poor detectability in tissues and biological media, (4) incomplete knowledge of critical particle attributes with regards to targeting, and (5) insufficient selectivity and efficiency of targeted NPs *in vivo*.

The aim of this work was to design and characterize core/shell structured multivalent polymeric NPs intended for selective targeting of mesangial cells with special focus on addressing the abovementioned challenges.

Development of therapeutic colloids intended for selective targeting requires the precise control of NP attributes. Particle size is widely considered a key factor since it determines the interfacial contact area and therefore, has a major impact on multivalent binding to target cells. Moreover, with respect to targeting of kidney cells, size also constitutes a restricting parameter in terms of glomerular entrance. In **Chapter 3**, microfluidic synthesis of multicomponent polymeric colloids was evaluated and compared to bulk nanoprecipitation, which is considered the gold standard in the field. Three NP formulations with varying core to shell ratios were optimized by adjusting critical process and formulation parameters and the influence on particle size and size distribution was investigated and analyzed by dynamic light scattering and transmission electron microscopy.

A profound understanding of NP behavior at the nano-bio interface is essential for the design of therapeutic systems. Adsorption of serum proteins onto the colloidal surface can substantially enhance recognition and clearance of NPs by the reticuloendothelial system. Moreover, formation of a protein corona can severely impair colloidal stability and therefore, has a major impact on the *in vivo* performance of colloidal drug delivery systems. To gain a better understanding of the nano-bio interface, the interaction of functionalized NPs with serum proteins was systematically studied as a function of surface charge and hydrophobicity. Moreover, the impact of protein corona formation on NP integrity was assessed (**Chapter 4**).

Surface functionalization with high-affinity ligands is commonly considered the major determinant for controlling the uptake efficiency *in vitro* and *in vivo*. However, it is often not sufficiently taken into consideration that cellular uptake of targeted colloids is governed by a delicate interplay between different particle features. In **Chapter 5**, the combinational influence of cRGD ligand density and poly(ethylene glycol) (PEG) linker length on NP uptake into $\alpha_v\beta_3$ integrin overexpressing U87MG glioblastoma cells was investigated by flow cytometry and fluorescence microscopy.

The therapeutic concept of targeted drug delivery systems relies on the specific interaction of targeting ligands presented on the colloidal surface with cognate receptors of the target cell. However, cell surface receptors are not exclusively located on target cells but can also be expressed by healthy off-target tissues. To overcome premature NP uptake into off-target cells and minimize systemic toxicity, new targeting strategies with enhance selectivity towards target cells are needed. Inspired by viruses, which are capable of sequential recognition and entry of their host cells, heteromultivalent binding NPs were designed. The advanced specificity of virus mimicking dual-targeted NPs towards rat mesangial cells, which are affected in a number of severe renal diseases, was assessed by flow cytometry and fluorescence microscopy (**Chapter 6**).

Polymeric NPs suffer from poor visibility in biological environments. Reliable and simultaneous qualitative and quantitative detectability in cells and tissues is a largely unmet need. Because profound knowledge of pharmacokinetics and biodistribution are key to the successful development of nanomedicines, additional labels are required to evaluate their *in vivo* performance and track their journey from the point of administration to the target site. To overcome this limitation, small gold tags were introduced as a contrast agent at the core/shell interface of polymeric NPs and

Chapter 2: Goals of the Thesis

polymer/gold hybrid NPs were characterized for their physicochemical characteristics and their toxicity *in vitro*. Moreover, the enhanced detectability in cells was evaluated by fluorescence and transmission electron microscopy (**Chapter 7**).

**Microfluidic manufacturing improves
polydispersity of multicomponent polymeric
nanoparticles**

Abstract

A key challenge in manufacturing of multicomponent polymeric colloids is obtaining monodisperse nanoparticles (NPs) with reproducible characteristics. Herein, NP formulations with varying core to shell ratios consisting of different poly(lactic acid)-poly(ethylene glycol) (PLA-PEG) copolymers (10k-b-5k, 15k-b-5k, 20k-b-5k) and poly(lactic-*co*-glycolic acid) (PLGA) at varying copolymer mass ratios (70/30, 65/35 or 60/40) were either prepared by bulk nanoprecipitation or microfluidic synthesis and evaluated regarding their size and polydispersity. Microfluidic process parameters, such as the total flow rate (TFR) and the flow rate ratio (FRR) of the aqueous phase and the organic polymer solution, were varied to tune particle size and further improve size distribution. Z-average hydrodynamic diameter and polydispersity index (PDI) were analyzed by dynamic light scattering (DLS) and selected formulations were further examined by transmission electron microscopy (TEM). In general, bulk nanoprecipitation resulted in formation of larger particles (52 - 65 nm) with a wide size distribution, whereas particles were significantly smaller in size (24 - 43 nm) and displayed a rather monodisperse size distribution when they were manufactured with a microfluidic system. The FRR was identified to be the key factor for improving the size distribution of NPs with a high ratio of PLA-PEG to PLGA, whereas it had only minor impact on particle characteristics of formulations with a lower copolymer ratio. Polydispersity of different NP formulations was successfully improved by microfluidic manufacturing, demonstrating that this technology is a valuable tool that allows for reproducible and scalable manufacturing of multicomponent NPs with precisely tunable quality attributes.

1 Introduction

The use of core/shell structured nanoparticles (NPs) as drug delivery system holds tremendous promise for improving the treatment of several diseases in terms of therapeutic efficacy and reduced side effects [161]. Especially, biocompatible and biodegradable NPs composed of poly(lactic acid)-poly(ethylene glycol) (PLA-PEG) and poly(lactic-co-glycolic acid) (PLGA) have gained enormous attention since they provide the possibility to combine various useful features such as hosting high amounts of hardly soluble drugs, controlled drug release with tunable release profiles and specific receptor targeting [162-164]. Different block copolymers are often combined to optimize NP composition and engineer their characteristics, such as particle size, charge, surface functionalization or the core to shell ratio [60,61]. A fast and simple technology to prepare PLGA-blended PLA-PEG nanoparticles is bulk nanoprecipitation by solvent exchange [165], which involves dropwise addition of a water-miscible organic polymer solution to a larger quantity of an aqueous non-solvent under stirring. As a consequence of diffusion, the solvent is exchanged leading to interfacial deposition of hydrophobic or amphiphilic polymers and self-assembling into core/shell structured NPs in order to reduce the free energy of the system [11,166]. However, in a bulk nanoprecipitation approach, phase mixing proceeds slowly and uncontrolled, which favors formation of hetero-sized nanocolloids due to the unequal distribution of polymer blocks and consequently, results in an insufficient batch-to-batch consistency. Hence, precise engineering, optimization and testing of core-blended NPs is severely impaired. As the *in vivo* performance of NPs strongly depends on their physicochemical characteristics it is crucial to enhance the reproducibility and controllability of NP synthesis [11,167,168]. Microfluidics has recently emerged as a new technology that offers precisely controlled reaction environments and has been harnessed to manufacture polymeric NPs with defined properties and excellent batch-to-batch consistency [61,168]. Furthermore, microfluidics can tackle the limited options provided by bulk nanoprecipitation for down- and up-scaling which makes this technology highly valuable for high-throughput screenings during the development of new nanomedicines as well as for clinical applications, where sufficient quantities of NPs with consistent properties are needed [61,169]. For these reasons, microfluidics was considered as an ideal platform to optimize size distribution of multicomponent polymeric NPs with distinct core to shell ratios. In this study, three NP formulations composed of PLA-PEG

Chapter 3: Microfluidic manufacturing of multicomponent nanoparticles

copolymers with increasing molecular weights of the PLA block (10k-b-5k, 15k-b-5k, 20k-b-5k) and varying PLA-PEG to PLGA copolymer mass ratios (70/30, 65/35 or 60/40) were prepared by bulk nanoprecipitation and microfluidic synthesis. Blends of PLGA and PLA-PEG copolymers were used to control the ratio between the hydrophilic PEG shell and the hydrophobic PLA/PLGA core of polymeric NPs. Optimization of these NP formulations was proceeded by adjusting process and formulation parameters and the influence of copolymer concentration, total flow rate (TFR) and the flow rate ratio (FRR) of aqueous to organic phase on particle size and size distribution was investigated and analyzed by dynamic light scattering (DLS) and transmission electron microscopy (TEM).

2 Materials and methods

2.1 Materials

1,8-Diazabicyclo[5.4.0]undec-7-ene (DBU) solution, 3,6-Dimethyl-1,4-dioxane-2,5-dione (Lactide), 3-(Trimethylsilyl)propionic-2,2,3,3-d₄ acid sodium salt (TMS⁺P), anhydrous dichloromethane (DCM), anhydrous ethyl acetate, deuterated chloroform (CDCl₃), deuterium oxide (D₂O), methoxy poly(ethylene glycol) with a molecular mass of 5000 g mol⁻¹ (MeO-PEG5k-OH), Resomer® RG 502 (PLGA) and Tetramethylsilane (TMS) were received from Sigma-Aldrich (Taufkirchen, Germany). All other materials were reagent grade and obtained from Merck KGaA (Darmstadt, Germany). Ultrapure water was obtained by using a Milli-Q water purification system (Millipore, Schwalbach, Germany).

2.2 Synthesis of functionalized PLA-PEG block copolymers

Poly(lactic acid)-poly(ethylene glycol) (PLA-PEG) block copolymers with different polymerization degrees of the PLA block (10k-b-5k, 15k-b-5k, 20k-b-5k) were synthesized by ring-opening polymerization as previously described by Qian *et al.* [170] with slight modifications. Prior to use, racemic 3,6-dimethyl-1,4-dioxane-2,5-dione (*D,L*-lactide) was purified by recrystallization from anhydrous ethyl acetate and dried under vacuum for at least 12 h. Linear methoxy poly(ethylene glycol) with a molecular mass of 5000 g mol⁻¹ was used as macroinitiator for the ring-opening polymerization of lactide using DBU as catalyst. After quenching the polymerization reaction with benzoic acid, block copolymers were subsequently precipitated in diethyl

ether and dried under vacuum at 45 °C overnight. ¹H-NMR spectra were recorded in CDCl₃ at 295 K using a Bruker Avance 300 spectrometer (Bruker BioSpin GmbH, Rheinstetten, Germany). The number-average molecular weight of PLA-PEG block copolymers was determined by integration of the methylene signal of PEG residues based on molecular weight (provided by the manufacturer) and calculation of the methine and methylene proton signals of PLA.

2.3 Bulk nanoprecipitation of nanoparticles

Polymeric NPs were prepared by bulk nanoprecipitation as previously described [165]. In general, PLA-PEG and PLGA were diluted with acetonitrile to a final polymer concentration of 5, 10 or 20 mg mL⁻¹. The polymerization degree of the PLA-PEG copolymer (10k-b-5k, 15k-b-5k, 20-b-5k) as well as the mass ratio of PLA-PEG to PLGA (70:30, 65:35 or 60:40) was varied depending on the NP formulation. A detailed description of the respective NP compositions with either high (NP510m), medium (NP515m) or low PEG content (NP520m) is given in Figure 1. The polymer solution was added dropwise into 10 volumes of stirred ultrapure water and NP dispersions were stirred for 3 hours to evaporate the organic solvent. NPs were filtered through a 0.45 μM Rotilabo® PES syringe filters (Carl Roth, Karlsruhe Germany) and concentrated by ultrafiltration using Pall Macrosep® Advance Centrifugal Devices (Pall GmbH, Dreieich, Germany) with 100 kDa MWCO.

2.4 Microfluidic synthesis of nanoparticles

Polymeric NPs were also prepared *via* microfluidics using a benchtop NanoAssemblr™ instrument (NanoAssemblr™, Precision NanoSystems Inc., Vancouver, Canada) and process parameters were controlled using the corresponding NanoAssemblr™ Controller software (v1.0.5). Ultrapure water was injected into the first inlet and the organic polymer solution in the second inlet of the microfluidic mixer. The TFR was varied from 2 to 17 mL min⁻¹ and the FRR of the aqueous phase and the organic polymer solution was either 10:1 or 5:1. NP formulations were collected at the outlet channel and stirred for 1 h to remove the organic solvent. Afterwards, NP dispersions were filtered through 0.45 μM Rotilabo® PES syringe filters (Carl Roth, Karlsruhe Germany).

2.5 PEG quantification

The PEG content was determined by $^1\text{H-NMR}$ spectroscopy according to a method described by Bertrand *et al.* [171] with slight modifications. To determine the total PEG content in NP formulations, NP510m, NP515m and NP520m were prepared in ultrapure water and 600 μL of the concentrated solutions (approx. 4 to 5 mg mL^{-1}) were lyophilized for 48 h. The exact NP mass of each sample was determined gravimetrically ($n=3$) and samples were subsequently dissolved in 600 μL of CDCl_3 containing 0.05% (v/v) TMS as an internal standard. Solutions of MeO-PEG5k-OH at defined concentrations (0.1-5.0 mg mL^{-1}) in CDCl_3 containing 0.05% (v/v) TMS were used for calibration. Methylene protons of PEG (3.65 ppm) were normalized to the proton signal of the internal standard (TMS) and used for calculation of the PEG concentration in respective samples. To determine the concentration of hydrated PEG in the NP shell, NP510m, NP515m and NP520m were prepared in ultrapure water and the solvent was exchanged with D_2O supplemented with 0.05% (m/v) TMSP as an internal standard using Microsep® Advance Centrifugal Devices (Pall GmbH, Dreieich, Germany) with 100 kDa MWCO. The exact polymer concentration of samples in D_2O was determined gravimetrically after lyophilization ($n=3$). The ratio of the methylene protons of PEG (3.72 ppm) to the integral of the methyl protons of the internal standard (TMSP) was then compared with the calibration curve of MeO-PEG5k-OH (0.1 - 5.0 mg mL^{-1}) in D_2O to calculate the PEG content in the NP shell. All measurements were conducted on a Bruker Avance 300 spectrometer (Bruker BioSpin GmbH, Rheinstetten, Germany) at 295 K.

2.6 Dynamic Light Scattering

Z-average hydrodynamic size and polydispersity index (PDI) of NP formulations were determined on a Zetasizer Nano ZS device (Malvern, Herrenberg, Germany). DLS measurements were performed in ultrapure water at a constant temperature of 25 $^\circ\text{C}$ using semi-micro PMMA disposable cuvettes (Brand, Wertheim, Germany). The position from the cuvette wall was set to 4.65 mm and the attenuator was optimized by the device. Data were collected and analyzed using the Malvern Zetasizer software version 7.11 (Malvern Instruments, Worcestershire, United Kingdom).

2.7 Transmission Electron Microscopy

The particle size, size distribution and morphology of selected NP formulations was evaluated on a Zeiss 902 (80 kV) transmission electron microscope (Zeiss, Oberkochen, Germany). NP samples were applied onto carbon-coated copper grids (300 mesh; Plano, Wetzlar, Germany), incubated for 5 minutes and negatively stained with a 1% uranyl acetate solution. Excess sample solution was removed with a filter paper and sample grids were dried and stored in a desiccator before use.

2.8 Statistical analysis

All results are presented as mean \pm standard deviation, based on the data obtained from at least $n = 3$ samples unless stated otherwise. Statistical significance was determined by means of one-way ANOVA, followed by Tukey's *post-hoc* test using GraphPad Prism 6.0 (GraphPad Software Inc., La Jolla, CA, USA). Statistical significances were set as indicated.

3 Results and discussion

3.1 PEG content quantification

Blending the NP core of polymeric PLA-PEG micelles with additional PLGA does not only stabilize the NP core by enhancing the hydrophobic interactions [172,173], but also allows for precise tuning of the core to shell ratio [171,174]. However, size and size distribution of a NP formulation are strongly affected by the formulation composition and the manufacturing process.

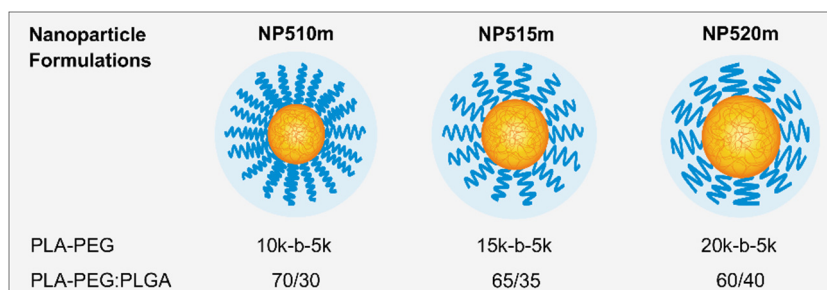


Figure 1. Composition of NP formulations that were used for this study. The core to shell ratio was varied by mixing PLA-PEG with increasing PLA block lengths (10k, 15k, 20k) and PLGA at different copolymer mass ratios (70/30, 65/35, 60/40).

Chapter 3: Microfluidic manufacturing of multicomponent nanoparticles

In this study, three NP formulations with different core to shell ratios were prepared by bulk nanoprecipitation and microfluidic manufacturing and evaluated for their critical quality attributes, such as particle size, size distribution and morphology. To this end, PLA-PEG copolymers with constant PEG block lengths and increasing polymerization degrees of the PLA block (10k-b-5k, 15k-b-5k, 20k-b-5k) were blended with PLGA at different mass ratios of PLA-PEG to PLGA (70/30, 65/35, 60/40) to generate particles with high (23.8%), medium (16.7%) and low (12.1%) PEG content, referring to as NP510m, NP515m and NP520m, respectively (Figure 1).

^1H -NMR spectroscopy was used to quantify the PEG content in each NP formulation and determine the fraction of PEG that was hydrated in the PEG shell (Figure 2). NPs were either dissolved in CDCl_3 , to determine the total amount of PEG, or, dispersed in D_2O , to quantify the PEG fraction that was hydrated in the shell and therefore, accessible for D_2O molecules. As shown in Figure 2A, the integral of methylene protons as determined by ^1H -NMR directly correlated with the PEG concentration of the calibration standard prepared in either D_2O or CDCl_3 with R^2 of the linear regression being 1.0000 and 0.9997, respectively.

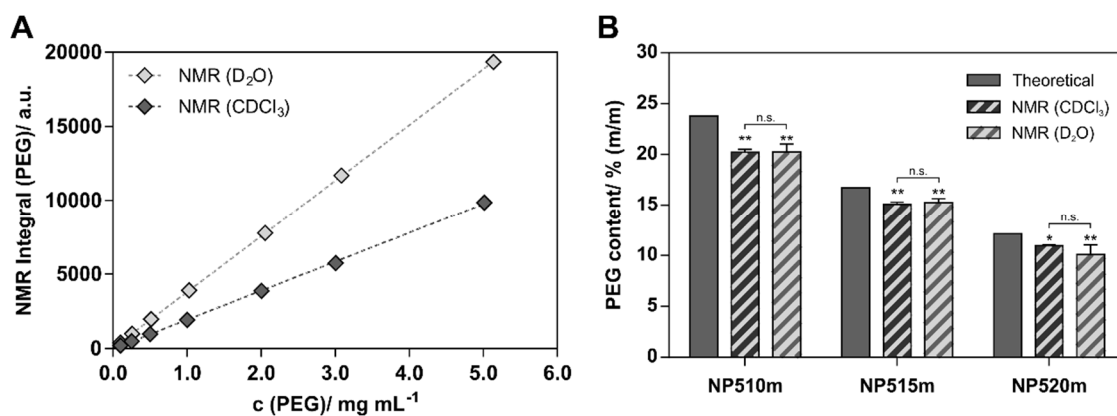


Figure 2. PEG content quantification by ^1H -NMR. (A) Solutions of MeO-PEG5k-OH were used to determine the correlation of PEG concentration and the integral of the methylene protons in either D_2O or CDCl_3 . (B) The absolute PEG content (CDCl_3) as well as the amount of hydrated PEG in the shell (D_2O) were calculated and compared to the PEG contents determined by calculation based on the NP composition and the molecular weights of the block copolymers. Levels of significance are indicated as: (**) $p < 0.01$ and (*) $p < 0.05$, compared to the theoretical PEG content.

PEG contents of all NP formulations assessed by $^1\text{H-NMR}$ were significantly ($p < 0.01$ or $p < 0.05$ as indicated) decreased compared to calculated values, indicating that the fraction of PLA-PEG that is not firmly anchored in PLGA blended NPs is removed during the purification process. As PEG contents of NP samples dispersed in D_2O and dissolved in CDCl_3 were comparable and did not show any significant differences, it can be concluded that the complete fraction of PEG is solvated in the outside shell of the NPs (Figure 2B). These results demonstrate, that composition and core to shell ratio can be controlled by the copolymer mass ratio and the PLA polymerization degree.

3.2 Correlation of process parameters and particle characteristics

To date, polymeric NPs consisting of amphiphilic copolymers are commonly prepared by addition of the respective polymers dissolved in a water miscible organic solvent into an aqueous non-solvent, leading to gradual solvent displacement and subsequent solidification of interfacial deposited polymers. However, when different copolymers, such as amphiphilic PLA-PEG and hydrophobic PLGA, are combined to modify the NP composition, manufacturing by bulk nanoprecipitation does not offer the possibility to precisely control the mixing processes, consequently resulting in insufficient batch-to-batch consistency and moreover, a high polydispersity of PLGA/PLA-PEG colloids due to an unequal distribution of hydrophobic PLGA. In contrast, microfluidic manufacturing provides a promising tool for the controlled synthesis of multicomponent polymeric NPs as it enables a rapid and tunable mixing of both fluids in a microfluidic channel.

In this study, NPs were prepared with a benchtop NanoAssemblrTM instrument (NanoAssemblrTM, Precision Nanosystems Inc, Vancouver, Canada) using commercially available micromixer chips that were featured with additional herringbone structures (Figure 3). These staggered herringbone structures located in the microfluidic mixing channel are known to induce chaotic advection of the fluid streams even at lower Reynold numbers ($\text{Re} < 100$), resulting in a decreased average diffusion distance necessary to homogenize unmixed volumes [175,176]. Ultrapure water was injected into the first inlet and the organic polymer solution in the second inlet of the microfluidic mixer and NP formulations were prepared by changing the critical process and formulation parameters as depicted in Figure 3.

Chapter 3: Microfluidic manufacturing of multicomponent nanoparticles

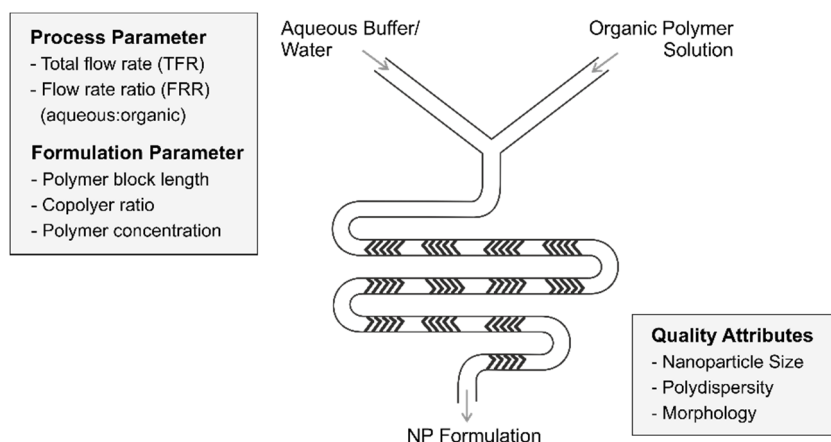


Figure 3. Schematic depiction of the microfluidic process. Polymers dissolved in an organic solvent (ACN) and an aqueous buffer are injected into separate inlet channels. The two fluid streams are thoroughly mixed in the mixing channel which possesses multiple herringbone structures to enhance chaotic advection between both streams and initiate nanoprecipitation. Process and formulation parameters were continuously varied and the resulting NP formulations were evaluated for their critical quality attributes.

In a first experiment, NP510m were prepared by either bulk nanoprecipitation or microfluidic synthesis and critical parameters, such as the copolymer concentration (5 - 20 mg mL⁻¹), TFR (2 - 17 mL min⁻¹) and FRR of the aqueous to the organic phase (10:1, 5:1) were varied in order to evaluate their influence on particle size and size distribution of the obtained NP formulations.

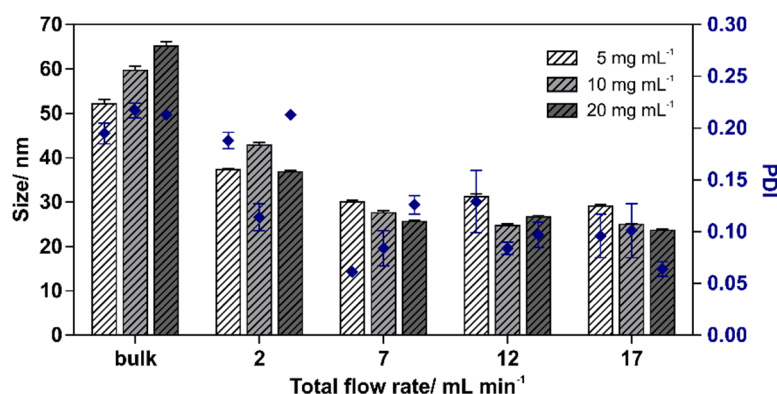


Figure 4. Size and size distribution of NP510m as a function of polymer concentration and total flow rate at a constant FRR of 10 to 1 of the aqueous to the organic phase. NPs were additionally prepared by bulk nanoprecipitation at an aqueous to organic phase ratio of 10 to 1.

Results and discussion

By using higher overall polymer concentrations, the volume of NPs prepared by bulk nanoprecipitation increased by a factor of 1.5 (10 mg mL^{-1}) and 1.9 (20 mg mL^{-1}) compared to NPs prepared from a 5 mg mL^{-1} polymer solution, which is much less than the concentration difference by a factor of 2 and 4, respectively (Figure 4). In contrast, when NPs were manufactured with the microfluidic system, differences between high and low concentrations vanished or even displayed reversed correlations at higher flow rates ($7 - 17 \text{ mL min}^{-1}$).

Compared to NP bulk formulations ($52.2 - 65.1 \text{ nm}$), NPs prepared by microfluidic synthesis at an equal aqueous to organic phase ratio (FRR of 10:1) displayed smaller z-average hydrodynamic sizes ($23.6 - 42.8 \text{ nm}$) and the PDI was slightly decreased at a flow rate of 2 mL min^{-1} and was further improved at flow rates of 7 to 17 mL min^{-1} ($0.064 - 0.129$). Z-average hydrodynamic sizes continuously decreased with higher flow rates, since higher flow rates result in enhanced chaotic advection and thus optimized mixing conditions that lead to higher nucleation rates and formation of smaller NPs. In contrast, NPs prepared by microfluidics at a FRR of 5:1 displayed an increase in PDI (Figure 5A) compared to NPs manufactured by microfluidics at a FRR of 10:1. These results were supported by TEM analysis, revealing that NPs were bound together by interparticular bridges (Figure 5B).

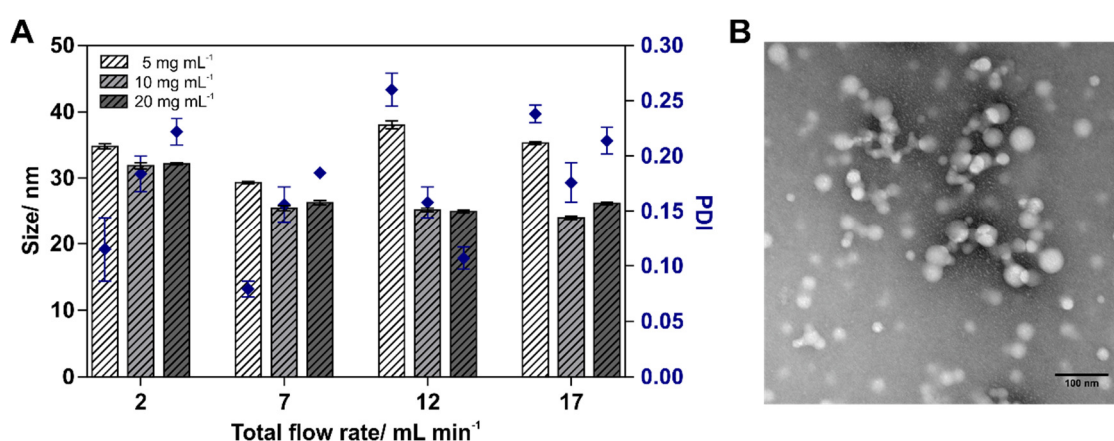


Figure 5. (A) Size and size distribution of NP510m as a function of polymer concentration and total flow rate at a constant FRR of 5:1. (B) TEM images of a selected NP formulation showing particle aggregation and coalescence. Scale bar indicates 100 nm.

Chapter 3: Microfluidic manufacturing of multicomponent nanoparticles

The process of nanoprecipitation occurs in three stages: First, small aggregates of macromolecules are formed due to nucleation, following nuclei growth and finally, aggregation until the colloidal stability is reached [177]. Self-assembly of amphiphilic copolymers can reach an equilibrium through two mechanisms [178]: If the mixing time is smaller than the time for aggregation, the NP size remains constant after the growing step and particle self-assembly occurs primarily when the solvent exchange is completed. In case that the mixing time is longer than the aggregation time, particles keep growing because macromolecules are continuously being delivered during the mixing process (Figure 6).

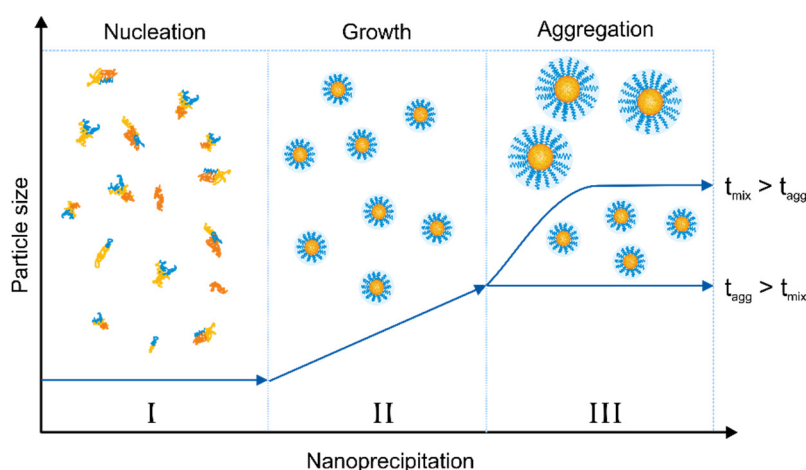


Figure 6. Schematic depiction of NP formation through nanoprecipitation. Small aggregates of copolymers are formed due to nucleation (stage I), following nuclei growth (stage II) and finally, aggregation (stage III). (Figure adapted from [178])

Thereby, supersaturation (S) of the polymer solution is considered as key factor for determination of the nucleation rate and can be expressed using equation 1 [179]:

$$S = \frac{c}{c_{\infty}} \quad (1)$$

With c being the polymer concentration in the initial organic solvent and c_{∞} being the bulk solubility in the final solvent mixture. By using a higher ratio of solvent to nonsolvent, the solubility of the polymer in the solvent mixture is increased which

results in lower supersaturation. As a consequence, solvent diffusion and thus nucleation rate is slowed down, which can promote Ostwald ripening leading to an increase in particle size [180]. Furthermore, a low supersaturation leads to secondary nucleation, meaning that both nucleation and particle growth concomitantly occur, leading to a wider size distribution.

Next, the impact of NP composition on critical particle characteristics was assessed. NP formulations (NP510m, NP515m and NP520m) with different core to shell ratios were prepared by microfluidics at a constant polymer concentration of 10 mg mL⁻¹. The copolymer mass ratio of PLA-PEG to PLGA and the copolymer block length was adjusted as described in Figure 1 and NPs were prepared at a FRR of 10:1 or 5:1 and a TFR of 2 to 17 mL min⁻¹. As shown in Figure 7, the z-average hydrodynamic particle size of NP510m, NP515m and NP520m was significantly smaller when NPs were prepared by microfluidics compared to bulk nanoprecipitation. Interestingly, changes in TFR and FRR had the highest effect on particle size and PDI of NP510m, and only minor impact on size and PDI of NP515m and NP520m. In general, neither size nor PDI of NP515m and NP520m were significantly altered except for NP515m prepared at a FRR of 5:1 and a TFR of 12 or 17 mL min⁻¹, both displaying a higher PDI compared to NP515m prepared at equal TFR but a FRR of 10:1. As NP515m and NP520m are composed of increasing fractions of hydrophobic PLA and PLGA as compared to NP510m, the solubility of the copolymer mixture in the final aqueous solvent mixture is vastly decreased, whereas the solubility in acetonitrile is only slightly changed, leading to higher supersaturation according to equation 1. In addition, the increase in supersaturation attributed to changes in the polymer composition seemed to overcompensate the decrease in supersaturation caused by the increased solubility in the final solvent mixture due to a change in solvent ratios.

These data suggest, that the composition of multicomponent polymeric NPs has a major impact on the critical quality attributes during manufacturing since it is an important determinant for the solubility of copolymers in the organic phase and final aqueous solvent, and thus has a major impact on supersaturation. Furthermore, as PLA-PEG is an amphiphilic block copolymer composed of one hydrophilic and one hydrophobic block, it can reduce the interfacial surface tension, and therefore leads to formation of smaller polymer nuclei in the mixing channel. This was also reflected by smaller sizes of NP510m (24.7 ± 0.4 nm), which are composed of a higher fraction of

Chapter 3: Microfluidic manufacturing of multicomponent nanoparticles

PLA-PEG compared to NP515m (29.2 ± 0.4 nm) and NP520m (33.5 ± 0.4 nm), when NPs were prepared by microfluidics at a FRR of 10:1 and TFR of 12 mL min^{-1} .

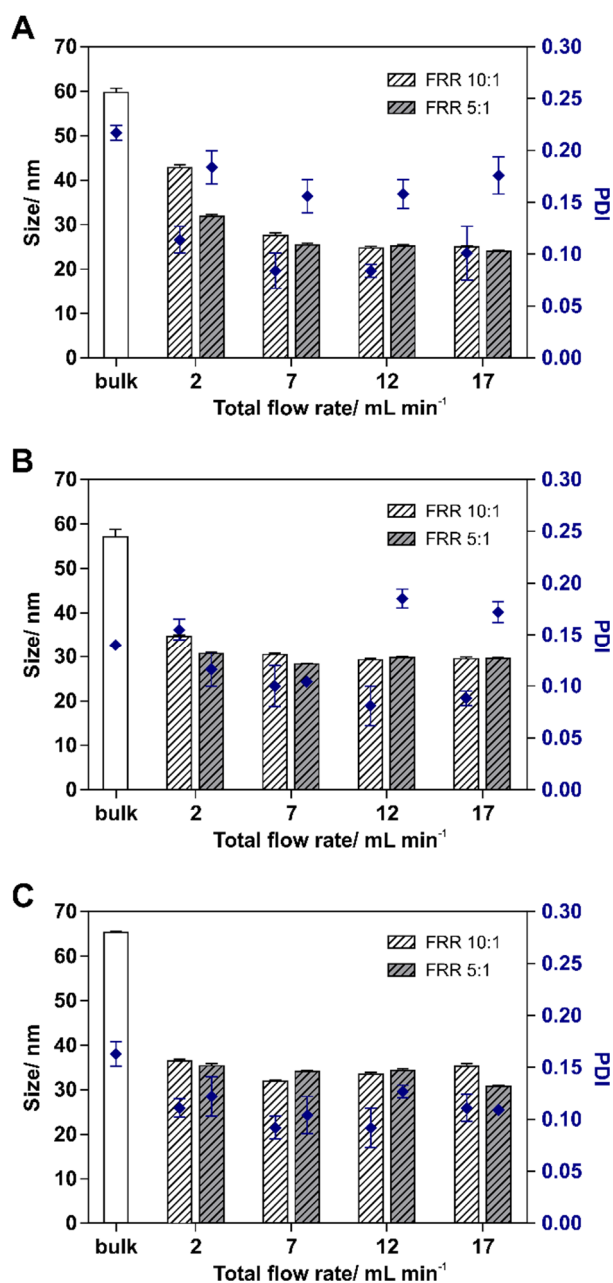


Figure 7. Impact of the total flow rate (TFR) and the flow rate ratio (FRR) on the size and size distribution of (A) NP510m, (B) NP515m and (C) NP520m prepared from a 10 mg mL^{-1} polymer solution and ultrapure water. All three NP formulations were additionally prepared *via* bulk nanoprecipitation at an aqueous to organic phase ratio of 10:1.

3.3 Characterization of the critical quality attributes

Particle size, size distribution and morphology of selected NP formulations were additionally evaluated and compared to respective intensity-weighted size distributions as determined by DLS. NP510m and NP520m both were prepared at a FRR of 1:10 and a TFR of 12 mL min⁻¹, whereas NP515m was manufactured at a FRR of 1:10 and a TFR of 17 mL min⁻¹. These NP formulations were selected since they displayed an improved size distribution (DLS) with PDIs of 0.084 (NP510m), 0.081 (NP515m) and 0.092 (NP520m). Respective NP formulations prepared by bulk nanoprecipitation were used for comparison (Figure 8).

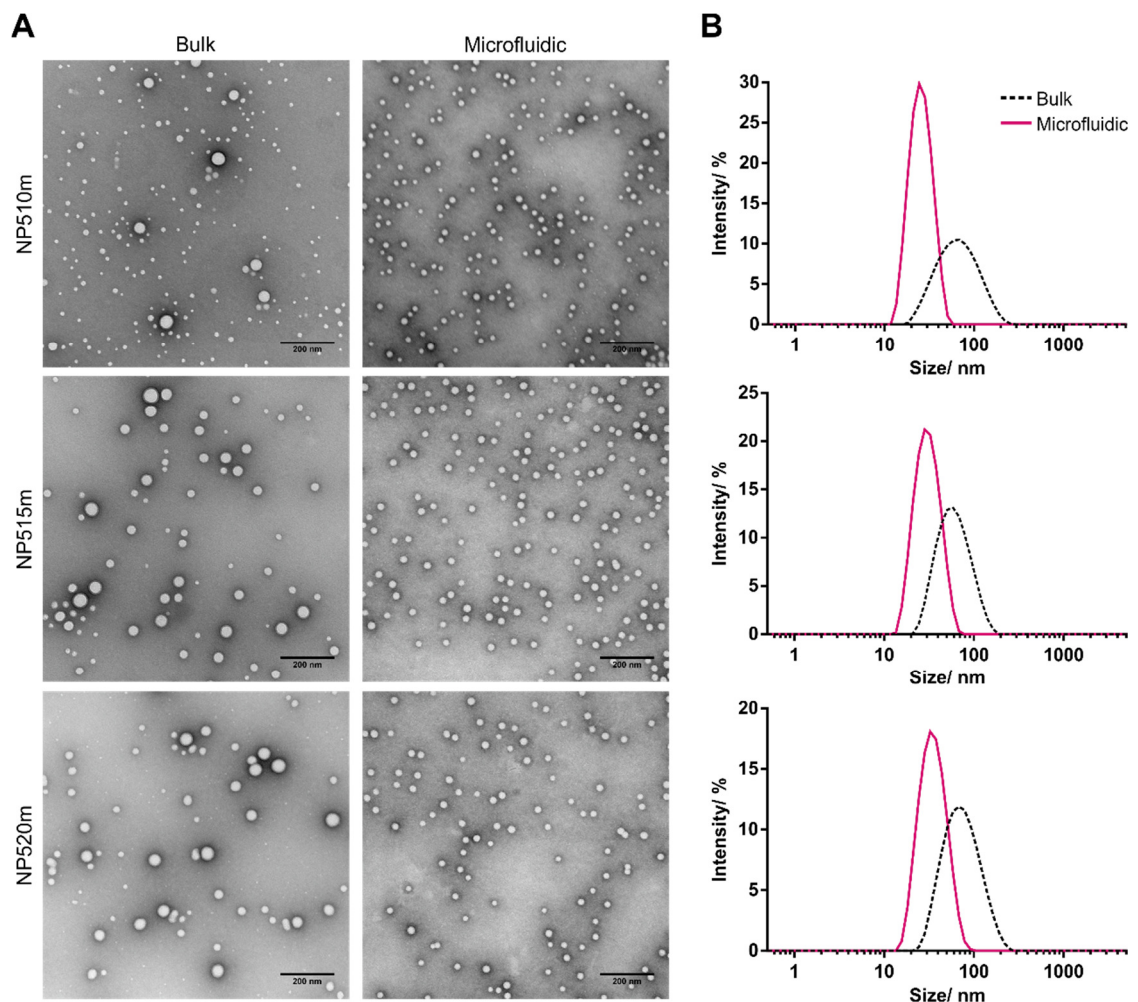


Figure 8. (A) Transmission electron microscopy images (scale bar = 200 nm) and (B) intensity-weighted size distribution (DLS) of NP510m, NP515m and NP520m prepared by bulk nanoprecipitation and microfluidic synthesis.

Chapter 3: Microfluidic manufacturing of multicomponent nanoparticles

As shown in Figure 8, size distributions of NPs prepared by microfluidic synthesis were narrower compared to formulations prepared by bulk nanoprecipitation. Comparing TEM images of NP510m, bulk nanoprecipitation resulted in high fraction in very small polymeric NPs insufficiently stabilized with additional PLGA, whereas for NP515m and NP520m, only few single micelles were detected by TEM since these two formulations possess a lower fraction of amphiphilic PLA-PEG. In contrast, DLS results indicated that the mean particle size decreased when NP510m were prepared with the microfluidic system. This is explained by the fact that z-average size analyzed by DLS is calculated as intensity-weighted mean diameter derived from the cumulants analysis. Herein, the scattering signal strongly depends on the particle diameter (d), with a d^6 correlation [181]. Therefore, larger particles are overestimated in this calculation, because the contribution of light scattering deriving from smaller NPs is vastly decreased, which is also reflected by the intensity-weighted size distribution shown in Figure 8B, where bulk formulations display a right-shift of the distribution curves towards larger particle sizes compared to microfluidic formulations. For NP515m and NP520m formulations, particle size and size distribution determined by TEM were in good agreement with corresponding DLS results.

In summary, these results clearly demonstrate that microfluidic synthesis significantly improved polydispersity of PLGA-blended PLA-PEG NPs composed of different copolymer compositions.

4 Conclusion

Bulk nanoprecipitation of multicomponent polymer particles does not offer the possibility to precisely control the mixing processes, consequently resulting in insufficient batch-to-batch consistency and moreover, a high polydispersity of core-stabilized PLGA/PLA-PEG colloids due to an unequal distribution of hydrophobic PLGA in the hydrophobic particle core.

In this study, three NP formulations with different core to shell ratios were prepared by bulk nanoprecipitation and microfluidic manufacturing. Dynamic light scattering and transmission electron microscopy were used to analyze the respective particle characteristics, such as size, size distribution and morphology. In general, both particle size and polydispersity index were decreased when NPs were manufactured with microfluidics. For NPs with a high copolymer mass ratio of PLA-PEG to PLGA, the

flow rate ratio of the aqueous outer to the organic inner phase was identified to be the key determinant for tuning the size distribution, whereas particle size was mainly controlled by the total flow rate. Polydispersity of core-stabilized PLGA/PLA-PEG NPs was significantly improved by microfluidic manufacturing - even at high flow rates and high polymer concentrations, demonstrating that microfluidics is a valuable technology that allows for reproducible and scalable manufacturing of multicomponent NPs with precisely tunable particle characteristics.

**Interaction of functionalized nanoparticles
with serum proteins and its impact on
colloidal stability and cargo leaching**

Abstract

The majority of efforts in the area of polymeric nanocarriers is aimed at providing controlled drug delivery *in vivo*. Therefore, it is essential to understand the delicate interplay of polymeric NPs with serum proteins in order to forecast their performance in a biological system. In this study, the interaction of serum proteins with functionalized polymeric colloids as a function of particle charge and hydrophobicity was investigated. Moreover, impact on NP stability and cargo leaching was assessed. The hard protein corona of polymeric NPs with either uncharged methoxy groups (NP510m), positively charged amine groups (NP510N), negatively charged carboxylic acid groups (NP510C) or zwitterionic NPs decorated with amine and carboxylic acid groups (NP510CN) was quantitatively and qualitatively analyzed and correlated with the respective colloidal stability using fluorescence resonance energy transfer (FRET). Positively charged NP510N displayed an enhanced interaction with serum proteins *via* electrostatic interactions resulting in a hard corona consisting of diverse protein components. As revealed by FRET and agarose gel electrophoresis, the enhanced adsorption of proteins onto the colloidal surface significantly altered the NP identity and severely impaired the colloidal integrity as the lipophilic cargo was continuously leached out of the hydrophobic NP core.

These results highlight the importance of generating a profound knowledge of the bio-nano interface because adherence of biomolecules can severely compromise the performance of a colloidal drug delivery system *in vivo* by changing its identity and integrity.

1 Introduction

Upon administration of nanoparticles (NPs) into the blood stream, serum proteins spontaneously bind to the colloidal surface, forming a biomolecular adsorption layer which is commonly referred to as protein corona (PC). The PC is a highly complex structure that consists of hard and soft layers that form around the NP surface [29,182,183]. The different types of layers are defined depending on how tightly biomolecules are associated with the colloids. The hard corona (HC) is composed of proteins that initially bind to the NP surface with high affinity, whereas biomolecules that are part of the soft corona (SC) secondarily interact with components of the HC rather than with the bare NP surface [184]. Furthermore, the SC is deemed to be more dynamic, consisting of rapidly exchanging biomolecules [185]. The adsorption of biomolecules onto nanomaterials is generally driven by the high surface energy of nanoscaled colloids. Thereby, interactions between proteins and NPs are governed by Coulomb forces, London dispersion, hydrogen-bonds, hydrophobic interactions, and π - π stacking [186]. Diverse particle characteristics, such as particle charge [30,187], size and surface curvature [30,33,34], surface topography [32] and hydrophobicity [31] have been identified to determine the degree, identity and kinetics of PC formation.

Adherence of biomolecules to NPs can severely alter particle attributes, which has a major impact on their key performance indicators, such as targeting capability, toxicity, aggregation behavior and their circulation time *in vivo* [171,188-190]. In addition, after being exposed to biomolecules, NPs can completely lose their integrity through disassembly, which is considered the dominant reason for premature cargo release from polymeric drug delivery systems [191]. Because protein-coating severely compromises the performance of a drug delivery system *in vivo*, it is crucial to understand and establish the relationship between physicochemical properties of polymeric colloids and interactions with serum proteins and, moreover, evaluate consequences of PC formation on NP stability and cargo release. Many efforts have been made to characterize the bio-nano interface of different kinds of NPs, however, as the interaction between serum proteins and colloids highly depends on the NP material, results often cannot be translated. NPs composed of poly(lactic-*co*-glycolic acid) and poly(lactic acid)-poly(ethylene glycol) (PLA-PEG) have recently received growing attention as drug delivery vehicles as they are biodegradable, biocompatible and offer the possibility to accommodate high amounts of hydrophobic drugs inside

Chapter 4: Impact of protein corona formation on colloidal stability

the colloidal core [10,162,164]. However, there are only limited studies available focusing on the interaction of core/shell structured polymeric colloids with biomolecules, and even less is known about their corona identity or cargo release mechanisms which makes their performance in a biological environment unpredictable.

Herein, core/shell structured NPs with differently charged surface end-groups were prepared through nanoprecipitation and the influence of surface functionalization on protein corona formation was investigated. To this end, PLA-PEG copolymers with different end-groups were synthesized and blended with PLGA to prepare NPs with either uncharged methoxy groups (NP510m), positively charged amine groups (NP510N), negatively charged carboxylic acid groups (NP510C) or zwitterionic NPs containing a mixture of amine and carboxylic acid groups (NP510CN). In the first part of this study, the four different NP formulations were evaluated for their interaction with serum proteins as a function of surface functionalization. The hard protein corona that was formed around the colloidal surface upon incubation with fetal calf serum (FCS) was quantified and its composition was analyzed by sodium dodecyl sulfate-polyacrylamide gel electrophoresis (SDS-PAGE). Furthermore, the colloidal stability in presence of serum proteins was investigated by fluorescence resonance energy transfer (FRET). In the second part, the impact of albumin adsorption on NP integrity was assessed as a function of incubation time and protein concentration using a combination of dynamic light scattering (DLS) and FRET. Protein corona induced cargo leaching of amine modified NPs was quantified by agarose gel electrophoresis.

2 Materials and methods

2.1 Materials

1,8-Diazabicyclo[5.4.0]undec-7-ene (DBU) solution, 2-Mercaptoethanol (BME), 3,6-Dimethyl-1,4-dioxane-2,5-dione (Lactide), ammonium persulfate (APS), anhydrous dichloromethane (DCM), anhydrous ethyl acetate, bovine serum albumin (BSA), deuterated chloroform (CDCl_3), fetal calf serum (FCS), formaldehyde solution (37 wt%), methoxy poly(ethylene glycol) with a molecular mass of 5000 g mol^{-1} (MeO-PEG5k-OH), Resomer® RG 502 (PLGA), sodium thiosulfate pentahydrate, trifluoroacetic acid (TFA) and the QuantiPro™ BCA Assay kit were received from Sigma-Aldrich (Taufkirchen, Germany). 1,1'-Dioctadecyl-3,3',3'-tetramethylindo-

carbocyanine perchlorate (DiI), 3,3'-dioctadecyloxycarbocyanine perchlorate (DiO), 1,1'-dioctadecyl-3,3',3',3'-tetramethylindodicarbocyanine perchlorate (DiD) and Dulbecco's phosphate buffered saline pH 7.4 (DPBS; consisting of 1.5 mM KH_2PO_4 , 8 mM Na_2HPO_4 , 2.7 mM KCl and 138 mM NaCl) were obtained from Invitrogen GmbH (Karlsruhe, Germany). Barium chloride dihydrate, iodine solution (0.1 N) and tetramethylethylenediamin (TEMED) were purchased from Carl Roth GmbH & Co KG (Karlsruhe, Germany). Pierce™ unstained protein molecular weight marker was obtained from Thermo Fisher Scientific (Schwerte, Germany). Bifunctional hydroxyl poly(ethylene glycol) carboxylic acid (COOH-PEG5k-OH) and hydroxyl poly(ethylene glycol) Boc-amine (Boc-NH-PEG5k-OH) with a molecular mass of 5000 g mol⁻¹ were purchased from JenKem Technology USA Inc. (Allen, TX, USA). Acrylamide/bis-acrylamide (37.5:1) solution, bromphenol blue sodium salt and sodium dodecylsulfate (SDS) were received from Serva Electrophoresis GmbH (Heidelberg, Germany). All other materials were reagent grade and obtained from Merck KGaA (Darmstadt, Germany). Ultrapure water was obtained using a Milli-Q water purification system (Millipore, Schwalbach, Germany).

2.2 Synthesis of functionalized PLA-PEG block copolymers

PLA-PEG-OMe (10k-b-5k), PLA-PEG-COOH (10k-b-5k) and PLA-PEG-NH₂ (10k-b-5k) block copolymers were synthesized by ring-opening polymerization as previously described by Qian *et al.* [170] with slight modifications. Prior to use, racemic 3,6-dimethyl-1,4-dioxane-2,5-dione (*D,L*-lactide) was purified by recrystallization from anhydrous ethyl acetate and dried under vacuum for at least 12 h. MeO-PEG-OH, Boc-NH-PEG-OH or COOH-PEG-OH were used as macroinitiators for a ring-opening polymerization of cyclic *rac*-Lactide using DBU as catalyst. After 1 h, the polymerization was quenched with benzoic acid. For cleavage of the Boc protection group of Boc-NH-PEG-PLA the respective polymer was dissolved in 50% (v/v) TFA in anhydrous DCM. After stirring for 30 min at RT, the solution was diluted with three volumes of anhydrous DCM and washed three times with saturated sodium bicarbonate solution and subsequently with ultrapure water. The organic phase was dried over anhydrous sodium sulfate, filtered, and concentrated under reduced pressure. For purification, block copolymers were precipitated in diethyl ether and dried under vacuum at either 35 °C (PLA-PEG-NH₂) or 45 °C (PLA-PEG-OMe, PLA-PEG-COOH). ¹H-NMR spectra were recorded in CDCl₃ at 295 K using a Bruker

Chapter 4: Impact of protein corona formation on colloidal stability

Avance 300 spectrometer (Bruker BioSpin GmbH, Rheinstetten, Germany). The number-average molecular weight of block copolymers was determined by integration of the methylene signal of PEG residues based on molecular weight (provided by the manufacturer) and calculation of the methine and methylene proton signals of PLA.

2.3 Preparation and characterization of polymeric nanoparticles

Polymeric NPs were prepared by bulk nanoprecipitation as previously described [165]. In general, functionalized PLA-PEG and PLGA were diluted with acetonitrile to a final polymer concentration of 10 mg mL⁻¹. The copolymer mass ratio of PLA-PEG to PLGA was kept constant at 70/30. For preparation of FRET NPs, DiO and DiI were added to the organic polymer solution (10 nmol per mg polymer). For cargo leaching experiments, NP510N were labeled with DiD (2.5 nmol mg⁻¹). NPs used for the determination of the hard protein corona (Micro BCA, SDS PAGE) were labeled with DiI (1 nmol mg⁻¹). The polymer solution was then added dropwise into 10 volumes of vigorously stirred ultrapure water and NP dispersions were stirred for 3 hours to remove the organic solvent. NPs were filtered through a 0.45 µm Rotilabo® PES syringe filter (Carl Roth, Karlsruhe Germany) and purified *via* ultrafiltration using Macrosep® Advance Centrifugal Devices (Pall GmbH, Dreieich, Germany) with 100 kDa MWCO. The exact NP concentration was either weighed out after lyophilization or determined by an iodine complexation assay [192]. Z-average hydrodynamic size, polydispersity index (PDI) and ζ-potential of NPs were determined on a Zetasizer Nano ZS device (Malvern, Herrenberg, Germany). DLS measurements were performed in ultrapure water at a constant temperature of 25 °C using semi-micro PMMA disposable cuvettes (Brand, Wertheim, Germany). The position from the cuvette wall was set to 4.65 mm and the attenuator was optimized by the device. The ζ-potential was measured in 1 mM NaCl solution at 25 °C using folded capillary cells (Malvern, Herrenberg, Germany). Data were collected and analyzed with the Malvern Zetasizer software version 7.11 (Malvern Instruments, Worcestershire, United Kingdom).

2.4 Nanoparticle quantification

Three batches of each NP formulation (NP510C, NP510N, NP510CN and NP510m) were prepared in ultrapure water, purified and concentrated as described above. A colorimetric iodine complexation assay [192] was used to quantify the exact amount of

PEG. In brief, NP samples were diluted in ultrapure water to a final PEG concentration of approximately 2.5 to 50 $\mu\text{g mL}^{-1}$. Dilutions of methoxy poly(ethylene glycol) with a molecular mass of 5000 g mol^{-1} were used as calibration standards (0 – 50 $\mu\text{g mL}^{-1}$). Two parts of a solution containing 5% (m/v) barium chloride in 1 N HCl were mixed with 1 part of a 0.1 N iodine/ potassium iodide solution immediately before use. 140 μL of sample and standard dilutions were transferred into a 96-well plate, mixed with 60 μL of the iodine reagent and incubated for 15 min at room temperature. Absorbance was measured at 535 nm using a FluoStar Omega fluorescence microplate reader (BMG Labtech, Ortenberg, Germany). The exact polymer concentration was determined gravimetrically after lyophilization of the concentrated NP samples and plotted against the PEG content determined by the iodine assay. As the PEG content of each NP formulation was considered to be constant, from this point on, the PEG content of freshly prepared samples was determined against the mPEG5k standard and used to calculate the polymer concentration (Figure S1).

2.5 Characterization of the hard protein corona

Equal amounts of DiI labeled functionalized NPs were incubated with 50% (v/v) FCS for 1 hour at 37 °C. Afterwards, NPs were isolated by centrifugation at 20,000 g, for 2 h at 4 °C and resulting NP pellets were washed two times with ultrapure water to remove any unbound protein. To ensure that NP pellets only consisted of nanoparticle-associated proteins, FCS in DPBS was treated equally and used as control. NPs were dispersed in ultrapure water and stored at 4 °C. Sodium dodecyl sulfate polyacrylamide gel electrophoresis (SDS-PAGE) was used to analyze the composition of the hard protein corona of the four different NP formulations. NP samples (650 $\mu\text{g mL}^{-1}$), the FCS placebo control (undiluted) and a 0.5 % (m/v) FCS solution were diluted with Laemmli sample buffer (4x) supplemented with 2-mercaptoethanol and boiled for 5 minutes at 95 °C to elute and denature proteins adsorbed to the colloidal surface. An unstained protein molecular weight marker with a molecular range from 14.4 to 116 kDa was used as molecular weight standard. Proteins were separated by SDS-PAGE using a 4.5% stacking/ 12% separating gel. The electrophoresis was run for 1 h at a constant voltage of 120 V and a decreasing current starting at 68 mA using a Pharmacia Amersham EPS 600 gel electrophoresis device (Bio-Rad Laboratories, Munich, Germany). Protein bands were visualized by silver staining [193]. Gels were imaged with a ChemiDoc™ MP gel imaging system (BioRad, Munich, Germany) and

Chapter 4: Impact of protein corona formation on colloidal stability

evaluated with the software Image Lab 6.0 (BioRad, Munich, Germany). For quantification of the hard protein corona, NPs were diluted to a polymer concentration of 500 $\mu\text{g mL}^{-1}$, the FCS placebo control was analyzed undiluted. The amount of proteins bound to each NP formulation was quantified using a Micro BCATM Protein Assay Kit (Thermo Fisher Scientific, Dreieich, Germany) according to the manufacturer's instruction and normalized to the colloidal surface area. All NP and control samples were analyzed in quadruplicates.

2.6 Fluorescence Resonance Energy Transfer (FRET)

A FRET experiment was used to assess the colloidal stability of functionalized NPs. DiO/DiI co-labeled NPs were diluted at a volume ratio of 1 to 10 in either DPBS (pH 7.4) or FCS and incubated at 37 °C. Fluorescence spectra were recorded during an incubation period of 24 h on an LS-55 fluorescence spectrophotometer (PerkinElmer, Rodgau, Germany). FRET fluorescence was excited at 460 nm (DiO) and emission spectra (DiI) were recorded between 485 and 710 nm. FRET ratios of different NP formulations were calculated using equation 1 [194]:

$$\text{FRET} = \frac{I_{\text{DiI}(\text{corr.})}}{I_{\text{DiO}(\text{corr.})} + I_{\text{DiI}(\text{corr.})}} \quad (1)$$

Where $I_{\text{DiI}(\text{corr.})}$ and $I_{\text{DiO}(\text{corr.})}$ are the blank-corrected fluorescence intensities at the emission maxima of DiI and DiO, respectively. Calculated FRET ratios were normalized to $t = 0$.

2.7 Adsorption of bovine serum albumin to nanoparticles

The adsorption of BSA onto the colloidal surface was investigated by DLS. Functionalized NPs (0.1 mg mL^{-1}) were incubated in either DPBS pH 7.4 or in DPBS supplemented with 45 mg mL^{-1} BSA for 1 h at 37 °C and subsequently cooled down to ambient temperature. Changes in particle size were analyzed by DLS as described above.

2.8 Serum stability of amine-modified NPs (NP510N)

For cargo leaching experiments, NP510N were labeled with DiD (2.5 nmol mg^{-1}) that was physically entrapped in the hydrophobic core. NP510N (1.0 mg mL^{-1}) were

incubated with 0, 15, 45 or 90 mg mL⁻¹ BSA or 90 % FCS for 1 hour at 37 °C and DiD leaching was determined by agarose gel electrophoresis at 60 V for 1 h using a 0.75% agarose gel. A solution of BSA (90 mg mL⁻¹) spiked with 12.5 μM DiD served as control. Gel images were acquired on a ChemiDoc™ MP gel imaging system (BioRad, Munich, Germany) and analyzed with the corresponding software Image Lab 6.0 (BioRad, Munich, Germany) before and after iodine staining (15 min: 2% BaCl₂, 0.02 N iodine in 0.4 M HCl). Relative fluorescence intensities of DiD-labeled NPs and released DiD was quantified using ImageJ image analysis software (version 1.52, National Institutes of Health, Bethesda, Maryland). All cargo leaching samples were analyzed in duplicates.

For FRET experiments DiO/DiI labeled NP510N were diluted in DPBS supplemented with 0, 15, 45 or 90 mg mL⁻¹ BSA or 90% (v/v) FCS to attain a final NP concentration of 0.1 mg mL⁻¹ and incubated at 37 °C for different periods of time (0, 1, 2, 4, 7, 12, 24 h). NP dilutions in acetone were used to achieve complete decomposition of polymeric NPs and served as positive control. FRET fluorescence was excited at 460 nm (DiO) and emission spectra (DiI) were recorded between 485 and 710 nm using an LS-55 fluorescence spectrophotometer (PerkinElmer, Rodgau, Germany). Spectra smoothing was performed using a Savitzky-Golay polynomial. FRET ratios were calculated as described above and normalized to t = 0 h.

Transmission electron microscopy (TEM) was used to evaluate the size, morphology and size distribution of NP510N prior and after incubation with BSA (45 mg mL⁻¹) for 5 hours at 37 °C. To remove unbound proteins and buffer salts, NPs were subsequently dialyzed (100 kDa MWCO) against 4 L of ultrapure water. Freshly prepared NP510N served as control. NP samples were diluted to a final polymer concentration of approximately 0.1 mg mL⁻¹ and applied onto carbon-coated copper grids (300 mesh; Plano, Wetzlar, Germany). After incubation for 5 minutes, excess sample solution was removed with a filter paper and samples were negatively stained with 1% uranyl acetate solution. Sample grids were dried and stored in a desiccator until they were analyzed. TEM images were acquired on a TEM Zeiss 902 (80 kV) electron microscope (Zeiss, Oberkochen, Germany).

2.9 Statistical analysis

All results are presented as mean ± standard deviation, based on the data obtained from at least $n=3$ samples unless stated otherwise. Statistical significance was

Chapter 4: Impact of protein corona formation on colloidal stability

determined by means of one-way ANOVA, followed by Tukey's *post-hoc* test using GraphPad Prism 6.0 (GraphPad Software Inc., La Jolla, CA, USA). Statistical significances were set as indicated.

3 Results and discussion

3.1 Characteristics of functionalized polymeric nanoparticles

Core/shell structured NPs consisting of hydrophobic PLGA and amphiphilic PLA-PEG were used to evaluate the interaction of serum proteins with functionalized polymeric colloids. Herein, PLA-PEG was used to introduce different functional groups, such as methoxy groups, amine groups or carboxylic acid groups. Using blends of PLGA and functionalized PLA-PEG copolymers, four different NP formulations were generated that were functionalized with either uncharged methoxy groups (NP510m), positively charged amine groups (NP510N), negatively charged carboxylic acid groups (NP510C) or a mixture of amine and carboxylic acid groups (NP510CN).

Functionalized NPs were characterized for their hydrodynamic z-average size and ζ -potential in ultrapure water and 1 mM NaCl solution, respectively. The hydrodynamic particle size as determined by DLS was comparable for all four NP formulations, ranging from 59.7 to 69.4 nm (Figure 1A). Surface functionalization of the four NP formulations was confirmed by ζ -potential measurements (Figure 1B).

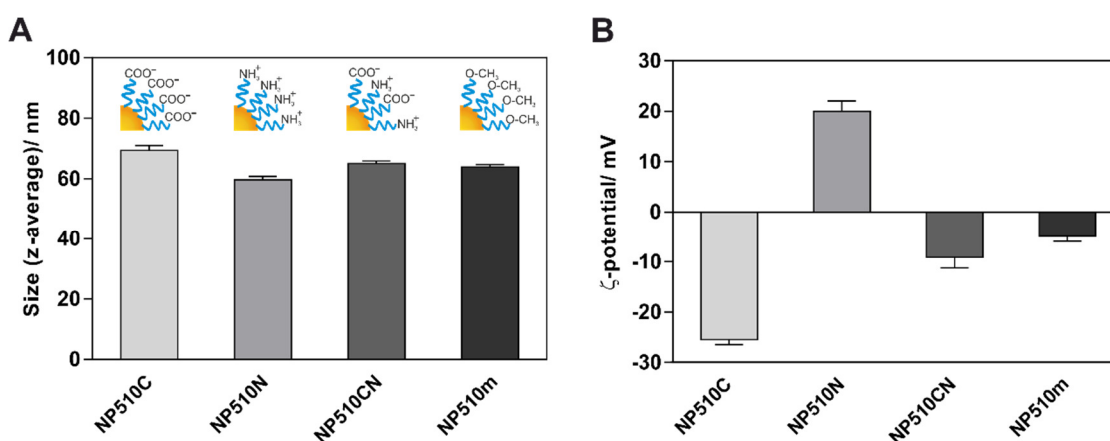


Figure 1. (A) Hydrodynamic z-average size and (B) ζ -potential of polymeric NPs functionalized with either carboxylic acid groups (NP510C), amine groups (NP510N), carboxylic acid and amine groups (NP510CN) or methoxy groups (NP510m).

NPs decorated with carboxylic acid groups (NP510C) possessed a strong negative charge of -25.5 mV, whereas NPs functionalized with amine groups (NP510N) had a positive charge of +20.2 mV. The uncharged NP510m and zwitterionic NP510CN were both slightly negatively charged (-4.9 and -9.1 mV) which was expected as PLGA which is part of the particle core contains residual free carboxylic acid groups and therefore, possesses a negative charge. Bare PLGA and PLA NPs are reported to have ζ -potentials ranging from -20 mV to -70 mV [194,195].

3.2 Characterization of the hard protein corona

Composition and quantities of biomolecules adsorbed onto the colloidal surface play an important role in identifying the unique physiological response to a distinct nanomaterial after administration into the blood stream. One dimensional SDS-PAGE was used to identify the components involved in the hard protein corona formed upon incubation of NPs with fetal calf serum for 1 h at 37 °C. Samples were adjusted to equal polymer concentrations to enable a semi quantitative comparison. A placebo buffer solution mixed with FCS was treated equally and used as control to make sure that only nanoparticle-associated proteins were isolated by centrifugation. As shown in Figure 2A, a distinct protein band with a molecular weight of approximately 66-67 kDa could be found in the hard corona of all NP samples. This band is most likely attributed to albumin (66 kDa) [196], the most abundant protein in plasma.

Positively charged NP510N displayed the highest number and amount of proteins adsorbed onto the colloidal surface which was expected since most of the serum proteins possess a negative net charge at physiological pH, which instantly enables the adsorption onto the colloidal surface due to strong electrostatic interactions followed by the adherence of oppositely charged proteins.

Interestingly, albumin was also enriched in the corona of negatively charged NP510C. Although albumin is negatively charged at physiological pH, it contains 60 positively charged lysine groups [197,198], providing cationic patches on the surface that can interact with the carboxylate groups on the colloids. Moreover, albumin can also interact with positively charged proteins that initially adhere to the NPs, forming a second protein layer. Although zwitterionic NP510CN and uncharged NP510m displayed comparable ζ -potentials, the protein corona of NP510m was more pronounced and also composed of a higher number of different proteins as most serum

Chapter 4: Impact of protein corona formation on colloidal stability

proteins undergo conformational changes when they come into contact with nanocarriers and thereafter, can interact *via* hydrophobic interactions. BSA has been reported to show clear conformational changes with significant reduction in its alpha-helical structures upon binding to cationic or hydrophobic colloids, whereas BSA adsorbed onto the surface of anionic colloids retains its native structure [197,199].

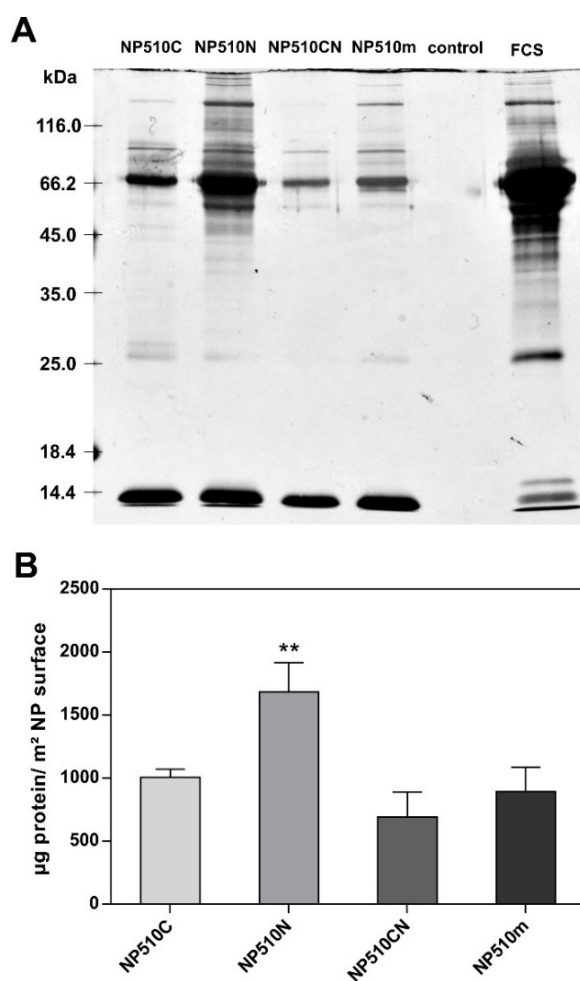


Figure 2. (A) Composition of the hard protein corona of NP510C, NP510N, NP510CN and NP510m was evaluated by sodium dodecyl sulfate-polyacrylamide gel electrophoresis. After incubation of functionalized NPs with fetal calf serum for 1 h at 37 °C, NPs were purified from unbound proteins by centrifugation. To make sure that only nanoparticle-associated proteins were analyzed, FCS in DPBS was treated equally and used as placebo control. Diluted FCS (1:200) was used to determine the full range of proteins that can potentially interact with functionalized NPs. (B) Quantification of the hard protein corona using a Micro BCA™ Protein Assay Kit. The amount of proteins was normalized to the respective surface area of functionalized NPs. Levels of significance are indicated as: (**) $p < 0.01$, compared to all other NP formulations. Data are expressed as mean \pm standard deviation.

The amount of proteins involved in formation of the hard protein corona was further quantified by a commercially available Micro BCA™ Protein Assay Kit and normalized to the NP surface area. As depicted in Figure 2B, the hard protein corona of zwitterionic NP510CN displayed the lowest amount of proteins (725 $\mu\text{g per m}^2$), as this NP formulation provides the fewest regions where hydrophobic or electrostatic interactions can occur. The amount of adsorbed serum proteins was 1.3-fold and 1.6-fold increased for uncharged NP510m (935 $\mu\text{g per m}^2$) and negatively charged NP510C (1124 $\mu\text{g per m}^2$) as these NP formulations can interact *via* hydrophobic and electrostatic forces, respectively. Positively charged NP510N showed the highest amount of proteins bound to the surface (1713 $\mu\text{g per m}^2$) which was even 2.4-fold increased compared to NP510CN. In summary, it can be concluded that NP charge and hydrophobicity both are decisive factors for the identity and amount of biomolecules involved in the formation of the hard protein corona, which is in accordance with literature [200].

3.3 Impact of corona formation on nanoparticle integrity

Colloidal stability of DiO/DiI loaded functionalized NPs in presence of serum proteins was assessed by fluorescence resonance energy transfer (FRET). For this purpose, a lipophilic FRET pair (DiO and DiI) was physically entrapped into the hydrophobic particle core. Energy transfer from the green fluorescent donor DiO (emission maximum: 505 nm) to the red-orange acceptor probe DiI (emission maximum: 575 nm) only occurs if the dye molecules are in close proximity to each other. Release of lipophilic fluorescent molecules, e.g. due to NP disassembly or cargo leaching, results in enlarged distance between the two dye molecules and consequently, to a reduced FRET efficiency [191,201]. The basic principle of FRET is outlined in Figure 3A displaying fluorescence spectra of NPs dispersed in DPBS and acetone. FRET-labeled NPs in DPBS exhibit a fluorescence maximum at around 575 nm, which corresponds to the DiI emitted fluorescence. In contrast, the emission maximum was shifted to 505 nm (DiO) when particles were decomposed in acetone because the distance of both dyes was above the required range and the energy transfer from DiO to DiI was maximally suppressed.

For each NP formulation, FRET ratios were calculated and normalized to $t = 0$. As depicted in Figure 3B, the FRET ratio only marginally decreased by 4.4% (to 7.9%) when NPs were incubated in DPBS (pH 7.4) at 37 °C for different periods of time. In

Chapter 4: Impact of protein corona formation on colloidal stability

contrast, FRET ratios exponentially decreased over time when functionalized NPs where incubated with 90% FCS, indicating that the integrity was severely impaired and dye molecules were released over time.

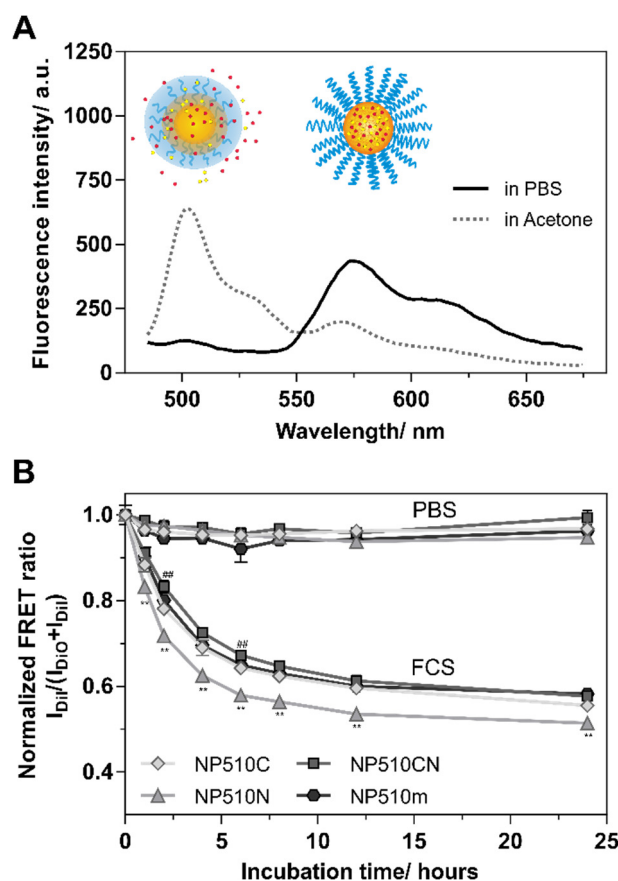


Figure 3. (A) Exemplary fluorescence spectra of NPs dispersed in either DPBS (solid line) or acetone (dashed line). FRET-labeled NPs in DPBS exhibit a fluorescence maximum at around 575 nm, whereas the emission maximum was shifted to 505 nm when particles were dispersed in acetone which leads to complete dissolution of the polymeric NPs. (B) Time-resolved FRET ratios of functionalized NPs incubated in either DPBS (pH 7.4) or 90 % (v/v) FCS at 37 °C. Data were normalized to $t = 0$ and expressed as mean \pm standard deviation. Levels of significance are indicated as: (**) $p < 0.01$, compared to all other NP formulations and (##) $p < 0.01$, comparing NP510C and NP510CN.

Positively charged NP510N displayed the most pronounced decay in FRET efficiency, whereas the FRET ratio of anionic NP510C, zwitterionic NP510CN and uncharged NP510m remained significantly higher ($p < 0.01$) during the 24 h incubation period,

indicating enhanced stability of these NP formulations in presence of serum proteins. The decay curve of NP510CN was slightly upshifted compared to NP510C and NP510m during the first 8 hours of incubation ($p < 0.01$ compared to NP510C at 2 h and 6 h). Decay curves of all samples were fitted with a one phase exponential decay to determine the half lifes ($t_{1/2}$) and plateaus that are theoretically reached end points, as both parameters are indicator for NP stability (Table 1).

Table 1: Stability of different NP formulations in fetal calf serum. FRET efficiency curves were fitted with a one phase exponential decay.

NP Formulation	Plateau/ %	Half Life/ h	Quality of curve fitting (R^2)
NP510C	57.59 ± 1.08	2.167	0.9932
NP510N	53.32 ± 0.85	1.639	0.9952
NP510CN	58.55 ± 0.68	2.699	0.9979
NP510m	58.86 ± 0.63	2.165	0.9976

The calculated $t_{1/2}$, corresponding to the range between the initial FRET ratio at $t = 0$ and the calculated plateaus, was 1.6-fold higher for zwitterionic NP510CN ($t_{1/2} = 2.70$ h) compared to NP510N ($t_{1/2} = 1.64$ h) and 1.2-fold higher compared to uncharged NP510m ($t_{1/2} = 2.17$ h) and anionic NP510C ($t_{1/2} = 2.17$ h). Although the half life of NP510CN was significantly higher, the plateau of NP510CN (58.6%) was comparable to plateaus of NP510m (58.9%) and NP510C (57.6%). In contrast, the plateau calculated for NP510N (53.3%) was significantly lower, implying that the stability of NP510N was most impaired in presence of serum compared to its uncharged, zwitterionic charged and anionic counterparts. These results clearly demonstrate that NP integrity can be directly correlated with the amount of protein bound to the colloidal surface.

3.4 Nanoparticle-albumin interaction

The degree of protein adsorption onto the colloidal surface was assessed by DLS since adsorption of proteins leads to an increase in hydrodynamic size and mass of NPs and thus alters their Brownian motion [202]. Albumin was chosen as model protein for this investigation as it was present in the protein corona of all NP formulations as described

Chapter 4: Impact of protein corona formation on colloidal stability

above. Moreover, albumin is the most abundant protein in human plasma with a concentration in the range of 35 to 50 mg mL⁻¹ [203] and along with IgG and fibrinogen, it is known to be involved in the early stage of corona formation as it rapidly adsorbs onto colloidal surfaces in plasma [30,204] and has been reported to have a major impact on *in vivo* biodistribution of NPs [194]. In this experiment, NPs were incubated with 45 mg mL⁻¹ BSA, corresponding to plasma concentrations *in vivo*.

Figure 4 shows the intensity-weighted size distribution of NP510C, NP510N, NP510CN and NP510m. Upon incubation with BSA, a right shift of intensity-weighted nanoparticle peak positions could be observed, indicating an increase in size resulting from the formation of a protein layer around the NP surface.

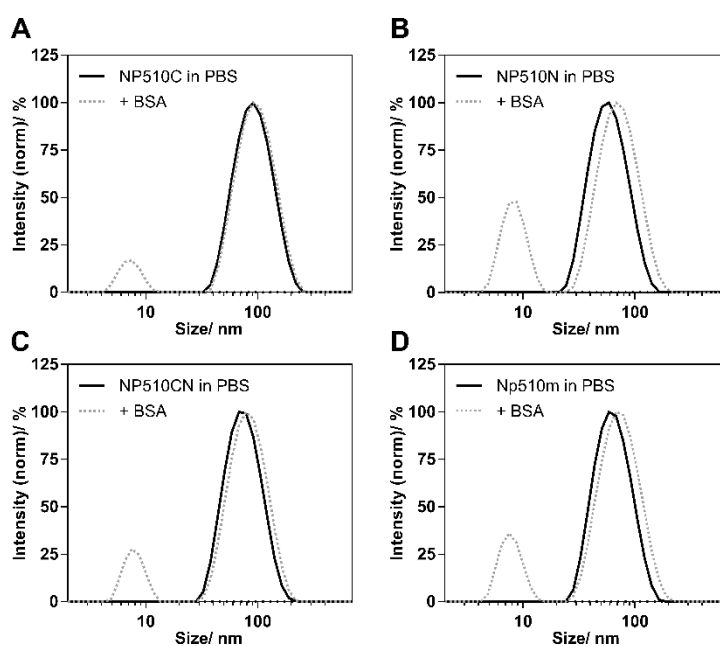


Figure 4. Intensity-weighted size distribution of (A) NP510C, (B) NP510N, (C) NP510CN and (D) NP510m determined by DLS in either DPBS (solid line) or after incubation for 1 h at 37 °C with 45 mg mL⁻¹ BSA (dashed line). Peak intensities were normalized for better comparison.

The increase in size, as determined by comparison of the mean values of intensity-derived peaks, was only minor for negatively charged NP510C (+7.8%) and medium for zwitterionic NP510CN (+10.4%) and uncharged NP510m (+16.2%).

Although the ζ -potential of NP510CN and NP510m was slightly negative, methoxy-decorated NPs can further interact with BSA *via* hydrophobic interactions. In contrast, albumin adsorption was most pronounced for NP510N due to strong electrostatic interaction of positively charged amine groups with albumin that possess a negative net charge at physiological conditions, leading to a significant increase in colloidal size (+22.5%) which derives from the formation of a distinct BSA corona. For NP samples that were incubated with BSA, two distinct DLS populations were obtained, referring to unbound BSA with a hydrodynamic diameter of approximately 9 nm [194] and NPs with a BSA corona. As a result, the PDI of these samples was vastly increased, e.g. the PDI of NP510N was 0.13 in DPBS and 0.63 in DPBS supplemented with BSA (Figure S2).

Because the interaction of NP510N with BSA was most pronounced, this NP formulation was further used to assess the kinetics of albumin adsorption. To this end, NP510N were incubated in either PBS pH 7.4 or DPBS supplemented with 45 mg mL⁻¹ BSA at 37 °C and size and PDI were measured in 0.5 h intervals over a period of 12 hours. As depicted in Figure S2, the size of NPs incubated with BSA initially increased by approximately 20 nm but thereafter, remained constant over time. This indicates, that adsorption of albumin occurs within a few seconds, which is in agreement with previous studies [204].

To investigate the impact of albumin concentration on cargo release kinetics, DiO/DiI co-labeled NP510N were incubated with increasing BSA concentrations (0 - 90 mg mL⁻¹) and the FRET fluorescence emission was monitored for a period of 24 h. No significant changes in FRET signals were observed when NPs were incubated in DPBS (Figure 5A) implying that the colloidal integrity was maintained and dye molecules were not released into the surrounding aqueous media. In contrast, for samples that were incubated with albumin, both, the DiO and the DiI fluorescence intensity increased with higher albumin concentration and longer incubation time, as indicated by arrows (Figure 5B-D). This was somewhat surprising since previous studies had demonstrated that the release of dye molecules from the particle core results in the increase in DiO fluorescence, whereas the DiI fluorescence simultaneously decreases [205]. The obtained results can be explained by partitioning of the fluorescent dyes. One fraction of the molecules is accumulating in a domain, where the distance between the donor and the acceptor is reduced, which consequently increases the DiI fluorescence.

Chapter 4: Impact of protein corona formation on colloidal stability

However, another fraction of the FRET pair is moving away from each other, resulting in a larger distance and a decrease in the energy transfer from DiO to DiI, consequently leading to an increase of the DiO-associated fluorescence intensity.

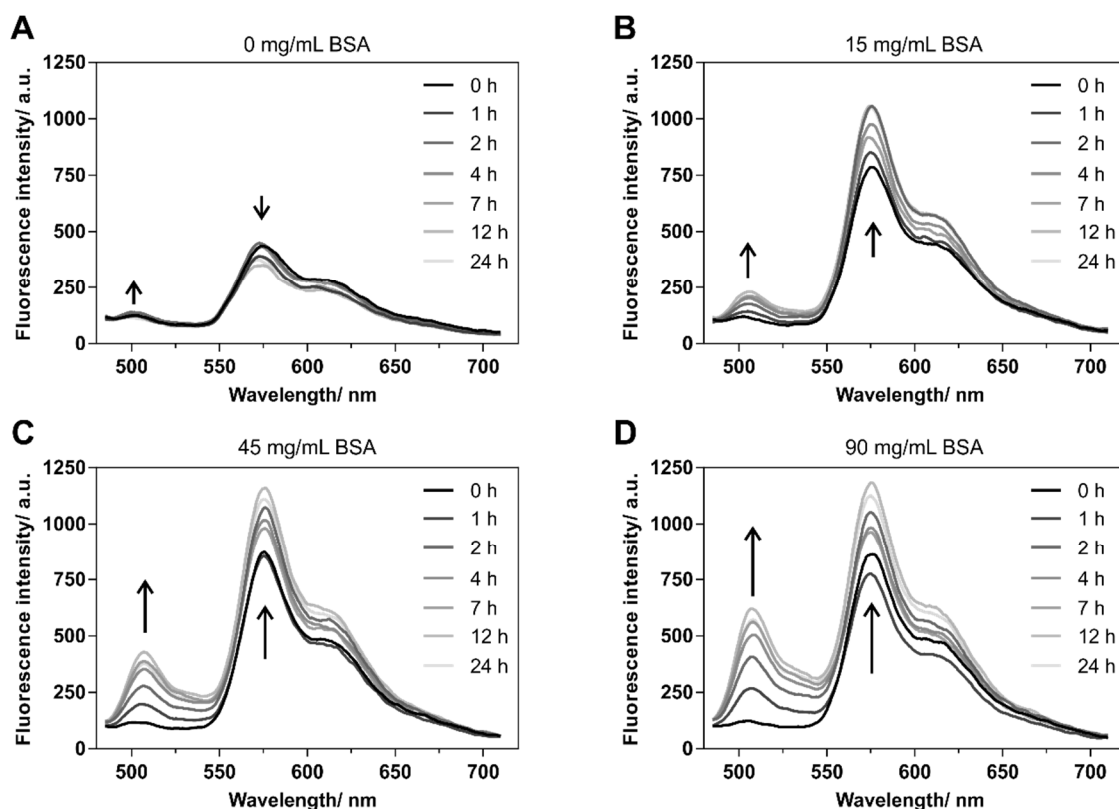


Figure 5 Time-resolved FRET emission fluorescence spectra of DiO/DiI loaded NP510N measured during incubation (37 °C) with either (A) 0 mg mL⁻¹, (B) 15 mg mL⁻¹, (C) 45 mg mL⁻¹ or (D) 90 mg mL⁻¹ BSA after 0, 1, 2, 4, 7, 12 and 24 hours. The maximum at 505 nm derives from the donor dye (DiO), whereas the maximum at 570 nm is attributed to the emission of the acceptor dye (DiI).

Moreover, partitioning of DiO and DiI was identified to be a two step process, as the increase in DiI fluorescence instantly occurred upon incubation with BSA, whereas the increase in DiO fluorescence emerged at a later stage (Figure 6). This clearly demonstrates, that adsorption of BSA onto the colloidal surface triggers an immediate cargo partitioning from the particle core into the protein corona, resulting in a closer proximity of the dye molecules and thus, to an enhanced FRET efficiency. As there is a

constant exchange of BSA molecules that are adsorbed on the surface with unbound BSA in solution, dyes will be constantly leached out until an equilibrium is reached, which will be determined by the concentration and localization of lipophilic molecules in the hydrophobic particle core. It is assumed that diffusion of dyes within the polymeric core is limited and cargo leaching only occurs if proteins and dyes are in close proximity to each other. Thus, it is expected that leaching induced cargo escape will reach a plateau over time after the outer dye layer at the interface of hydrophobic core and hydrophilic shell is depleted.

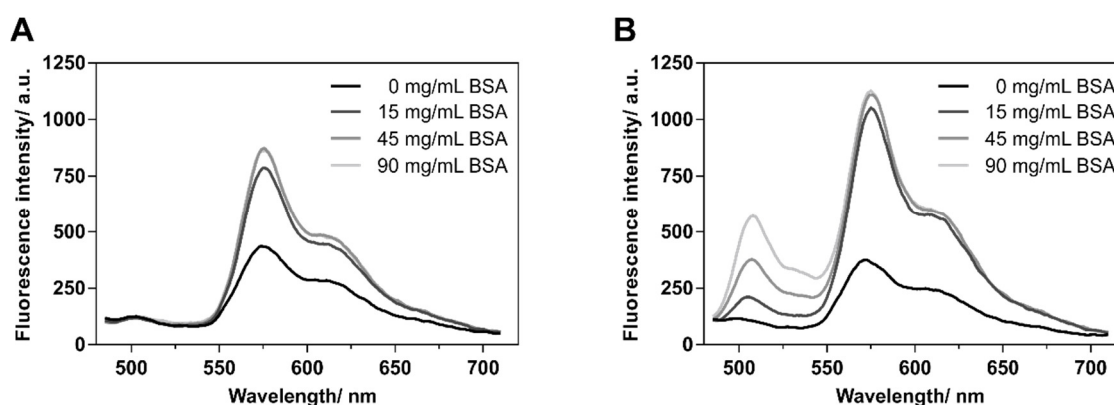


Figure 6. FRET fluorescence spectra of DiO/DiI loaded NP510N recorded (A) after 0 and (B) after 24 hours of incubation with increasing concentrations of BSA.

To determine the incubation time needed to reach an equilibrium where no further decrease in energy transfer occurs, FRET ratios of NP510N samples were calculated. As shown in Figure 7, NP samples incubated with 15 mg mL⁻¹ BSA displayed no significant reduction in FRET efficiency compared to the control (0 mg mL⁻¹) over time, whereas the FRET ratio of NP510N incubated with either 45 or 90 mg mL⁻¹ BSA gradually decreased during the initial 4 hours of incubation and then stayed constant at 85.7% and 77.6%, respectively.

Chapter 4: Impact of protein corona formation on colloidal stability

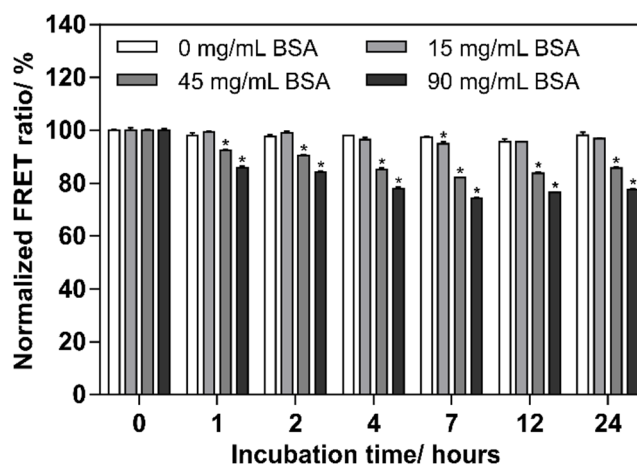


Figure 7. Normalized FRET ratios of NP510N incubated with different BSA concentrations at 37 °C. Data were normalized to $t=0$ and expressed as mean \pm standard deviation. Levels of significance are indicated as: (*) $p < 0.01$, compared to control NPs incubated in DPBS.

The degree of cargo leaching caused by protein adsorption onto the NP surface was quantified by agarose gel electrophoresis. NP510N were incubated with increasing concentrations of BSA (0, 15, 45 or 90 mg mL⁻¹) or 90% FCS for 4 hours at 37 °C. DiD in DPBS supplemented with or without 90 mg mL⁻¹ BSA served as references. Samples were separated on a 0.75% agarose gel and DiD associated fluorescence was used to assess the amount of dye either physically entrapped inside the particle core or leached out and bound to serum proteins. Gels were additionally analyzed after staining with iodine solution, as iodine incorporates into PEG polymers and forms a brownish precipitate. This treatment was expected to mask fluorescence associated with NPs because the formation of a precipitate in the PEG shell was considered as an embargo for fluorescence emission originating from the particle core. By this experimental design, even low amounts of protein-bound DiD could be detected after staining. The protein/dye control consisting of BSA spiked with DiD was not only considered as marker to evaluate the position of protein-bound cargo, but was further used to determine a fluorescence ratio of the acquired fluorescence images before and after staining, which allows for the quantification of the faint protein-bound dye in relation to dye entrapped in NPs. All samples were loaded into pockets located in the vertical center of the agarose gel as protein formation was expected to invert the NP charge.

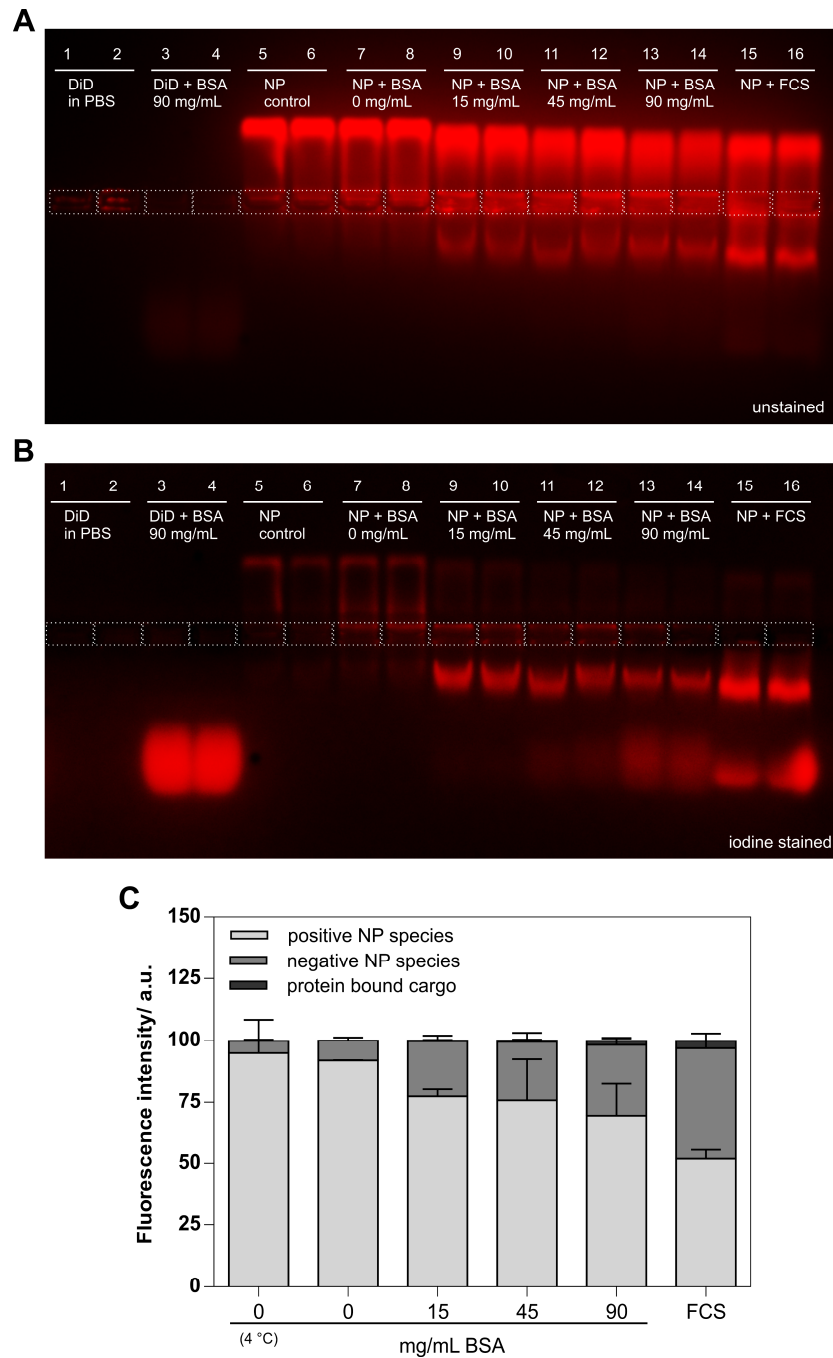


Figure 8. Cargo leaching of DiD loaded NP510N was assessed by agarose gel electrophoresis (A) before and (B) after iodine staining. DiD in DPBS and DiD in 90 mg mL⁻¹ BSA served as dye controls. NPs were either incubated with increasing concentrations of BSA (0 – 90 mg mL⁻¹) or with 90% (v/v) FCS for 4 hours at 37 °C. NPs stored at 4 °C served as particle control. (C) Fluorescent band detected in the unstained gel were used to assess the amount of negative and positive NP species, the iodine stained gel was used to determine the amount of protein-bound cargo.

Chapter 4: Impact of protein corona formation on colloidal stability

With this setting, NP species that still possess a positive charge migrate upwards to the cathode, whereas negatively charged NP species as well as BSA-bound cargo approaches the anode. As depicted in Figure 8A, NP510N that were either freshly prepared (lane 5 and 6) or incubated in PBS without the addition of BSA (lane 7 and 8) almost completely consisted of positively charged NP species. In contrast, samples that were incubated with BSA displayed an additional band below the pockets which was considered as NP species possessing a negative charge. This charge inversion was attributed to the adsorption of high amounts of negatively charged BSA onto the surface of NP510N. With increasing concentrations of BSA (lane 5 to 14) the migration distance of the positively charged NP species towards the cathode decreased, as adsorption of proteins not only resulted in an increase in NP size, but also led to a reduction of the positive ζ -potential. After iodine staining, an additional faintly fluorescent band was visible that could be attributed to BSA-bound dye (Figure 8B). Formation of negatively charged NP species and cargo leaching was most pronounced for samples incubated with FCS (lane 15 and 16) as a full hetero-multilayer corona was formed. The amount of positively charged NP species, negatively charged NP species as well as the fraction of protein-bound dye was further quantified by analyzing the intensities of the fluorescent bands before and after iodine staining.

As shown in Figure 8C, samples incubated with BSA or FCS showed a different species pattern compared to freshly prepared NP510N (lane 5 and 6) and NPs incubated in DPBS (lane 7 and 8). The fraction of positively charged NP species decreased, whereas the fraction of negatively charged NP species significantly increased ($p < 0.05$) upon incubation with higher amounts of BSA. The fraction of protein-bound cargo significantly increased with higher protein concentration from 0% (no BSA) to 1.7% (90 mg mL⁻¹ BSA), however, differences were not significant. NP510N incubated with FCS displayed the highest degree of cargo leaching (3.0%) when multiple different biomolecules were involved in the development of the hard and soft protein corona.

Transmission electron microscopy was used to assess changes in particle core size, size distribution and morphology of NP510N upon incubation with BSA. To this end, NP510N were incubated in PBS pH 7.4 supplemented with 90 mg mL⁻¹ BSA for 5 hours. Buffer salts and unbound BSA were removed by dialysis against ultrapure water using a dialysis membrane (100 kDa MWCO). NPs that were freshly prepared in ultrapure water and subsequently applied onto a carbon-coated copper grid served as reference. Both samples displayed a comparable core size distribution as depicted in Figure 9.

The size of NP510N incubated with BSA was slightly shifted towards larger core diameters due to the adsorption of albumin onto the colloidal surface.

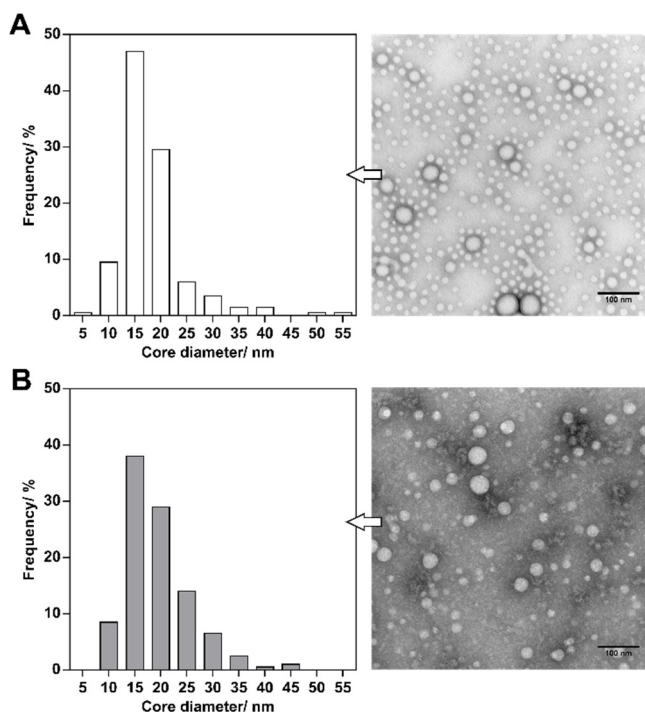


Figure 9. Size and morphology of NP510N was analyzed by TEM (A) immediately after preparation (B) and after incubation with 90 mg mL^{-1} BSA for 5 hours at 37°C following dialysis to remove unbound proteins and buffer salts. Scale bars indicate 100 nm. Particle size frequency distribution was determined from 200 particles.

Furthermore, the reduction in counts of small polymeric NPs ($< 7.5 \text{ nm}$) may also result from the purification procedure, as those NPs possess a similar size as albumin (d_H of approximately 7 nm) [206] and consequently, can pass through the dialysis membrane [207]. As DLS results (cf. Figure S2) did not indicate any significant changes in size or polydispersity, disassembly of small polymeric micelles is rather unlikely and therefore negligible. The cloudy spots that could be observed in the TEM images of NP510N incubated with BSA (Figure 9B) most probably derive from insoluble BSA aggregates or from residual phosphate salts that can react with uranyl acetate to insoluble uranyl phosphate [208].

4 Conclusion

In this study, functionalized polymeric NPs with different surface charge and hydrophobicity were evaluated regarding their interaction with serum proteins and its impact on their colloidal stability and cargo leaching. From the quantitative and qualitative analysis of the hard protein corona it was concluded, that zwitterionic NPs were least affected by the development of a protein corona as this NP formulation provides only limited opportunities for serum proteins to interact *via* electrostatic or hydrophobic interactions compared to polymeric colloids functionalized with uncharged methoxy-groups or negatively charged carboxylate groups. In contrast, positively charged NPs displayed an enhanced interaction with serum proteins resulting in a diverse range of different proteins that were part of the hard corona. This enhanced interaction also significantly impaired the colloidal integrity as the lipophilic cargo was continuously leached out of the hydrophobic NP core. Agarose gel electrophoresis revealed that cargo leaching directly correlated with the protein concentration and that the identity of amine-decorated NPs was significantly altered upon incubation with albumin, leading to the formation of negatively charged NP species. Cargo leaching was identified to be a two step process as the cargo was first redistributed from the particle core to proteins adsorbed onto the colloidal surface, followed by the final escape through desorption of the protein carrier from the particle. In summary, these findings highlight the importance of generating a profound knowledge of the protein corona, as it can bestow a new biological identity to NPs and moreover, severely impair NP integrity.

Ligand density and linker length are critical factors for multivalent nanoparticle-receptor interactions

Abstract

Although there are a large number of studies available evaluating the therapeutic efficacy of targeted polymeric nanoparticles, little is known about the critical attributes that can further influence their uptake into target cells. In this study, varying cRGD ligand densities (0 - 100% surface functionalization) were combined with different PEG spacer lengths (2/3.5/5kDa) and the specific receptor binding of targeted core/shell structured PLGA/PLA-PEG nanoparticles was evaluated using $\alpha_v\beta_3$ integrin overexpressing U87MG glioblastoma cells. Nanoparticles with 100% surface functionalization and short PEG2k linkers displayed a high propensity to form colloidal clusters, allowing for the cooperative binding to integrin receptors on the cellular membrane. In contrast, the high flexibility of longer PEG chains enhanced the chance of ligand entanglement and shrouding, decreasing the number of ligand-receptor binding events. As a result, the combination of short PEG2k linkers and a high cRGD surface modification synergistically increased the uptake of nanoparticles into target cells. Even though to date, the nanoparticles size and its degree of functionalization are considered to be major determinants for controlling the uptake efficiency of targeted colloids, these results strongly suggest that the role of the linker length should be carefully taken into consideration for the design of targeted drug delivery formulations in order to maximize the therapeutic efficacy and minimize adverse side effects.

1 Introduction

Over the past decades, tethering of targeting moieties to core/shell structured polymeric nanoparticles (NPs) has become a well-established strategy to precisely control the interaction between ligand-decorated NPs and target cells. By this rational design, colloidal drug delivery systems can be tailored to selectively deliver therapeutic cargos to the site of action, maximizing the therapeutic efficacy and significantly reducing the incidence of adverse side effects [161].

Although NP size [209,210] and surface functionalization with high-affinity ligands [11,211] are widely considered to be the most important key factors, it is generally accepted that the targeting capability can be further optimized by precisely tailoring the properties of ligand-decorated NPs, such as ligand density, size, charge, hydrophobicity or shape [59-61,212,213]. For example, a high degree of colloidal surface functionalization with ligands or a worm-like shape of ligand-decorated NPs generally result in an enhanced recognition of target cells by virtue of multivalent receptor binding, given that the receptor density on the cellular membrane is sufficiently high. Moreover, recent studies on targeted drug delivery into cells have highlighted the importance of particle size. Although NPs in the size range of tens to hundreds of nanometers can be internalized by cells *via* wrapping, the optimal NP size range for cell entry was identified to be 50 to 100 nm [64,65]. To optimize the design of colloidal drug delivery systems, a profound knowledge of all key attributes affecting the ligand's affinity and thus, the targeting efficiency, is of utmost importance. However, the majority of recent studies focusing on the optimization of targeting strategies have only evaluated a single key attribute, neglecting the fact that these contributing factors mutually influence each other.

Poly(ethylene glycol) (PEG) is one of the most prominent linkers used for ligand tethering as PEG is known to enhance the colloidal stability and reduce serum protein adsorption *in vivo* [15,214]. Moreover, modification of NPs with polymer layers increases the particle size as a function of linker length and grafting density. On the other hand, polymer linkers reduce the propensity of NPs to aggregate and thus have an indirect influence on the actual colloidal size. Although it is known that the length of the PEG linker plays a pivotal role in regulating the unspecific NP uptake [215], the effect of the linker length is not sufficiently taken into consideration for the development of targeted nanocarriers. Furthermore, the delicate mutual influence of

Chapter 5: Ligand density and linker length are critical targeting factors

ligand density and linker length is not fully understood yet. Therefore, an extensive investigation of NP uptake as a combinational dependency of the surface functionalization degree and the linker length is needed to better understand the interaction of ligand-decorated nanoscaled colloids with the targeting receptors.

For this purpose, cyclic RGD (cRGD) was selected as ligand because it is already well-established as a targeting moiety and has been routinely used in uptake studies due to its high affinity towards $\alpha_v\beta_3$ and $\alpha_v\beta_5$ integrin receptors [81-83,216]. Moreover, binding of cRGD to the integrin receptor triggers endocytosis of the NP-receptor complex [217], which is indispensably required if a cargo has to be delivered into the cell to achieve a therapeutic effect.

Polymeric NPs consisting of poly(lactic-co-glycolic acid) (PLGA) and amphiphilic poly(lactic acid)-poly(ethylene glycol) (PLA-PEG) were considered ideal for this study as they are biodegradable, biocompatible and could also be used as a carrier to deliver drugs. Furthermore, the block copolymers can be pre-modified with ligands or fluorescent tags and the blending of different polymers allows for a precise tailoring of NP composition, which is of particular importance if the ligand density has to be controlled during the NP manufacturing process.

In this study, the contribution of the ligand density and the PEG linker length on the integrin binding kinetics and uptake efficiency of cRGD-decorated polymeric colloids was evaluated using $\alpha_v\beta_3$ integrin overexpressing U87MG glioblastoma cells as model cell line. To this end, PLA-PEG copolymers consisting of carboxylic acid terminated short (2kDa), medium (3.5kDa) or long (5kDa) PEG blocks and a constant PLA part (10kDa) were synthesized and the ligand was covalently attached to the carboxylic acid function of the PEG chain. In the first part, polymeric NPs with either short, medium or long PEG-linkers and different cRGD densities were prepared by nanoprecipitation of polymer blends consisting of constant amounts of PLGA and different feed ratios of PLA-PEG-COOH (2kDa, 3.5kDa or 5kDa PEG) and corresponding PLA-PEG-cRGD copolymers and NPs were evaluated regarding their physicochemical characteristics, such as their actual ligand density, ζ -potential, colloidal size and morphology.

In the second part, the influence of the ligand density and PEG-linker length on the integrin receptor binding efficiency was assessed by flow cytometry using $\alpha_v\beta_3$ integrin overexpressing U87MG glioblastoma cells as model cell line. In the last part, the uptake kinetics of fully functionalized NPs as a function of PEG linker length was analyzed by

flow cytometry and confocal laser scanning microscopy to evaluate the time-dependent internalization and cellular distribution of the different targeted NP formulations.

2 Materials and methods

2.1 Materials

1,4-Diazabicyclo[2.2.2]octane hydrochloride (DABCO), 1,8-Diazabicyclo[5.4.0]undec-7-ene (DBU) solution, 3,6-Dimethyl-1,4-dioxane-2,5-dione (Lactide), 4-(4,6-Dimethoxy-1,3,5-triazin-2-yl)-4-methylmorpholinium chloride (DMTMM), N-(3-Dimethylaminopropyl)-N'-ethylcarbodiimide (EDC), N-hydroxy-succinimide (NHS), N,N-Diisopropylethylamine (DIPEA), CFTM 488A amine and CFTM 647 amine, anhydrous N,N-Dimethylformamide (DMF), anhydrous dichloromethane (DCM), methoxy poly(ethylene glycol) with a molecular mass of 5000 g mol⁻¹ (mPEG5k) and Resomer® RG 502 (PLGA) were received from Sigma-Aldrich (Taufkirchen, Germany). Hydroxyl poly(ethylene glycol) carboxylic acid with a molecular mass of 2000, 3500 and 5000 g mol⁻¹ (COOH-PEG-OH) was provided by JenKem Technology USA Inc. (Allen, TX, USA). Cyclic RGDfK (cRGDfK) was purchased from SynPeptide Co. Ltd (Shanghai, China). All other materials were reagent grade and obtained from Merck KGaA (Darmstadt, Germany). Ultrapure water was freshly prepared using a Milli-Q water purification system (Millipore, Schwalbach, Germany).

2.2 Fluorescent labeling of PLGA (PLGA-CF488/-CF647)

PLGA was dissolved in anhydrous DMF and the carboxylic acid group was activated by the addition of DMTMM for two hours. Afterwards, 0.1 equivalents of an amine-functionalized dye (CFTM 488A amine or CFTM 647 amine) were added and stirred overnight to yield PLGA-CF488A and PLGA-CF647. To remove any unreacted dye, fluorescently labeled PLGA was purified by several precipitation steps in methanol (2x) and water (1x), followed by dialysis against water and lyophilization of the polymer conjugate.

2.3 Synthesis of PLA-PEG-COOH

PLA-PEG-COOH block copolymers (10k-b-2k, 10k-b-3.5k, 10k-b-5k) were synthesized by a ring-opening polymerization as previously described in literature [170]. Linear hydroxyl poly(ethylene glycol) carboxylic acid with a molecular mass of 2000, 3500 and 5000 g mol⁻¹ was used as macroinitiator for the ring-opening polymerization of lactide using DBU as catalyst. ¹H-NMR (CDCl₃, 300 Hz) was used to characterize the precursor PLA-PEG-COOH polymers (10k-b-2k, 10k-b-3.5k, 10k-b-5k) and calculate the degree of polymerization.

2.4 Synthesis of PLA-PEG-cRGD

Cyclo(RGDfK) was covalently conjugated to carboxy-modified PLA-PEG block copolymers *via* the lysine residue of the cyclic peptide [60] (Figure 1). First, the carboxylic acid function of PLA-PEG-COOH was activated by EDC (25 equiv) and NHS (25 equiv) for 2 hours in anhydrous DMF. Then, BME (30 equiv) was added to quench the reaction. DIPEA (10 equiv) and cRGDfK (3 equiv) were subsequently added and stirred for 24 hours. The ligand-modified copolymer was purified by several precipitation steps in diethyl ether/ methanol mixtures, followed by dialysis against water for 24 hours to remove excess free ligand and reactants.

2.5 Preparation of polymeric nanoparticles

For the manufacture of nanoparticles (NPs) consisting of PLA-PEG_{5k}-COOH and PLGA (NP-cRGD_{0-5k}), polymers were diluted with acetonitrile to a final polymer concentration of 10 mg mL⁻¹. The copolymer ratio of PLA-PEG to PLGA was kept constant at 70/30 (m/m). The polymer mixture was then added dropwise into 10 volumes of DPBS (75 mM, pH 7.4) while stirring. NP dispersions were stirred for 3 hours to evaporate the organic solvent. NPs were concentrated by centrifugation at 2500 g for 15 min using Pall Microsep® filters (MWCO 100 kDa).

For different cRGD ligand densities and varying PEG linker length, PLA-PEG-COOH was substituted with different amounts of PLA-PEG-cRGD. The copolymer ratio of PLA-PEG to PLGA was continuously adjusted to obtain particles with consistent molarities of PLA-PEG and PLGA, resulting in a constant molar ratio of PEG chains per fluorescence tags.

2.6 Dynamic light scattering and ζ -potential

The size of all NP formulations was analyzed on a Malvern Zetasizer Nano ZS (Malvern, Herrenberg, Germany) equipped with a 633-nm He-Ne laser and operating at an angle of 173°. Samples were measured at a constant temperature of 25 °C in either 75 mM (DLS) or 15 mM (ζ -potential) PBS pH 7.4. Semi-micro PMMA disposable cuvettes (Brand, Wertheim, Germany) were used for size measurements and folded capillary cells (Malvern, Herrenberg, Germany) were utilized for the ζ -potential determination. The position from the cuvette wall was set to 4.65 mm and the attenuator was optimized by the device. Data were collected and analyzed using the Malvern Zetasizer software version 7.11 (Malvern Instruments, Worcestershire, United Kingdom).

2.7 Transmission electron microscopy

The size and aggregation behavior of functionalized NPs were evaluated on a Zeiss 902 (80 kV) transmission electron microscope (Zeiss, Oberkochen, Germany). NP-cRGD₁₀₀-2k, NP-cRGD₁₀₀-3.5k and NP-cRGD₁₀₀-5k were prepared in DPBS (75 mM, pH 7.4), stirred for 3 hours to remove the organic solvent and subsequently dialyzed against ultrapure water to remove buffer salts. NP samples (50 $\mu\text{g mL}^{-1}$) were applied onto carbon-coated copper grids (300 mesh; Plano, Wetzlar, Germany), incubated for 5 minutes and negatively stained with 1% uranyl acetate solution. Excess sample solution was removed with a filter paper and sample grids were dried and stored in a desiccator before use.

2.8 Nanoparticle quantification by an iodine assay (IA)

Three batches of nontargeted NPs (NP-cRGD₀-5k) consisting of PLA-PEG_{5k}-COOH and PLGA were prepared in ultrapure water, purified and concentrated as described above. A colorimetric iodine complexation assay [192] was used to quantify the exact amount of PEG. In brief, NP samples were diluted in ultrapure water to a final PEG concentration of approximately 2.5 to 50 $\mu\text{g mL}^{-1}$. Dilutions of methoxy poly(ethylene glycol) with a molecular mass of 5000 g mol^{-1} (mPEG5k) were used as calibration standards (0 - 50 $\mu\text{g mL}^{-1}$). Two parts of a solution containing 5% (m/v) barium chloride in 1 N HCl were mixed with 1 part of a 0.1 N iodine/ potassium iodide solution immediately before use. 140 μL of sample and standard dilutions were transferred into

Chapter 5: Ligand density and linker length are critical targeting factors

a 96-well plate, mixed with 60 μL of the iodine reagent and incubated for 15 min at room temperature. Absorbance was measured at 535 nm using a FluoStar Omega fluorescence microplate reader (BMG Labtech, Ortenberg, Germany). The exact polymer concentration was determined gravimetrically after lyophilization of the concentrated NP samples and plotted against the PEG content determined by the iodine assay. As the PEG content of each particular formulation was considered to be constant, from this point on, the PEG content of freshly prepared samples was determined against the mPEG5k standard and used to calculate the polymer concentration (Figure S3).

For different cRGD ligand densities and varying PEG linker lengths, the PEG content was analyzed and diluted to attain equal molarities of PEG in each formulation.

2.9 Phenanthrenequinone Assay (PCA)

The cRGDfK content of different NP formulations was determined by quantification of the arginine content as described previously [83]. In brief, NP samples were diluted in ultrapure water to a final polymer concentration of approximately 1 mg mL⁻¹. Dilutions of cRGDfK (0 - 40 $\mu\text{g mL}^{-1}$) were used for calibration. Then, 6 parts of a 9,10-phenanthrenequinone solution (150 μM in ethanol) were mixed with 1 part of 2 N NaOH. 50 μL of sample or standard solutions were mixed with 175 μL of the phenanthrenequinone reagent solution and incubated at 60 °C for 3 hours. 125 μL aliquots were transferred into a 96-well plate, mixed with 125 μL 1 N HCl and incubated at room temperature for 1 hour. Fluorescence was excited at 312 nm and emission was recorded at 395 nm using a PerkinElmer LS 55 Fluorescence spectrometer (Perkin Elmer, Wiesbaden, Germany). The surface functionalization degree (SFD) for each NP formulation was calculated using equation 1.

$$\text{SFD [\%]} = \frac{\text{concentration of cRGDfK}_{\text{PCA}} [\mu\text{M}]}{\text{concentration of PEG}_{\text{IA}} [\mu\text{M}]} \cdot 100 \quad (1)$$

2.10 Determination of the PEG grafting density and ligand density

The PEG grafting density and the ligand density were calculated as previously described in literature [174,218]. The absolute ligand density (number of peptide-conjugated PEG molecules per μm^2) was calculated based on the SFD and PEG

grafting density (PEG chains per nm²) which was obtained by relating the number of PEG molecules (calculated based on $M_{W(PEG)}$, wt % of PEG in PLA-PEG determined by ¹H-NMR and the theoretical NP composition) to the surface area ($S_{(NP)}$) and NP volume ($V_{(NP)}$) using a density ($\rho_{(NP)}$) of 1.2 g cm⁻³:

$$\text{PEG grafting density} = \frac{\text{wt \%} \times V_{(NP)} \times \rho_{(NP)} \times N_A}{M_{W(PEG)} \times S_{(NP)}} \quad (2)$$

where $S_{(NP)}$ and $V_{(NP)}$ are calculated using the z-average diameter of the NP distribution, $M_{W(PEG)}$ is the PEG average molecular weight according to the specification sheet provided by the manufacturer, and N_A is the Avogadro's number.

2.11 Flow cytometry assessment of cellular uptake

To quantify the cellular uptake of CFTM647-labeled NPs with different PEG spacer lengths and different surface functionalization degrees, flow cytometry experiments were performed. Particle concentrations were adjusted to equal PEG molarities per sample, corresponding to 200 µg mL⁻¹ of NP-cRGD₀-5k as reference. U87MG cells were seeded into collagen-coated 24-well plates at a density of 80,000 cells per well and cultured for 72 h. NP test solutions were prepared in TRIS binding buffer (20 mM TRIS, 150 mM NaCl, 2 mM CaCl₂, 1 mM MgCl₂, 1 mM MnCl₂, 0.1% BSA) supplemented with 10% FCS and incubated for 15 min at 37 °C to induce the formation of a protein corona and cells were subsequently treated with NP solutions for 45 min at 37 °C. To evaluate the binding kinetics of cRGD-decorated nanoparticles with different PEG linker lengths (NP-cRGD-2k, NP-cRGD-3.5k and NP-cRGD-5k), incubation times were varied from 15 to 180 minutes. For the control experiment, an excess of cRGDfK (500 µM) was used to suppress binding to the $\alpha_v\beta_3$ receptor. After incubation, cells were washed with DPBS, trypsinized and centrifuged at 200 g for 5 min and washed once with DPBS. Cells were suspended in 200 µL DPBS and cellular fluorescence was analyzed with a FACSCalibur flow cytometer (Becton Dickinson, Franklin Lakes, USA) using a 633 nm laser for excitation and a 670 nm long pass (LP) filter for detection. Resulting data were evaluated using the Flowing Software v2.5 (Turku, Finland).

2.12 Confocal laser scanning microscopy

To analyze the NP binding pattern on cells, confocal microscopy was conducted. U87-MG cells were seeded into collagen-coated 8-well Chamber Slide™ systems (Lab-Tek®) at a density of 15,000 cells/well and cultivated for 48 h. CF™ 488A-labeled sample solutions were prepared in RGD binding buffer (20 mM TRIS, 150 mM NaCl, 2 mM CaCl₂, 1 mM MgCl₂, 1 mM MnCl₂, 0.1% BSA) supplemented with 10% FCS and incubated for 15 min at 37 °C to induce the formation of a protein corona. Cells were treated with the pre-warmed NP test solutions for either 15 or 60 min at 37 °C. Then, cells were washed, fixed with 2% paraformaldehyde in DPBS for 10 min at room temperature and washed extensively with DPBS. Samples were embedded in Mowiol aqueous embedding medium supplemented with 2.5% (w/v) DABCO and analyzed with a Zeiss Axiovert 200 microscope combined with an LSM 510 laser-scanning device at 63-fold magnification. NP fluorescence was excited with an argon laser at 488 nm and the emission was recorded using a 530/30 nm bandpass (BP) filter.

2.13 Statistical analysis

All results are presented as mean ± standard deviation, based on the data obtained from at least $n = 3$ samples. Statistical significance was determined by means of one-way ANOVA, followed by Tukey's *post-hoc* test using GraphPad Prism 6.0 (GraphPad Software Inc., La Jolla, CA, USA). Statistical significances were set as indicated.

3 Results and discussion

3.1 Preparation of NPs with different surface functionalization

To allow for precise tuning of the NP composition, a set of block copolymers with distinct molecular weights was first synthesized and conjugated with cRGD ligands. Carboxylic acid terminated PLA-PEG block copolymers with constant PLA blocks and different PEG lengths (10k-b-2k, 10k-b-3.5k, 10k-b-5k) were prepared by a catalyzed ring opening polymerization and the resulting block copolymers were then modified with cRGD by EDC/NHS chemistry (Figure 1A). PLGA was labeled with a fluorescent dye (CF488A or CF647) to enable tracing of polymeric colloids in *in vitro* experiments (Figure 1B). To investigate the influence of ligand density and PEG-linker length on the

cellular uptake into U87MG glioblastoma cells, polymeric NPs with either a short, medium or long PEG-linker length and with tunable cRGD densities were manufactured (Figure 1C) by changing the set of PLA-PEG block copolymers (10k-b-2k, 10k-b-3.5k, 10k-b-5k) and the feed mass ratio of PLA-PEG-cRGD and PLA-PEG-COOH (0/100, 25/75, 50/50, 75/25 or 100/0). The corresponding NP samples were defined as NP-cRGD_x-2k, NP-cRGD_x-3.5k or NP-cRGD_x-5k to distinguish between the linker length and as NP-cRGD₀, NP-cRGD₂₅, NP-cRGD₅₀, NP-cRGD₇₅, NP-cRGD₁₀₀ to define the surface functionalization degree.

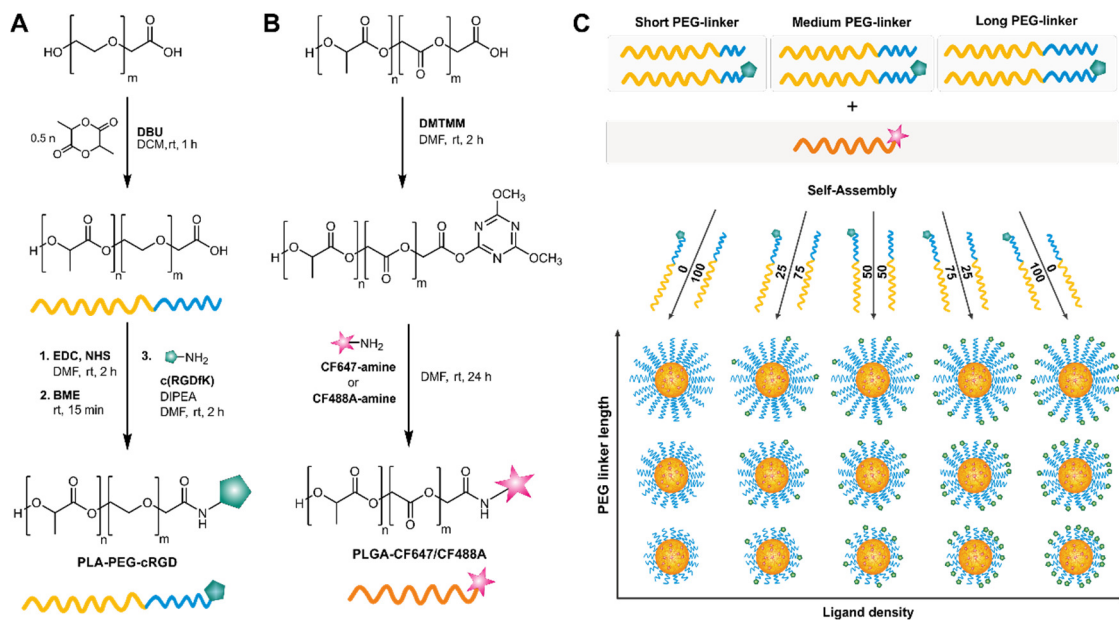


Figure 1. Synthesis strategies for the block copolymers and preparation of the NPs. (A) Synthesis of PLA-PEG-COOH (10k-b-2k, 10k-b-3.5k, 10k-b-5k) copolymers and conjugation of c(RGDfK) using EDC/NHS chemistry. (B) Conjugation of fluorescent dyes (CF647/CF488A) to carboxylic acid terminated PLGA using DMTMM. (C) Preparation of NP formulations with different ligand densities and different PEG-spacer lengths by blending constant amounts of PLGA with different mass ratios of PLA-PEG-COOH (10k-b-2k, 10k-b-3.5k, 10k-b-5k) and corresponding PLA-PEG-cRGD copolymers.

3.2 Characterization of nanoparticles

To confirm the correlation between predicted and actual ligand density, the molar amounts of PEG and cRGD were quantified with an iodine complexation assay and a

Chapter 5: Ligand density and linker length are critical targeting factors

9,10-phenanthrenequinone assay, respectively. The surface functionalization degree of each NP formulation was calculated using equation 1. As depicted in Figure 2 the predicted cRGD density highly correlated with the experimentally determined ligand density ($R^2 = 0.9975$, 0.9888 and 0.9980) confirming that the pre-modification of block polymers and the manufacturing process allow for a precise tailoring of the surface composition of polymeric PLGA blended PLA-PEG NPs.

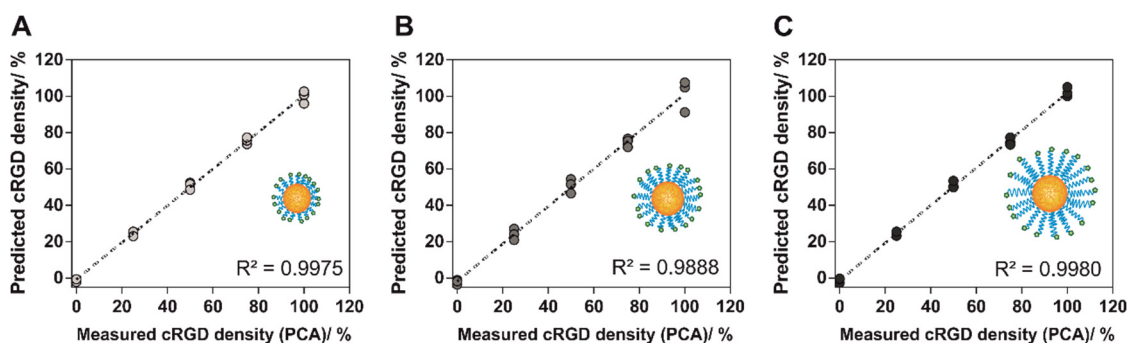


Figure 2. Correlation of predicted and measured ligand density. (A) NP-cRGD-2k, (B) NP-cRGD-3.5k, (C) NP-cRGD-5k. The amount of peptide was determined by a 9,10-phenanthrenequinone assay and the amount of PEG was analyzed using an iodine complexation assay.

Furthermore, all NP formulations were analyzed with regard to their size and ζ -potential. Modification of the colloidal surface with increasing amounts of cRGD ligands generally resulted in a consecutive increase in the hydrodynamic diameter and also in the ζ -potential (towards less negative values). While the increase in the hydrodynamic diameter was only minor for NPs with long PEG5k-linkers (38.4 to 54.1 nm), the increase in size was even more pronounced for NPs with medium PEG3.5k-linkers (36.0 to 97.3 nm) and short PEG2k-linkers (43.3 to 171.9 nm) when the surface functionalization degree was 100% compared to the respective unmodified counterparts. In contrast, the ζ -potential became less negative upon conjugation of the carboxylic acid groups with cRGD, also indicating that the coupling reaction was successful and that less charged groups are available on the surface. TEM images of NP-cRGD₁₀₀-2k (Figure 3G), NP-cRGD₁₀₀-3.5k (Figure 3H) and NP-cRGD₁₀₀-5k (Figure 3I) revealed that the increase in size measured by DLS was not a result of an actual enlargement of the particle size, but of a higher tendency of spherical NPs with

short and medium PEG-linkers to form NP clusters upon functionalization of the carboxylic acids groups on the colloidal surface with the peptide (Figure S4). The clustering tendency was also reflected in the number-weighted size distribution patterns obtained by DLS (cf. Figure S5).

In case of NP aggregation, the specific surface area per cluster volume decreases. Since these polymeric NPs generally have a negatively charged particle core due to unmodified carboxylic acid groups of the PLGA polymer, an increase in the apparent cluster volume also results in a more pronounced negative charge of a cluster compared to a single NPs which is opposite to the charge increase (towards a neutral charge) on account of surface modification.

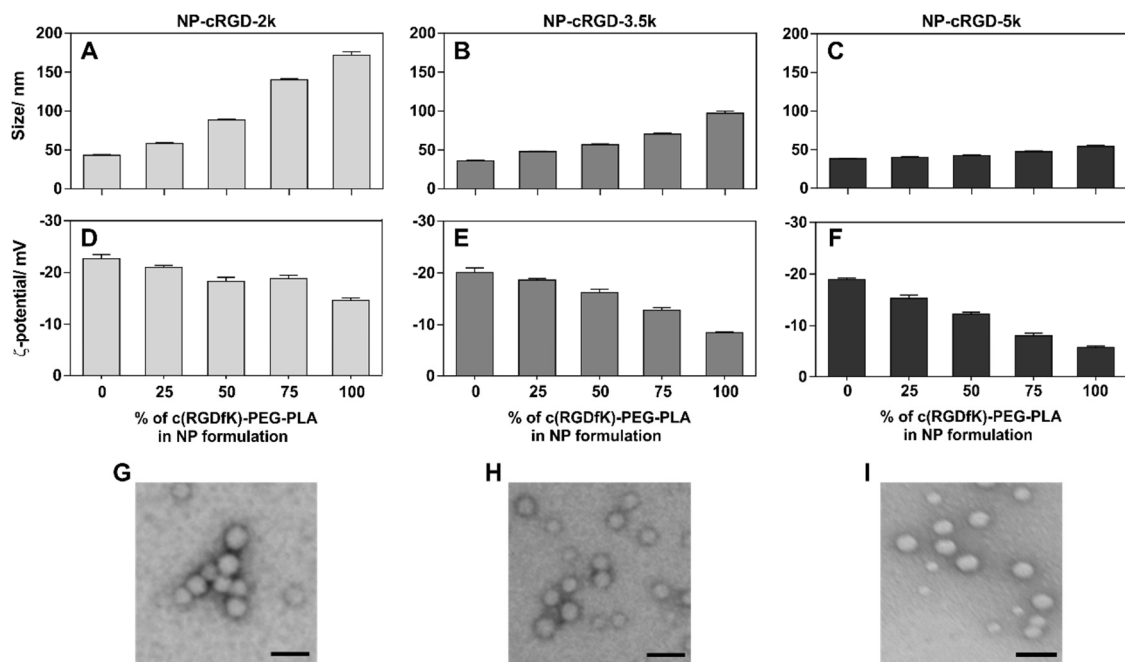


Figure 3. Characterization of different NP formulations. Hydrodynamic diameter and ζ -potential polymeric NPs with different surface functionalization degrees (0-100%) and PEG-linker lengths: (A,D) NP-cRGD-2k, (B,E) NP-cRGD-3.5k, (C,F) NP-cRGD-5k. TEM images of (G) NP-cRGD₁₀₀-2k, (H) NP-cRGD₁₀₀-3.5k and (I) NP-cRGD₁₀₀-5k demonstrating the different clustering tendencies depending on the PEG-linker length. Scale bars indicate 50 nm.

Chapter 5: Ligand density and linker length are critical targeting factors

Hence, the ζ -potential of NP-cRGD₁₀₀-2k only slightly altered from -22.7 to -14.7 mV (Δ = 8.0 mV), whereas NP modified with the medium PEG3.5k-linker and long PEG5k-linker displayed a more pronounced change in ζ -potential from -20.1 to -8.5 mV (Δ = 11.6 mV) and from -19.0 to -5.6 mV (Δ = 13.4 mV), respectively.

Interestingly, NP-cRGD₁₀₀-2k displaying the highest absolute value of the ζ -potential (-14.7 mV) compared to NP-cRGD₁₀₀-3.5k (-8.5 mV) and NP-cRGD₁₀₀-5k (-5.6 mV) possessed the lowest colloidal stability. This was mainly attributed to the fact that the ζ -potential was measured in diluted DPBS (15 mM, pH 7.4) because it is only evaluable at low salt concentrations. As the ζ -potential highly depends on ionic strength, absolute differences in ζ -potential between these formulations are expected to be even smaller in TRIS buffer that was used for uptake experiments, and are not considered to significantly influence the colloidal stability in terms of electrostatic repulsion. Moreover, PEG is known to enhance the colloidal stability by steric repulsion as a function of grafting density and linker length [189,219]. In conclusion, the decrease in electrostatic repulsion, which was reflected in a lower absolute value of the ζ -potential, was overcompensated by the enhanced steric hindrance of longer PEG linkers.

3.3 Cellular uptake and targeting of nanoparticles

In this study, polymeric NPs with distinct surface functionalization degrees and different PEG spacer lengths were prepared *via* bulk nanoprecipitation and the impact of the ligand density and the PEG spacer length on the integrin receptor binding and uptake into U87MG cells was evaluated by flow cytometry. As U87 glioblastoma cells are known to overexpress the $\alpha_v\beta_3$ receptor, which can be effectively targeted with the cyclic RGD peptide, they were used as model cell line in this study. Polymeric NPs were prepared with a constant molar ratio of PEG chains per fluorescence tags to allow for the correlation of the cellular associated fluorescence determined by flow cytometry and the relative degree of surface functionalization.

As shown in Figure 4, cellular associated fluorescence levels increased with higher cRGD surface densities of NP-cRGD-2k, NP-cRGD-3.5k and NP-cRGD-5k, indicating that higher amounts of ligands present on the colloidal surface increased the targeting efficiency towards $\alpha_v\beta_3$ integrin positive cells. The uptake of NP-cRGD-5k and NP-cRGD-3.5k into U87MG cells was similar when the relative cRGD modification was 0, 25 and 50%, but began to increase for NP-cRGD-3.5k above a surface

functionalization level of 50%. In contrast, NP formulations with a short PEG2k linker displayed an exponential increase in cell-associated fluorescence with higher degrees of surface functionalization. Compared to the other two NP formulations, the uptake of NP-cRGD-2k was significantly higher ($p < 0.01$) at surface functionalization levels of 50, 75 and 100% (Figure 4), e.g. the cell-associated fluorescence of NP-cRGD₁₀₀-2k (365.7 a.u.) was 3.7 and 5.7 times higher compared to NP-cRGD₁₀₀-3.5k (98.0 a.u.) and NP-cRGD₁₀₀-5k (64.0 a.u.), respectively.

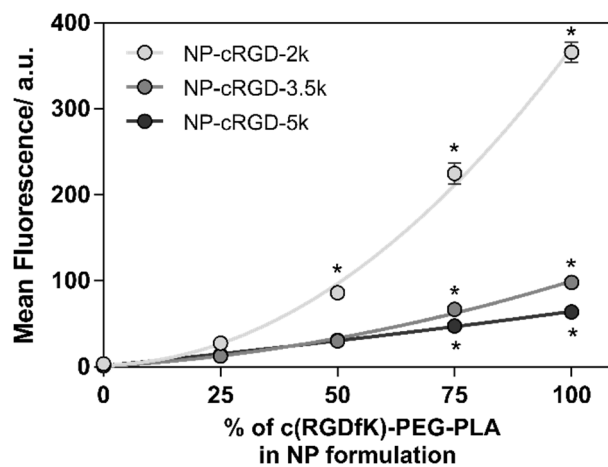


Figure 4. Integrin receptor mediated uptake of polymeric NPs modified with different degrees of surface functionalization (0-100 %) and PEG-linker lengths (2kDa, 3.5kDa, 5kDa) determined by flow cytometry. Data were fitted with a second order polynomial. Levels of significance are indicated as: (*) $p < 0.01$, comparing polymeric NPs with an equal surface functionalization degree.

Interestingly, the relation of ligand density and uptake efficiency of NP-cRGD-2k and NP-cRGD-3.5k could be described using a second order polynomial function, with the coefficients of determination being 0.9966 and 0.9948, respectively. In contrast, the surface functionalization dependent uptake of NPs decorated with long PEG5k linkers (NP-cRGD-5k) could not only be fitted with a second ($R^2 = 0.9988$), but also with a first order polynomial ($R^2 = 0.9968$). In the case of NP-cRGD-2k and NP-cRGD-3.5k the relation between NP uptake and the degree of surface functionalization did not follow a first order polynomial equation (Table 1), indicating that for NP-cRGD-2k and

Chapter 5: Ligand density and linker length are critical targeting factors

NP-cRGD-3.5k there is more than one contributing key factor influencing the receptor binding efficiency.

Table 1: Surface functionalization degrees of different NP formulations were correlated with corresponding cell-associated fluorescence levels. Data were fitted with a first and second order polynomials.

Formulation	First order polynomial	R ²	Second order polynomial	R ²
NP-cRGD-2k	$y = -42.9 + 3.69x$	0.9205	$y = 1.89 + 0.103x + 0.0359x^2$	0.9966
NP-cRGD-3.5k	$y = -7.90 + 0.992x$	0.9565	$y = 0.489 + 0.321x + 0.0671x^2$	0.9948
NP-cRGD-5k	$y = -0.0840 + 0.633x$	0.9968	$y = 1.12 + 0.537x + 0.000959x^2$	0.9988

As demonstrated earlier, NPs with short and medium PEG spacer length exhibited a higher tendency to form colloidal clusters, resulting in a higher apparent particle size. Based on the z-average size of NPs and clusters as determined by DLS, the absolute ligand density per μm^2 was calculated for each NP formulation (Figure S6) and the cellular associated fluorescence was plotted against the calculated ligand density per μm^2 . As shown in Figure 5, the mean fluorescence directly correlated with the absolute ligand density for all three NP formulations (Table S1), which implies that the integrin-mediated cellular uptake highly depends on the absolute ligand density expressed as ligands per μm^2 .

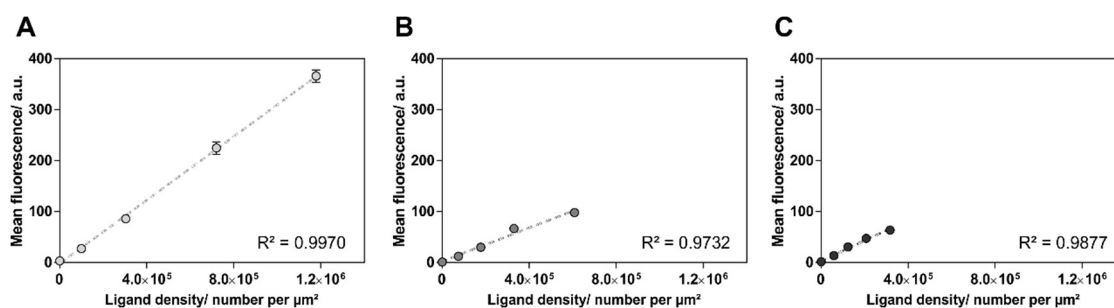


Figure 5. NP binding to U87MG cells as a function of absolute ligand densities (number of peptide-conjugated PEG molecules per μm^2) in different NP formulations. (A) NP-cRGD-2k, (B) NP-cRGD-3.5k and (C) NP-cRGD-5k.

For NP-cRGD-2k, the slope of the fitted straight line was higher (0.0003116) than for NP-cRGD-3.5k (0.0001645) and NP-cRGD-5k (0.0001995), indicating that in the case of medium and long PEG linkers, not all of the tethered cRGD ligands are available on the NP surface. It has already been reported in the literature that molecules conjugated to PEG linkers can be entangled by the polymer and may not be available for ligand-receptor interactions [54]. As a result, the affinity of the ligand towards the receptor is severely impaired. This ligand shrouding effect is highly depending on the molecular weight of the linker as the flexibility of PEG chains increases with higher polymerization degrees [220]. Interestingly, the change in ζ -potential deriving from the progressing surface modification had no effect on binding efficiency at all. This observation was further confirmed by a control experiment in which unmodified control NPs with different ratios of methoxy- and carboxylic acid terminated PLA-PEG copolymers were used to imitate the conversion of the charged groups on the surface to neutral conjugates (cf. Figure S7).

Furthermore, the relation of fluorescence levels and ideal ligand densities, meaning that the ligand density of cRGD-decorated NPs corresponding to the PEG grafting density multiplied with the surface functionalization degree, could not be described with a first order polynomial (with the exception for NP-cRGD-5k, showing no significant cluster formation) but instead, followed a second order polynomial. This finding indicates, that the effective ligand density of NP clusters is affected by rearrangement of PEG linkers upon cluster formation, which results in a higher ligand density on the surface of clustered NPs that are available for binding to $\alpha_v\beta_3$ integrin receptors (Figure S8).

In summary, the clustering tendency and ligand density both have a major impact on integrin mediated uptake of NPs. However, both of these determinants are highly influenced by PEG linker length, even if the functionalization degree is controlled by the relative amount of ligand-conjugated PLA-PEG copolymer used for preparation of polymeric NPs.

3.4 Uptake kinetics of nanoparticles with different linker lengths

In the previous section it was shown that both factors, the ligand density and the linker length, are critical attributes that have a major influence on the multivalent nanoparticle-receptor interaction. As fully modified NP-cRGD₁₀₀-2k, NP-cRGD₁₀₀-3.5k

Chapter 5: Ligand density and linker length are critical targeting factors

and NP-cRGD₁₀₀-5k showed significant differences in their clustering tendency and thus, in integrin binding efficiency, these three particular formulations were used to further investigate the integrin binding kinetics. To this end, U87MG cells were incubated with NP-cRGD₁₀₀-2k, NP-cRGD₁₀₀-3.5k and NP-cRGD₁₀₀-5k for different time periods, ranging from 15 to 180 minutes. Unmodified NP-cRGD₀-5k served as control because this formulation is not expected to be internalized *via* the specific receptor-mediated endocytosis pathway.

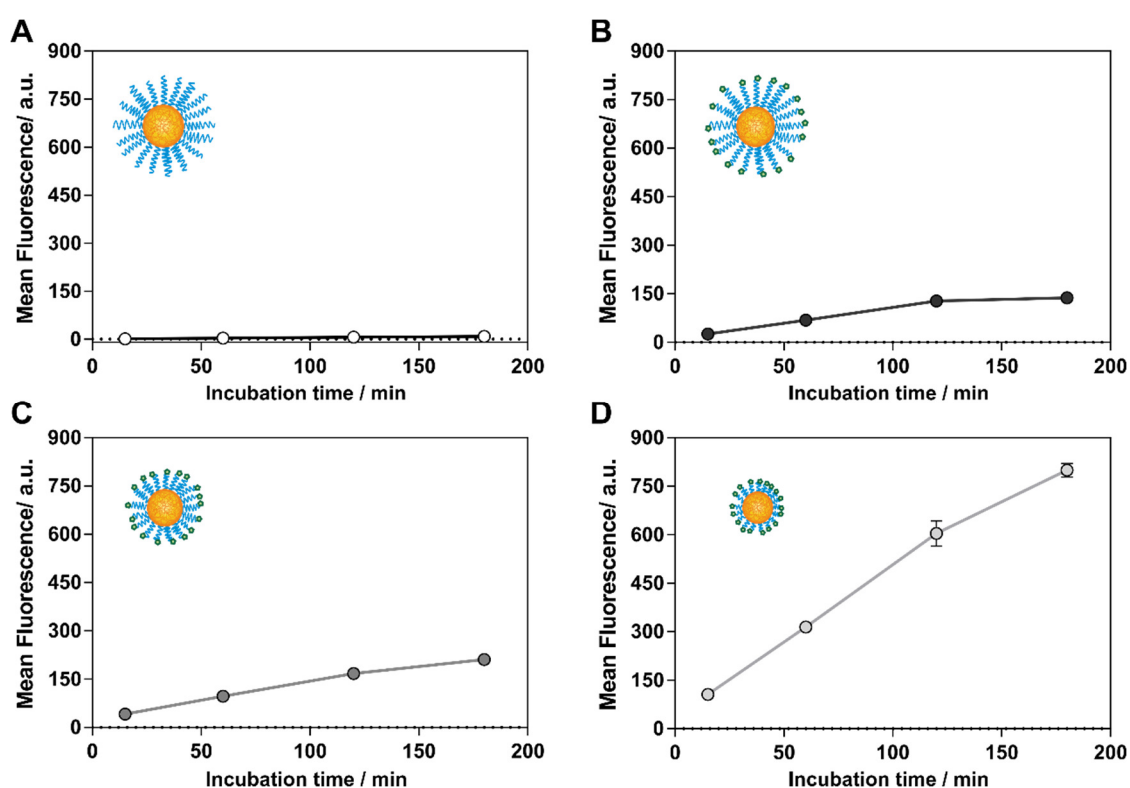


Figure 6. Binding kinetics of (A) NP-cRGD₀-5k (B) NP-cRGD₁₀₀-5k, (C) NP-cRGD₁₀₀-3.5k and (D) NP-cRGD₁₀₀-2k. U87MG cells were incubated with different NP formulations for either 15, 60, 120 or 180 minutes. Cell associated fluorescence was assessed by flow cytometry.

As demonstrated in Figure 6, all three cRGD-decorated NP formulation exhibited a linear increase in cellular associated fluorescence between 15 and 120 minutes, followed by a slightly plateaued increase between 120 and 180 minutes. Because the

growth medium is substituted with nutrient free TRIS binding buffer during the sample incubation, the receptor mediated internalization kinetics might be altered as a result of a change in the physiology of U87MG cells. Furthermore, the change in slope may also result from a saturation of receptors on the surface or a decelerated recycling process of the integrin receptors, usually undergoing a constant endo/exocytic shuttling from the endosome back to the plasma membrane [221,222]. Comparing the correlation between fluorescence and incubation time (15 - 120 minutes), the slope of the fitted straight line (Table S2) of NP-cRGD_{100-2k} was much higher (4.745 units min⁻¹) compared to NP-cRGD_{100-3.5k} (1.195 units min⁻¹) and NP-cRGD_{100-5k} (0.972 units min⁻¹).

Unmodified NP-cRGD_{0-5k} did not show a relevant binding to U87MG cells during the whole incubation timeline up to 180 minutes. As the slope is an indicator for uptake kinetics, these results clearly indicate that NPs modified with shorter PEG chains are more rapidly internalized by the cells than NP decorated with longer PEG chains. This can be explained by a thermodynamic approach: When the NP interacts with the cell membrane, there are four major determinants that contribute to the free energy of the system

$$F_{\text{sum}} = F_{\text{membrane}} + F_{\text{cytoskeleton}} + F_{\text{ligand}} + F_{\text{polymer}} \quad (3)$$

In this equation F_{membrane} is the bending energy of the cellular membrane which is related to a change in membrane curvature during endocytosis of the NPs. $F_{\text{cytoskeleton}}$ describes the change in deformation energy of the cytoskeleton or, more precisely, actin filaments. F_{ligand} represents the specific ligand-receptor interaction and F_{polymer} is the free energy of the grafted polymer chains resulting from steric repulsion between the grafted PEG chains and the cellular membrane [223]. Upon NP binding to the receptor F_{ligand} is reduced. Due to changes in curvature of the cellular membrane and the deformation of the cytoskeleton during internalization of the receptor-NP complex, F_{membrane} and $F_{\text{cytoskeleton}}$ increase, respectively. When NP-grafted PEG chains are absorbed and covered by the cellular membrane they forfeit conformational degrees of freedom, resulting in an increase in F_{polymer} . According to equation 3, endocytosis of NPs is triggered if the increment in F_{membrane} , $F_{\text{cytoskeleton}}$ and F_{polymer} is overcompensated by the decrease in F_{ligand} .

Chapter 5: Ligand density and linker length are critical targeting factors

Provided that the receptor density on the cellular membrane is sufficiently high, an increase in ligand density generally leads to a higher number of simultaneously occurring ligand-receptor binding events consequently resulting in a decrease in F_{ligand} . During the initial phase of endocytosis, the repulsive part of the particle-cell interaction is mainly governed by deformation of the cytoskeleton and membrane bending [224,225]. NP clustering can enhance the reduction of F_{ligand} by cooperative binding of ligands on NP clusters *via* multivalent ligand-receptor interactions [226] which then can trigger receptor clustering and further reduce F_{ligand} . Moreover, cooperative wrapping of NPs also lowers the free energy threshold necessary for bending the membrane (F_{membrane}) as the relative surface area of a particle cluster which has to be covered is significantly smaller compared to the sum of surface areas of independently wrapped particles [227].

In contrast to their shorter and more rigid counterparts, PEG chains with an increasing chain length possess higher flexibility. Therefore, entropic penalty paid for binding to $\alpha_v\beta_3$ integrins on the cellular membrane is significantly higher for longer PEG linker, leading to a more substantial increase in F_{polymer} of longer linkers compared to PEG2k chains [223]. In addition, PEG chains with higher flexibility also have an enhanced chance of entangling and cloaking the ligand inside the PEG shell due to partly folding on the distal end of the PEG linker [228]. As a consequence, the orientation and thus ligand presentation [229] is partially impaired, attenuating the decrease in F_{ligand} as there are less ligand-receptor binding events per area. Even though the major contribution derives from conformational entropy losses upon binding to the receptors, ligand entanglement and shrouding still constitutes a contributing factor as it hinders the association of peptides with their target receptors.

Moreover, membrane bending and deformation near a bound NP can promote further NP clustering on the membrane during endocytosis. As the membrane in the adjacent location to a bound NP is already partly deformed, it allows neighboring particles to gain more contact area. As a result, the energetic threshold of F_{membrane} and $F_{\text{cytoskeleton}}$ is reduced, which makes adjacent binding energetically favorable. This effect has been recently described for norovirus-like particles after binding to glycosphingolipids on a supported lipid bilayer [230].

To ensure that the enhanced uptake of NP clusters derived from specific NP-receptor interactions and was not solely attributed to the increase in particle size, an additional control experiment was performed. U87MG cells were either treated with

cRGD-decorated NPs or simultaneously incubated with NPs and excess of the free ligand for 15 or 60 minutes. When cells were co-incubated with targeted NPs and cRGD, the specific NP-receptor interaction was completely suppressed to fluorescence levels comparable with non-targeted control NPs (Figure 7). These results provide clear evidence that the internalization of ligand-decorated NPs was not a result of an increased unspecific uptake due to a larger effective particle size of clusters but instead, was exclusively mediated by specific ligand-receptor interactions.

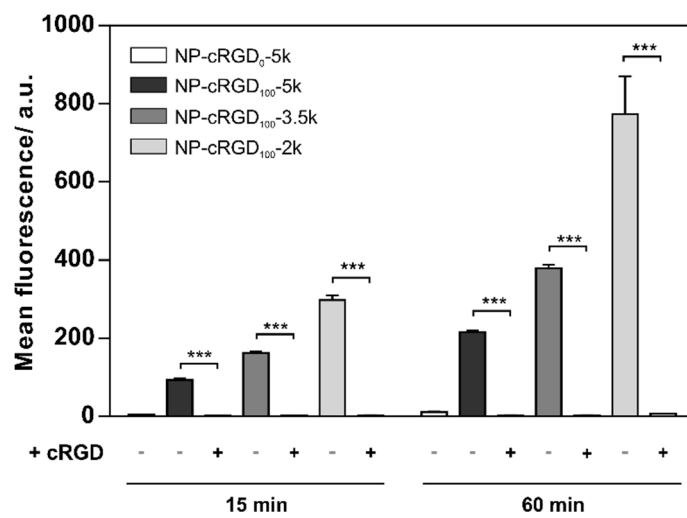


Figure 7: Cellular uptake of NP-cRGD₀-5k (non-targeted NPs), NP-cRGD₁₀₀-2k, NP-cRGD₁₀₀-3.5k and NP-cRGD₁₀₀-5k after 15 and 60 minutes. To suppress specific NP-receptor interactions, cells were simultaneously incubated with NPs and excess free ligand (500 μ M cRGDfK). Levels of significance are indicated as: (***) $p < 0.001$.

In summary, NPs decorated with cRGD tethered to short PEG2k linkers displayed a high propensity to form colloidal clusters which allow for cooperative binding to integrin receptors. Multivalent receptor binding of NP clusters decreases F_{ligand} and, in addition, lowers the energetic threshold of F_{membrane} and $F_{\text{cytoskeleton}}$. In contrast, NPs decorated with medium PEG linkers only formed smaller clusters and NP-cRGD₁₀₀-5k did not form clusters at all. Furthermore, NP-cRGD₁₀₀-3.5k and NP-cRGD₁₀₀-5k suffered from ligand entanglement which led to impairment of ligand interactions with $\alpha_v\beta_3$ receptors located on the cell membrane and consequently to a less pronounced decrease in F_{ligand} . Moreover, the overall entropic loss upon binding to the receptor was

Chapter 5: Ligand density and linker length are critical targeting factors

reduced if the ligand was conjugated to shorter PEG chains compared to medium and long PEG linkers. As a thermodynamic result, the uptake efficiency of NP-cRGD_{100-5k} was low and the uptake of NP with medium PEG3.5k spacers (NP-cRGD_{100-3.5k}) was moderate compared to NP-cRGD_{100-2k} which displayed the most efficient integrin receptor-mediated uptake (Figure 8).

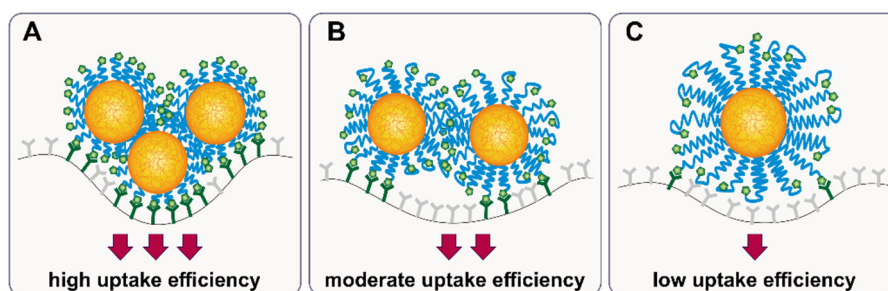


Figure 8. Schematic illustration of the $\alpha_v\beta_3$ receptors binding and cellular uptake of (A) NP-cRGD_{100-2k}, (B) NP-cRGD_{100-3.5k}, (C) NP-cRGD_{100-5k}. In general, the number of successful ligand-receptor interactions is increased through cooperative binding clustering of NPs and decreased by entanglement and shrouding of ligands.

3.5 Time-dependent cellular distribution of nanoparticles with different linker lengths

In the last part of this study, the receptor binding and cellular uptake of NPs as a function of time was assessed by confocal laser scanning microscopy (Figure 9). The objective of this experiment was to confirm, that the increase in cell-associated fluorescence determined by flow cytometry was attributed to the specific integrin receptor-mediated uptake and did not derive from non-specific adhesion to the cellular membrane. For this purpose, U87MG cells were incubated for either 15 or 60 minutes with NP-cRGD_{100-2k}, NP-cRGD_{100-3.5k} or NP-cRGD_{100-5k} and subsequently fixed with PFA. As flow cytometry results had already revealed that incubation of cells with the NP formulations resulted in different intensities of cell-associated fluorescence, microscope settings were adjusted to attain images with comparable fluorescence levels. After 15 minutes of incubation, NPs mainly accumulated on the cellular membrane and only a low amount of NPs was internalized by the cells. However, after

60 minutes of incubation, NPs were homogeneously distributed within the cytoplasm of the cells and mainly accumulated in endosomes.

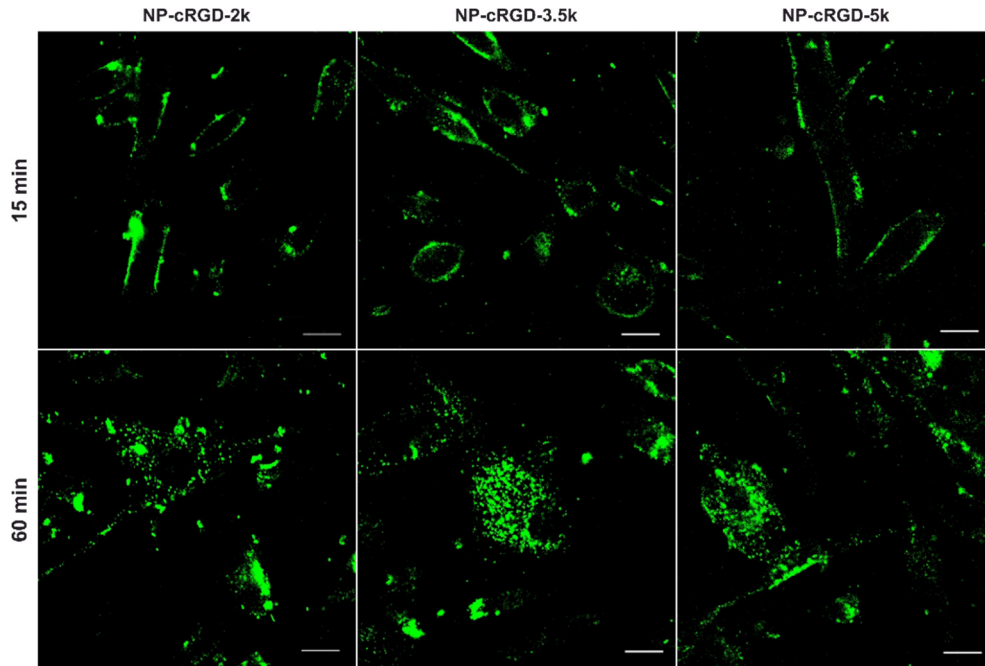


Figure 9. Evaluation of the NP localization and distribution by CLSM. Confocal images of U87MG cells treated with either NP-cRGD₁₀₀-2k, NP-cRGD₁₀₀-3.5k or NP-cRGD₁₀₀-5k for 15 or 60 minutes. To allow for comparison of all samples, microscope settings were adjusted to attain images with comparable fluorescence levels. Scale bars indicate 20 μ m.

These results are in accordance with previous studies by Sancey *et al.* who demonstrated that multivalent binding of tetrameric RGD to $\alpha_v\beta_3$ integrin receptors resulted in internalization of the ligand-receptor complex *via* clathrin-mediated endocytosis [231]. The ratio of membrane-bound to endocytosed NPs after 15 and 60 minutes of incubation was similar for all three NP formulations, although NP-cRGD-2k samples displayed a much higher fluorescence level. These results clearly demonstrate, that regardless of the PEG spacer length, cRGD-modified polymeric NPs were internalized by the cells. Moreover, the increase in cell-associated fluorescence of NPs with a higher clustering tendency results from enhanced receptor-mediated uptake and is not assigned to non-specific binding of NP aggregates to the membrane.

Chapter 5: Ligand density and linker length are critical targeting factors

Furthermore, these observations support, that U87MG cells are capable of internalizing whole clusters of ligand-decorated NPs upon multivalent binding to $\alpha_v\beta_3$ receptors. Nevertheless, it should be noted that the *in vitro* results cannot ultimately be translated into an *in vivo* performance of targeted nanoscaled colloids as there are numerous factors influencing the targeting ability, such as the formation of a protein corona influencing the phagocytosis of NPs, physiological barriers on the route to the target tissue or enzymes that might have an impact on degradation [10,171,232].

4 Conclusion

In this study, the contribution of the ligand density and the PEG linker length on integrin binding kinetics and uptake efficiency of cRGD-decorated polymeric colloids was evaluated. Although a sufficiently high cRGD density was considered as a prerequisite for the integrin receptor-mediated endocytosis, uptake efficiency of NPs possessing a high functionalization degree was mainly dominated by the PEG linker length. Ligand-decorated NPs with short PEG2k linkers displayed a high propensity to form colloidal clusters allowing for cooperative binding to integrin receptors. Furthermore, the higher flexibility of longer PEG chains increased the chance of entangling and cloaking the ligand, thereby decreasing the number of ligand-receptor binding events on the cell membrane. Moreover, the overall entropic loss upon binding to receptor was reduced if ligands were conjugated to shorter PEG chains compared to medium and longer PEG linkers. All of these factors affected different thermodynamic driving forces which ultimately determine the receptor-mediated internalization kinetics into U87MG cells. As a result, it was shown that targeted colloids with short PEG2k chains were most efficient in targeting $\alpha_v\beta_3$ receptors *in vitro*, whereas NPs with medium PEG3.5k and long PEG5k linkers only displayed a moderate and low endocytosis rate, respectively.

On the basis of these results, it should be noted, that the precise control of the ligand density might not always be sufficient for optimization of targeted drug delivery systems and that the role of the linker length should be taken into serious consideration for the design of colloidal drug delivery formulations in order to maximize therapeutic efficacy and minimize undesired side effects.

**Development and characterization of
virus-mimetic heteromultivalent
nanoparticles with enhanced selectivity
towards mesangial cells**

Abstract

Viruses provide pioneering concepts of selective receptor targeting as they recognize and enter their host cells by sequential binding to different adhesion and entry receptors, which allows them to unequivocally identify their targets. Following this strategy, polymeric core/shell structured nanocarriers were designed that were surface decorated with two mesangial cell-specific targeting ligands, an $\alpha_v\beta_3$ integrin-specific peptide and an angiotensin II receptor (AT₁R) antagonist. Mesangial cells were chosen as model targets as they play a central role in the progressive loss of kidney function in diabetic nephropathy. The two targeting ligands were tethered to PEG linkers with different lengths to allow for sequential ligand presentation. The primary ligand (AT₁R blocker) was used for the first recognition of the target cell *via* binding to the AT₁R, whereas the secondary ligand (cRGD) was initially “invisible” for the cell and interacted with the secondary receptor ($\alpha_v\beta_3$ integrin) in a time-shifted manner, followed by endocytosis of the colloid. Laser scanning confocal microscopy and flow cytometry experiments confirmed that dual-targeted nanoparticles displayed synergistic targeting effects with enhanced selectivity towards mesangial cells as compared to nanoparticles decorated with a single type of targeting ligand. Thus, virus-inspired heteromultivalent nanoparticles offer a versatile platform for delivering therapeutic cargos to a target site with significantly improved specificity and targeting efficiency.

1 Introduction

Effective and specific targeting of nanoscaled drug delivery systems to the target site is of paramount importance for the development of new nanomedicines. One of the leading concepts to enhance selectivity towards the target tissue is surface decoration of NPs with distinct targeting-moieties. This conventional targeting strategy aims at improved multivalent binding to cells that overexpresses a certain kind of target receptor in a diseased state. This allows the immobilized receptor ligands on the colloidal surface to bind to several cognate target receptor molecules on the cell surface simultaneously. Multivalent binding to target cells has been well documented for a plethora of nanomaterials [58,233-235] and various receptors such as G protein-coupled receptors (GPCR) [236-238] or integrins[81,239].

However, it is often overlooked that there is not one receptor that is exclusively expressed on a single cell-type which limits the potential of single-targeted drug delivery systems due to binding to off-target tissues. Even though these off-target cells express lower levels of the molecular target, they might be earlier accessible for the colloid during its route through the organism. Recent approaches have tried to overcome these limitations and increase target cell selectivity through simultaneous presentation of two different types of ligand. This heteromultivalent strategy has been proven to significantly enhance specificity and targeting efficiency *in vitro* [93-97,240]. Nevertheless, this concept has not taken sufficiently into account that by involving multiple types of receptor ligands also the number of off-target sites *in vivo* is increased, since the circulating colloids will encounter more types of cell that express either of the receptors compared to the single-target approach.

Viruses are widely considered the pioneers of selective receptor targeting as they have evolved unique strategies of recognizing and invading their host cells [100-102]. Virus binding to the cell surface and cell entry is a complex multi-stage procedure that involves the consecutive binding of different receptor types. The initial recognition of the primary adhesion receptor is used to identify their targets and allows the virus to attach to the cell membrane, yet it does not trigger virus entry. Nonetheless the close vicinity to the cell surface enhances heteromultivalent binding events to entry receptors which then initiate cellular uptake of the virus by endocytosis or membrane fusion [103-105].

Chapter 6: Virus-mimetic heteromultivalent nanoparticles

Inspired by the sequential binding of viruses to two distinct types of target receptors, virus-mimetic heteromultivalent NPs were engineered carrying two different kinds of targeting ligands. Thereby, the primary ligand was intended for the initial target cell recognition, whereas the secondary ligand was used to confirm cell identity and affiliates receptor-mediated endocytosis. Playing a key role in maintaining the glomerular function [139,241] and being critically involved in progression of renal diseases, such as diabetic nephropathy (DN) [154], mesangial cells were used as model target cell line. Pathological changes of mesangial cells are among the earliest and most critical events found in DN which makes them a valuable therapeutic target [151].

In this study, polymeric core/shell structured nanoparticles (NPs) consisting of poly(lactic acid)-poly(ethylene glycol) (PLA-PEG) that were further core-stabilized with additional poly(lactic-co-glycolic acid) (PLGA) were used as targeting system. Thereby, amphiphilic PLA-PEG block copolymers were utilized to introduce different targeting moieties. The primary and secondary ligand were conjugated to PEG linkers with different lengths aiming at a time-shifted consecutive binding of two receptor types (AT_1 and $\alpha_v\beta_3$ receptor) expressed on mesangial cells.

The schematic illustration of the concept of sequential mesangial cell recognition and cell entry by dual-targeted heteromultivalent NPs is depicted in Figure 1.

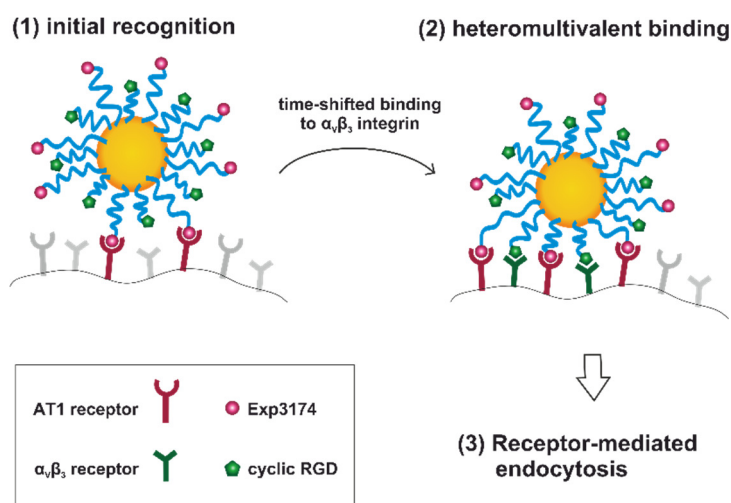


Figure 1. Schematic illustration of the concept of heteromultivalent target cell recognition by dual-targeted nanoparticles.

The primary ligand, an angiotensin receptor blocker (ARB; e.g. Exp3174) is used for the first recognition of the target cell *via* binding to the AT₁ receptor, but does not trigger endocytosis. Since the secondary ligand cyclo(Arg-Gly-Asp-D-Phe-Lys) (cRGD) is tethered to shorter PEG-chains, it is initially “invisible” for the cell and can only bind to the secondary receptor ($\alpha_v\beta_3$ integrin) if the NP is already in close proximity to the cell membrane. Binding to the secondary receptor will then trigger cellular uptake of the colloid.

To implement this targeting strategy, there are several requirements towards the two ligands that have to be met. The primary ligand should be able to specifically bind to the primary AT₁R with moderate affinity without inducing internalization. In contrast, the secondary receptor has to be shielded during the initial cell recognition to minimize ligand-receptor interactions with off-target cells. Furthermore, it has to be capable of binding to the secondary $\alpha_v\beta_3$ integrin receptor with high affinity and trigger endocytosis upon receptor binding.

In the first part of the study, two different ARBs (Exp3174 and Valsartan) were evaluated for their potential as primary ligand. Flow cytometry and confocal microscopy analyses were performed to assess AT₁R binding and cellular distribution of NPs, whereas a calcium immobilization assay was used to evaluate the affinity loss of ARB ligands upon PEGylation. In the second part of the study, $\alpha_v\beta_3$ integrin receptor binding and cellular uptake of NPs decorated with the secondary ligand was evaluated and the minimum PEG linker length required for ligand cloaking was assessed using $\alpha_v\beta_3$ integrin receptor overexpressing off-target cells (U87MG). In the last part of this study, binding and uptake of dual-targeted heteromultivalent NPs into mesangial cells was assessed and compared to the respective single-targeted counterparts.

2 Materials and methods

2.1 Materials

1,8-Diazabicyclo[5.4.0]undec-7-ene (DBU) solution, anhydrous dichloromethane (DCM), 4-(4,6-Dimethoxy-1,3,5-triazin-2-yl)-4-methylmorpholinium chloride (DMTMM), 3,6-Dimethyl-1,4-dioxane-2,5-dione (Lactide), CFTM 647 amine, anhydrous dimethyl sulfoxide (DMSO), fluoresceinamine isomer I (FAM), 2-Mercaptoethanol (BME), methoxy poly(ethylene glycol) with a molecular mass of 5000 g mol⁻¹

Chapter 6: Virus-mimetic heteromultivalent nanoparticles

(MeO-PEG5k), N-(3-Dimethylaminopropyl)-N'-ethylcarbodiimide (EDC), N-hydroxy-succinimide (NHS), N,N'-Dicyclohexylcarbodiimide (DCC), N,N-Diisopropylethylamine (DIPEA) and Resomer® RG 502 (PLGA) were received from Sigma-Aldrich (Taufkirchen, Germany). Losartan potassium and Valsartan were obtained from Santa Cruz (Heidelberg, Germany). Alexa Fluor™ 647 cadaverine, Dulbecco's phosphate buffered saline pH 7.4 (DPBS; containing 1.5 mM KH₂PO₄, 8 mM Na₂HPO₄, 2.7 mM KCl and 138 mM NaCl), fura-2AM and Leibovitz's L15 medium were obtained from Invitrogen GmbH (Karlsruhe, Germany). Cyclic RGDfK (cRGD) was purchased from SynPeptide Co. Ltd (Shanghai, China). Hydroxyl polyethylene glycol carboxylic acid with molecular masses of 2000, 3500 and 5000 g mol⁻¹ (COOH-PEG-OH) and hydroxyl poly(ethylene glycol) Boc-amine (Boc-NH-PEG5k-OH) with a molecular mass of 5000 g mol⁻¹ were provided by JenKem Technology USA Inc. (Allen, TX, USA). All other materials were of technical grade and obtained from Merck KGaA (Darmstadt, Germany). Ultrapure water was obtained using a Milli-Q water purification system (Millipore, Schwalbach, Germany).

2.2 Fluorescent labeling of PLGA

PLGA was dissolved in anhydrous DMF and the carboxylic acid group was activated by addition of DMTMM for two hours. Afterwards, 0.1 equivalents of CF™ 647 amine or Alexa Fluor™ 647 cadaverine, or 3 equivalents of FAM were added and stirred overnight to yield PLGA-CF647, PLGA-Alexa647 and PLGA-FAM. To remove unreacted dye, fluorescently labeled PLGA was purified by several precipitation steps in methanol (2x) and water (1x), followed by dialysis against water. The purified polymer conjugate was lyophilized for 72 h.

2.3 Synthesis of block copolymers

PLA-PEG-OMe (10k-b-5k), PLA-PEG-COOH (10k-b-5k, 10k-b-3.5k, 10k-b-2k) and PLA-PEG-NH₂ (10k-b-5k) block copolymers were synthesized by ring-opening polymerization as previously described by Qian *et al.* [170] with slight modifications. Prior to use, racemic 3,6-dimethyl-1,4-dioxane-2,5-dione (*D,L*-lactide) was purified by recrystallization from anhydrous ethyl acetate and dried under vacuum for at least 12 h. Linear MeO-PEG-OH or Boc-NH-PEG-OH with a molecular mass of 5000 g mol⁻¹ and COOH-PEG-OH with a molecular mass of either 2000, 3500 or 5000 g mol⁻¹ were used as macroinitiators for a ring-opening polymerization of cyclic *rac*-Lactide using

DBU as catalyst. After 1 h, the polymerization was quenched with benzoic acid. For cleavage of the Boc protection group of Boc-NH-PEG-PLA the respective polymer was dissolved in 50% (v/v) TFA in anhydrous DCM. After stirring for 30 minutes at room temperature, the solution was diluted with three volumes of anhydrous DCM and washed three times with saturated sodium bicarbonate solution and subsequently with ultrapure water. The organic phase was dried over anhydrous sodium sulfate, filtered, and concentrated under reduced pressure. For purification, block copolymers were precipitated in diethyl ether and dried under vacuum at either 35 °C (PLA-PEG-NH₂) or 45 °C (PLA-PEG-OMe, PLA-PEG-COOH). ¹H-NMR spectroscopy (CDCl₃, 300 Hz) was used to characterize the PLA-PEG polymers and calculate the molecular weight of the respective PLA block.

2.4 Synthesis of Losartan carboxylic acid (Exp3174)

Exp3174 (losartan carboxylic acid) was prepared from losartan by oxidation with potassium permanganate (KMnO₄). Briefly, losartan potassium was dissolved in 0.1 N sodium hydroxide (NaOH) solution and cooled down to 0 °C. KMnO₄ (2 equiv.) was dissolved in ultrapure water, added dropwise to the losartan solution and stirred for 4 h at room temperature. The reaction was monitored by thin layer chromatography (DCM/MeOH/HOAc 90/10/0.5). Losartan carboxylic acid was precipitated by stepwise addition of 1 N HCl until the supernatant turned pink. The precipitate, containing Exp3174 and manganese dioxide, was thoroughly washed with ultrapure water and the product was dissolved by addition of 2 N NaOH. Manganese dioxide was removed by centrifugation and subsequent filtration of the supernatant through a 5 µm Acrodisc® PES syringe filter (Pall GmbH, Dreieich, Germany). The pH of the filtered solution was adjusted to pH 3 using 1 N HCl to precipitate the product. The cloudy aqueous suspension was extracted three times with ethyl acetate. After ethyl acetate was removed by rotary evaporation, the residue was dissolved in ethanol and the solution was filtered through a 1.2 µm Acrodisc® PES syringe filter (Pall GmbH, Dreieich, Germany). The purified product was precipitated into 20 volumes of ultrapure water and lyophilized for 72 h.

2.5 Synthesis of PLA-PEG-ARB conjugates

The two AT₁ receptor blockers (ARB) Exp3174 and Valsartan were covalently conjugated to amine-modified PLA-PEG block copolymers and MeO-PEG5k-NH₂ by

Chapter 6: Virus-mimetic heteromultivalent nanoparticles

DCC/NHS chemistry. MeO-PEG5k-NH₂ was synthesized from its precursor MeO-PEG5k-OH using the Mitsunobu reaction as described previously [242]. First, ARBs were dissolved in DMF and the carboxylic group was activated by DCC and NHS for 1 hour at room temperature. Resulting urea byproducts were removed by centrifugation and subsequent filtration through a 0.45 μm Rotilabo® PTFE syringe filter (Carl Roth, Karlsruhe Germany). PLA_{10k}-PEG_{5k}-NH₂ and DIPEA were added and stirred for 24 h to form a stable amide bond. Ligand-modified conjugates were purified by precipitation in diethyl ether/-methanol, and dialysis against 10% (v/v) ethanol in 10 mM borate buffer (pH 8.5) to remove excess free ligand and reagents, followed by dialysis against ultrapure water to remove buffer salts. PLA-PEG-ARB conjugates were lyophilized for 72 hours. PEGylated ARBs were further purified and concentrated by ultrafiltration using Amicon Ultra-15 filter units (MWCO 3 kDa) and stored as solution until used. Ligand conjugation was confirmed using a fluorescamine assay [237].

The content of PEG was quantified using a colorimetric iodine complexation assay [192] (IA) and the conjugation efficiency (CE) for each ARB-conjugate was calculated using equation 1.

$$CE [\%] = \frac{c_{PEG} [\mu M] - c_{unreacted\ amines} [\mu M]}{c_{PEG} [\mu M]} \cdot 100 \quad (1)$$

In addition, liquid chromatography mass spectrometry* (LC-MS) was used to confirm absence of free ligand in PEGylated ARBs.

2.6 Synthesis of PLA-PEG-cRGD

Cyclo(RGDfK) was covalently conjugated to carboxy-modified PLA-PEG block copolymers *via* the lysine residue of the cyclic peptide. In brief, PLA-PEG-COOH was dissolved in anhydrous DMF and the carboxylic acid function was activated by EDC and NHS for 2 hours. Then, BME was added to quench the reaction. DIPEA and cRGDfK were subsequently added and stirred for 24 hours to form a stable amide bond [60]. Ligand-modified copolymers were purified by several precipitation steps in diethyl ether/-methanol mixtures, followed by dialysis against water for 24 hours to

*LC-MS analyses were performed by the Central Analytical Service (University of Regensburg)

remove excess free ligand and reactants. Conjugated cRGDfK was quantified using a 9,10-phenanthrenequinone assay as described previously [83]. A colorimetric iodine complexation assay [192] (IA) was used to quantify the exact amount of PEG. The conjugation efficiency (CE) was calculated as the ratio of peptide molecules to PEG chains (equation 2).

$$\text{CE [\%]} = \frac{c_{\text{cRGDfK}} [\mu\text{M}]}{c_{\text{PEG}} [\mu\text{M}]} \cdot 100 \quad (2)$$

2.7 Preparation of polymeric nanoparticles

For the manufacture of non-targeted nanoparticles (ntNPs) consisting of PLA_{10k}-PEG_{5k}-MeO and fluorescently labeled PLGA, polymers were diluted with acetonitrile to a final polymer concentration of 10 mg mL⁻¹. The copolymer mass ratio of PLA-PEG to PLGA was 70/30. The polymer mixture was then added dropwise into 10 volumes of borate buffer (10 mM, pH 8.5) while stirring. NP dispersions were stirred for 3 hours to evaporate the organic solvent. The dispersant was changed to DPBS *via* ultracentrifugation at 2500 g for 15 min using Pall Microsep® filters (MWCO 100 kDa). To prepare NPs with different ligand densities and varying PEG linker lengths, a fraction of PLA-PEG-MeO was substituted with ligand-modified PLA-PEG copolymers. The copolymer ratio of PLA-PEG to PLGA was continuously adjusted to obtain particles with consistent molarities of PLA-PEG and PLGA, resulting in a constant molar ratio of PEG chains per fluorescence tags.

2.8 Nanoparticle quantification by an iodine assay (IA)

Three batches of non-targeted NPs consisting of PLA_{10k}-PEG_{5k}-MeO and PLGA were prepared in ultrapure water, purified and concentrated as described above. A colorimetric iodine complexation assay was used to quantify the amount of PEG [192]. The exact polymer concentration was determined gravimetrically after lyophilization (n=3) of the concentrated NP samples and plotted against the PEG content determined by the iodine assay. Since the PEG content was considered to be constant, from this point on, the PEG content of freshly prepared samples was determined against the mPEG5k standard and used to calculate the polymer concentration of non-targeted NPs. For different formulations with varying ligand densities and PEG linker lengths, the PEG content was analyzed and diluted to attain equal molarities of PEG.

2.9 Flow cytometry analysis

Receptor binding of fluorescently labeled nanoparticles (PLGA-Alexa647, PLGA-CF647 or PLGA-FAM) was evaluated by flow cytometry. U87MG ($\alpha_v\beta_3^+$), NCI-H295R (AT_1^+) or rat mesangial cells (rMC; $\alpha_v\beta_3^+$ and AT_1^+) were seeded into 24-well plates (Corning, Corning, NY, USA) at a density of 120,000, 150,000 or 60,000 cells per well, respectively. For all experiments conducted with U87MG cells, wells were collagen-coated since binding of cRGDfK significantly impairs attachment of U87MG cells to uncoated wells [243]. Flow cytometry experiments were performed when 80 - 90% cell confluency was reached. Fluorescently labeled sample solutions were prepared in RGD binding buffer (20 mM TRIS, 150 mM NaCl, 2 mM $CaCl_2$, 1 mM $MgCl_2$, 1 mM $MnCl_2$, 0.1% BSA) supplemented with 10% FCS and incubated for 15 min at 37 °C to induce the formation of a protein corona. Cells were washed with DPBS and subsequently treated with NP dilutions for 45 min at 37 °C. After incubation, cells were washed with DPBS, trypsinized and centrifuged at 200 g for 5 min and washed once again with DPBS. Cells were suspended in 200 μ L DPBS and cellular fluorescence was analyzed with a FACSCalibur flow cytometer (Becton Dickinson, Franklin Lakes, USA). FAM and Alexa647/CF647 fluorescence was excited at 488 nm and 633 nm, respectively. Emission was measured using a 530/30 BP filter for PLGA-FAM and a 661/16 nm BP filter for PLGA-Alexa647/CF647. To evaluate the fluorescence intensity distribution 10,000 events were gated and results were corrected for the negative control (untreated cells) unless otherwise stated. Data were evaluated using the Flowing Software v2.5 (Turku, Finland).

2.10 Confocal Laser Scanning Microscopy (CLSM)

To analyze the NP binding pattern on the cells confocal microscopy was conducted. U87MG ($\alpha_v\beta_3^+$), NCI-H295R (AT_1^+) or rat mesangial cells ($\alpha_v\beta_3^+$ and AT_1^+) were seeded into 8-well μ -slides (Ibidi, Martinsried, Germany) at a density of 15,000 (U87MG; collagen-coated wells) or 8000 (rMC and NCI-H295R) cells per well, respectively. After cells had adhered to the cell culture plastic, NP binding was assessed. Fluorescently labeled sample solutions were prepared in TRIS binding buffer (20 mM TRIS, 150 mM NaCl, 2 mM $CaCl_2$, 1 mM $MgCl_2$, 1 mM $MnCl_2$, 0.1% BSA) supplemented with 10% FCS and incubated for 15 min at 37 °C to induce the formation of a protein corona. Cells were washed with DPBS and treated with pre-warmed NP test solutions for 45 min at 37 °C. After the incubation period, cells were vigorously washed with DPBS and cells

were analyzed in Leibovitz's medium. Confocal fluorescence analysis of cells was conducted on a Zeiss Axiovert 200 microscope combined with an LSM 510 laser-scanning device at 63-fold magnification. NP fluorescence was excited with an argon laser at 488 or 633 nm and the emission was recorded using a 530/30 nm bandpass (BP) or a 650 nm longpass filter for NPs labeled with PLGA-FAM or PLGA-Alexa647/-CF647, respectively.

2.11 Binding of ARB-decorated nanoparticles to AT₁R

Binding to the AT₁R expressed on NCI-H295R was assessed by flow cytometry and CLSM as described above. ARB-decorated NPs were manufactured by nanoprecipitation, using fluorescently labeled PLGA (FAM or Alexa647) and either PLA_{10k}-PEG_{5k}-Valsartan (NP-Val) or PLA_{10k}-PEG_{5k}-Exp3174 (NP-Exp). Non-targeted NPs served as control. NP concentration was 400 µg mL⁻¹ (FAM-labeled) for CLSM experiments and 300 µg mL⁻¹ (Alexa647-labeled) for flow cytometry analysis. To suppress specific NP-receptor interactions, cells were simultaneously incubated with NPs and an excess of the free ligand (500 µM).

The antagonistic affinity of native and conjugated ARB ligands towards the AT₁R was measured using the fluorescent fura-2 Ca²⁺ chelator method as recently described [54]. Briefly, suspensions of rat mesangial cells were incubated with 5 µM fura-2AM and 0.05% Pluronic F-127 in Leibovitz's L-15 medium for 1 hour at room temperature under light exclusion. After loading, cells were repeatedly washed by centrifugation (3x, 5 min, 200 g, RT) to remove excess fura-2AM and suspended in Leibovitz's medium. Dilutions of native ARB ligands (Exp3174, Valsartan) or ligands conjugated to mPEG5k (mPEG-Val, mPEG-Exp), as well as dilutions of ligand-decorated NPs (NP-Val, NP-Exp) were pipetted into half-area 96-well plates (Corning, Corning, NY, USA) at 10 µL per sample and 45 µL of cell suspension (2x10⁶ cells mL⁻¹) were subsequently injected into each well. After 30 minutes of incubation, 45 µL of the EC₈₀ of the agonist angiotensin II (Bachem, Bubendorf, Switzerland) was injected into each well and the fluorescence signal was instantly recorded using a FluoStar Omega fluorescence microplate reader (BMG Labtech, Ortenberg, Germany) for 30 s. The EC₈₀ (concentration that leads to 80% of the maximum response) of angiotensin II was determined from sigmoidal fit of the agonist dose-response curve in rat mesangial cells using GraphPad Prism 6.0 (GraphPad Software Inc., La Jolla, CA, USA). For time resolved ratiometric measurements 340/20 nm and 380/20 nm excitation filters were

Chapter 6: Virus-mimetic heteromultivalent nanoparticles

used and fluorescence emission recorded using a 510/20 bandpass filter. Loaded cells incubated with 0.1% Triton X-100 and 0.1% Triton X-100 supplemented with 45 mM ethylene glycol-bis(2-aminoethylether)-N,N,N',N'-tetraacetic acid (EGTA) were used to determine the maximum (R_{max}) and minimum (R_{min}) ratio, respectively. Intracellular calcium concentrations were calculated based on the Grynkiewicz equation [244]. IC_{50} values (concentration that leads to 50% inhibition) were determined with sigmoidal fitting (variable slope) of dose-response curves using GraphPad Prism 6.0 (GraphPad Software Inc., La Jolla, CA, USA).

2.12 Binding of cRGD-decorated nanoparticles to $\alpha_v\beta_3$ receptors

Binding of the secondary ligand (cRGD) to $\alpha_v\beta_3$ receptors as a function of ligand density was assessed by flow cytometry using U87MG cells. NPs with different ligand densities were prepared by varying the molar ratio of PLA_{10k}-PEG_{5k}-MeO to PLA_{10k}-PEG_{5k}-cRGD from 0/100 to 100/0, whereas the amount of PLGA-FAM was kept constant. U87MG cells were treated with NPs (200 $\mu\text{g mL}^{-1}$) for 45 min. An excess of cRGDfK (200 μM) was used to suppress binding to the $\alpha_v\beta_3$ receptor. To analyze the binding pattern of NP-cRGD on U87MG cells confocal microscopy was conducted.

2.13 Shielding of cRGD by tethering to shorter PEG chains

To initially shield the secondary ligand, NPs were prepared with 50/50 molar ratios of PLA_{10k}-PEG_x-cRGD ($x = 2\text{k}, 3.5\text{k}$ or 5k) and PLA_{10k}-PEG_{5k}-MeO. The copolymer ratio of PLA-PEG to PLGA was continuously adjusted to obtain particles with consistent molarities of PLA-PEG to PLGA, resulting in a constant molar ratio of PEG chains per fluorescence tags. NPs that were completely surface functionalized with cRGD conjugated to short PEG_{2k}, medium PEG_{3.5k} or long PEG_{5k}-linkers served as reference and ntNP were used as control. Cellular-associated fluorescence of U87MG cells treated with CF647-labeled NPs (200 $\mu\text{g mL}^{-1}$, or equivalents) for 45 min was quantified by flow cytometry.

2.14 Binding and uptake of heteromultiligand binding nanoparticles

Dual-targeted NPs decorated with both ligands (NP-Exp/cRGD_{3.5k}) were prepared using a 50/50 molar ratio of PLA_{10k}-PEG_{3.5k}-cRGD to PLA_{10k}-PEG_{5k}-Exp and a constant amount of PLGA-CF647. NPs comprising PLA_{10k}-PEG_{5k}-MeO and either

PLA_{10k}-PEG_{3.5k}-cRGD (NP-cRGD_{3.5k}/MeO) or PLA_{10k}-PEG_{5k}-Exp3174 (NP-Exp/MeO) blended at a mass ratio of 50/50, as well as ntNPs served as reference. Rat mesangial cells were seeded at a density of 40,000 cells per well and cultured for 48 h. Cells were incubated with 300 $\mu\text{g mL}^{-1}$ of CF647-labeled ntNPs (or NP equivalents) and receptor binding was investigated by flow cytometry and CLSM.

2.15 Statistical analysis

All results are presented as mean \pm standard deviation, based on the data obtained from at least $n = 3$ samples. Statistical significance was determined by means of one-way ANOVA, followed by Tukey's *post-hoc* test using GraphPad Prism 6.0 (GraphPad Software Inc., La Jolla, CA, USA). Statistical significances were set as indicated.

3 Results and discussion

3.1 Dual-targeted nanoparticles

For specific targeting of the AT₁R, designated as the primary target, PLA-PEG copolymers were modified with Exp3174 and Valsartan moieties. Both ligands belong to the group of angiotensin receptor blockers (ARBs) and are widely applied to treat diabetic nephropathy as they can lower the intraglomerular pressure and therefore, slow down disease progression [245]. The cyclic pentapeptide cRGDfK was used to target the vitronectin receptor that was intended as secondary target in this study. The $\alpha_v\beta_3$ integrin receptor can be found on epithelial and endothelial cells at low expression levels, whereas high receptor densities are linked to the development and progression of several diseases, such as cancer [246,247] or diabetic kidney disease [158,248].

As the targeting strategy aims at a time-shifted sequential binding of the primary (AT₁) and the secondary ($\alpha_v\beta_3$ integrin) receptor, ligand presentation had to be optimized. Therefore, cRGD was conjugated to PLA-PEG block copolymers with different PEG linker lengths (Figure 2). Pre-modification of block polymers allows for precisely tuning NP composition, which was considered as a prerequisite for the preparation of heteromultiligand NPs. Successful conjugation of PLA-PEG-cRGD copolymers was confirmed using a 9,10-Phenanthrenequinone assay, whereas conjugation efficiency of PLA-PEG-Exp3174 and PLA-PEG-Valsartan was determined using a fluorescamin

Chapter 6: Virus-mimetic heteromultivalent nanoparticles

assay. The conjugation efficiency was in the range of 97.9% to 99.7% for cRGD-modified block copolymers and between 98.4% and 99.0% for ARB-tethered PLA-PEG copolymer, respectively (Table 1).

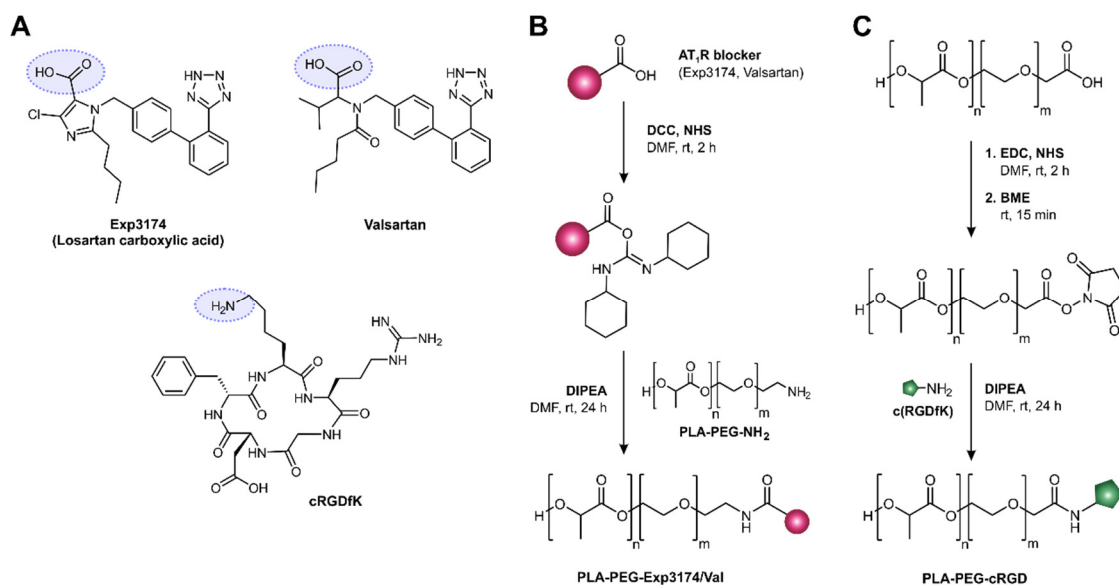


Figure 2. (A) Ligand moieties used in this study. (B) Angiotensin II receptor blockers (ARBs) Exp3174 and Valsartan were conjugated to amine-terminated PLA-PEG-NH₂ *via* the carboxylic acid function. (C) c(RGDfK) was tethered to carboxy-terminated PLA-PEG-COOH *via* the lysine residue.

Table 1. Conjugation efficiency of ligand-modified PLA-PEG copolymers.

PLA-PEG Copolymer	CE (%) ^[1]	PLA-PEG Copolymer	CE (%) ^[2]
PLA _{10k} -PEG _{2k} -cRGD	99.7 ± 3.9	PLA _{10k} -PEG _{5k} -Valsartan	98.4 ± 0.1
PLA _{10k} -PEG _{3.5k} -cRGD	98.8 ± 6.9	PLA _{10k} -PEG _{5k} -Exp3174	99.0 ± < 0.1
PLA _{10k} -PEG _{5k} -cRGD	97.9 ± 3.9		

⁽¹⁾ As determined by PCA.

⁽²⁾ As determined by Fluram Assay.

3.2 Targeting the AT₁R with ARB-decorated nanoparticles

A major prerequisite for the primary ligand is its ability to specifically bind to the AT₁R without initiating endocytosis of the nanocarrier. To evaluate the potential of Exp3174 and Valsartan as primary ligand, ARB-decorated NPs were prepared by nanoprecipitation and receptor binding was assessed by flow cytometry using NCI-H295R cells, an adrenal gland carcinoma cell line with high expression levels of the AT₁R [233]. Non-targeted NPs (ntNPs) served as control to evaluate nonspecific binding to the cells, whereas unmodified free ligand was added used to suppress specific NP-cell interactions. As shown in Figure 3A, cell-associated fluorescence was 1.59-fold and 2.35-fold increased, when NCI-H295R cells were incubated with Valsartan- and Exp3174-decorated NPs, respectively, compared to cells treated with ntNPs. In contrast, fluorescence of cells that were simultaneous incubated with ARB-modified NPs and excess free ligand was significantly decreased ($p < 0.001$) to a level comparable to the ntNP control, confirming that the interaction between targeted NPs and NCI-H295R cells was receptor-mediated. Confocal microscopy was used to evaluate the NP distribution pattern on NCI-H295R cells after incubation with NP samples. As shown in Figure 3B, both ARB-decorated NP formulations displayed strong binding to the cell membrane, whereas cellular association of non-targeted NPs was only marginal.

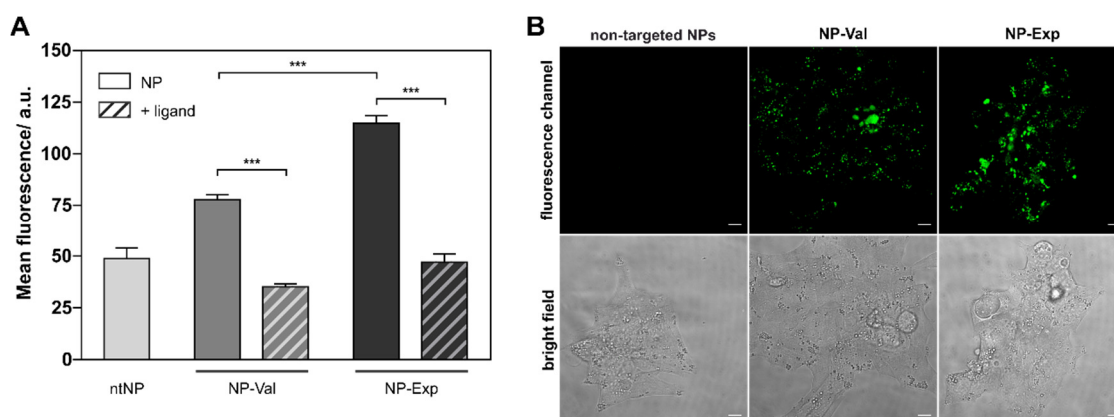


Figure 3. (A) Binding of Valsartan- and Exp3174-decorated NPs to AT₁R expressing NCI-H295R cells was quantified by flow cytometry. Levels of significance are indicated as: (***) $p < 0.001$ (B) The cellular distribution pattern of NCI-H295R cells incubated with ARB-decorated NPs was analyzed by CLSM. ARB-decorated NPs accumulated on the cell surface and were not internalized *via* endocytosis. Specific AT₁R binding could be suppressed by addition of excess free ligand (scale bar: 10 μm).

Chapter 6: Virus-mimetic heteromultivalent nanoparticles

Neither NP-Val nor NP-Exp were internalized by the cells, which is in good agreement with previous studies demonstrating that binding of AT₁R antagonists to the receptor do not trigger receptor-mediated endocytosis [249,250]. Targeted NPs were homogeneously distributed on the cell surface, however, the NP binding pattern was characterized by multiple bright fluorescent spots indicating distinct membrane areas with local AT₁R accumulation that allow for multivalent binding of ARB-decorated NPs.

Since Exp3174 and Valsartan are not immediately internalized by the cells, they stayed adhered to the cell membrane where they could bind to neighboring receptors. Although native Valsartan and Exp3174 have comparable receptor affinities, Exp3174-decorated NPs displayed stronger binding to the AT₁R expressing cells compared to NP-Val which might result from their different binding kinetics. Valsartan is a competitive antagonist, whereas Exp3174 is an insurmountable (noncompetitive) antagonist [251]. Insurmountable ARBs dissociate slowly from the receptor and have been reported not to dissociate under physiological conditions until the AT₁R is recycled. Due to the slow dissociation rate, antagonistic effects of insurmountable ligands cannot be overcome by high concentrations of angiotensin II [252]. Furthermore, slow dissociation favors multivalent binding of several receptors, because NPs stay in close proximity to the cell membrane over a prolonged period of time.

Hennig and colleagues [54] have previously demonstrated that PEGylation of AT₁R antagonists leads to severe affinity loss that can be significantly counterbalanced by the multivalent binding of Exp3174-decorated Qdots. For that reason, ARB-decorated NPs were evaluated for their binding affinities and compared to native and PEGylated counterparts using a calcium immobilization assay. Activation of AT₁R can be monitored by measuring the increase in cytosolic calcium using the fluorescent calcium chelator dye fura-2, whereas the angiotensin II induced receptor response is decreased after antagonist binding. Dose-response curves of native ARBs and their respective conjugates are depicted in Figure 4.

Native Valsartan and Exp3174 both blocked angiotensin II signaling of the AT₁R with low nanomolar affinity and IC₅₀ values of 2.4 ± 0.3 nM (Valsartan) and 0.7 ± 0.1 nM (Exp3174), which is in agreement with literature [233,253].

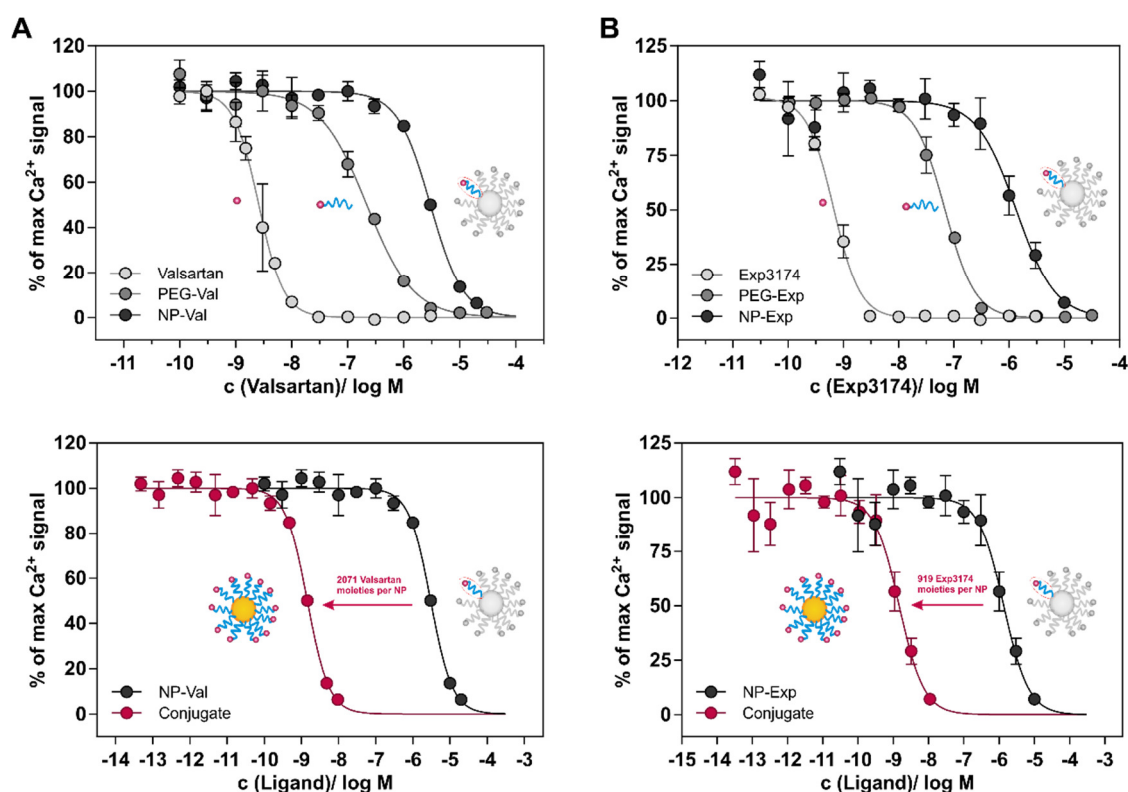


Figure 4. Affinity of (A) Valsartan and (B) Exp3174 towards AT_1R expressed on rat mesangial cells was assessed using an intracellular calcium immobilization assay. The native ligands antagonized the AT_1R with nanomolar affinity, whereas the receptor affinity was substantially decreased upon PEGylation and immobilization on polymeric NPs. When considering the whole NP as a targeting construct, the calculated affinity regained a nanomolar IC_{50} due to the high avidity of multivalent NPs.

To investigate the affinity of ARBs after PEGylation, Valsartan and Exp3174 were tethered to MeO-PEG5k- NH_2 with an equivalent molecular weight compared to the PEG5k linker used for ligand presentation on PLGA/PLA-PEG NPs. Compared to their native counterparts, the affinity of PEGylated Valsartan and Exp3174 was vastly decreased to $229.8 \pm 38.9 \text{ nM}$ and $66.3 \pm 8.4 \text{ nM}$, respectively (Table 2). Binding of ARBs to the AT_1R involves key acid-base interactions between acidic moieties of the ARB molecule and basic amino acid residues on the cognate receptor. Mire and colleagues have reported, that the carboxylic acid group at the 5-position of the imidazole ring provides a crucial hydrogen-bonding point of attachment to the AT_1R [254], which might be a contributing factor for the loss in affinity. However, Santella and colleagues have demonstrated that substitution of the carboxylic acid functional group at the

Chapter 6: Virus-mimetic heteromultivalent nanoparticles

imidazole 5-position with amides and esters only marginally decreases affinity towards the AT₁R but might have an impact on AT₁/AT₂ receptor selectivity [255]. Therefore, key factors for the substantial decrease in AT₁R affinity are the increased size and the steric hindrance of ARB-PEG conjugates. On the one hand, the binding site for small ARBs is located deep in the seven transmembrane regions of the AT₁R [237,256], it is hardly accessible for larger molecules. On the other hand, PEGylation attenuates intermolecular interactions between the ligand and the amino acid residues of the receptor, such as hydrogen bonding, hydrophobic and electrostatic interactions and π - π stacking, due to wrapping around the ARBs.

Table 2. Binding affinities of ARBs and ARB-conjugates towards AT₁R expressed on rMC.

Conjugate	# ARB ligands ⁽¹⁾	Ligand affinity/(nM)	Conjugate affinity ⁽²⁾ /(nM)
Valsartan	1	2.4 ± 0.3	n.a.
mPEG-Val	1	229.8 ± 38.9	229.8 ± 38.9
NP-Val	2071 ± 23	3022.1 ± 140.4	1.5 ± 0.1
Exp3174	1	0.7 ± 0.1	n.a.
mPEG-Exp	1	66.3 ± 8.4	66.3 ± 8.4
NP-Exp	919 ± 40	1515.9 ± 549.6	1.5 ± 0.8

⁽¹⁾ Conjugation of PEG-ARB was confirmed by MS.

⁽²⁾ Calculated based on the z-average size as determined by DLS and using a density of 1.2 g cm⁻³. (NP-Val: 47.9 ± 0.2 nm; NP-Exp3174: 36.5 ± 0.5 nm)

Compared to native ARBs, the calculated affinity of a single NP-bound PEG-Valsartan and PEG-Exp3174 was 1259- and 1516-fold increased to 3022.1 ± 140.4 nM and 1515.9 ± 549.6 nM, respectively. This additional loss in affinity can be attributed to the fact that the interface between the flat cell membrane and the NP, which has a considerable surface curvature, is rather small compared to the surface area of the respective NP. As a consequence, only a small fraction of ligands can spatially interact with their cognate receptors, whereas the remaining ligands cannot reach the target receptors located on the cell membrane due to the spherical NP geometry. However, these ligands contribute to the overall ligand density on the NP surface and thus also dictate the number of ligands that are present on the NP-cell interface. The IC₅₀ calculated for ARB-modified NPs was drastically decreased to 1.5 ± 0.1 nM (NP-Val) and 1.5 ± 0.8 nM (NP-Exp) compared to their monovalent PEGylated counterparts due

to the higher avidity of targeted NPs which enables simultaneous binding of multiple receptors on the target cell.

These results clearly demonstrate that both ARB ligands meet the requirements as primary ligand: a specific but moderate affinity towards the primary receptor and no induction of endocytosis upon receptor binding. However, Exp3174 was chosen for further experiments due to its slower binding kinetics that was considered highly beneficial for the sequential targeting approach.

3.3 Binding of cRGD-decorated nanoparticles to the $\alpha_v\beta_3$ receptor

NPs with different degrees of cRGD-modification (0 - 100%) were prepared and the influence of ligand density on binding to U87MG cells was investigated by flow cytometry. As shown in Figure 5A, a higher quantity of ligands on the particle surface led to an almost linear increase in cell-associated fluorescence, indicating an enhanced cellular association, while non-modified NPs displayed no receptor interaction at all (compared to the control cells).

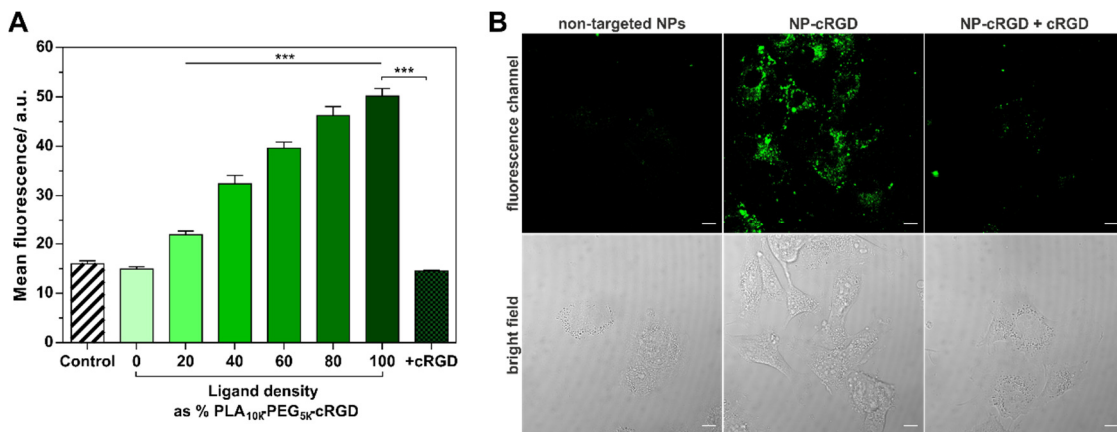


Figure 5: (A) Integrin binding of cRGD-decorated NPs as a function of ligand density quantified by flow cytometry. Specific integrin receptor binding could be suppressed with a surplus of free cyclo(RGD) peptide. Levels of significance are indicated as: (***) $p < 0.001$ compared to non-targeted NPs. (B) Endocytosis of NP-cRGD after binding to the $\alpha_v\beta_3$ receptor was confirmed by CLSM (scale bar: 10 μm).

Chapter 6: Virus-mimetic heteromultivalent nanoparticles

Binding of NPs with the highest degree of modification (100%) were completely suppressed when an excess of cRGDfK was added, which served as an evidence that binding of ligand-decorated NPs was receptor-mediated.

These data demonstrate, that even a low cRGD ligand density (e.g. of 20%) was sufficient to target the $\alpha_v\beta_3$ receptor. As confirmed by confocal microscopy, binding of cRGD-decorated NPs to the $\alpha_v\beta_3$ integrin receptor resulted in fast endocytosis of the nanocarrier (Figure 5B) and accumulation in vesicles within the cytosol. Simultaneous incubation of cells with NP samples and free ligand could efficiently inhibit specific NP uptake.

To avoid binding of the secondary ligand to off-target cells expressing high levels of $\alpha_v\beta_3$ integrin receptor, cRGD was conjugated to block copolymers with different PEG lengths and was additionally blended with equimolar amounts of methoxy-modified PLA_{10k}-PEG_{5k}-MeO. U87MG cells were chosen for this experiment, since they are known for their exceptionally high $\alpha_v\beta_3$ integrin expression [23] and thus, shielding has to be highly efficient to successfully avoid receptor binding and uptake by these off-target cells. As shown in Figure 6, receptor binding was effectively suppressed when the secondary ligand was tethered to short PEG2k or medium PEG3.5k linker, whereas the shielding was not efficient if cRGD was conjugated to long PEG5k.

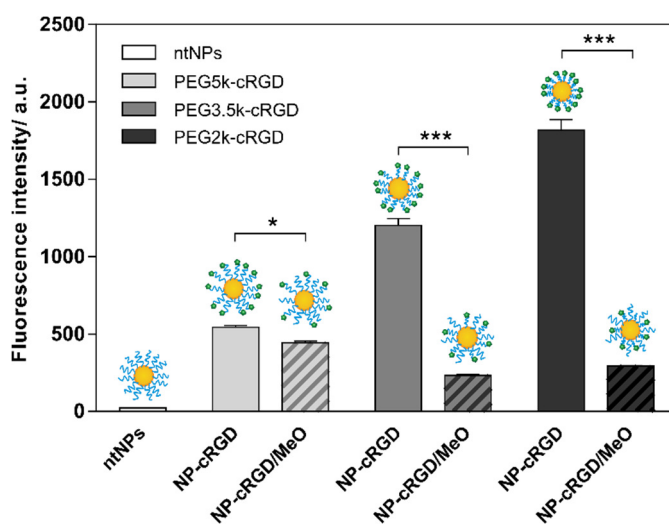


Figure 6: Shielding of the secondary ligand (cRGD) tethered to either 2k, 3.5k or 5k PEG was investigated by flow cytometry. NPs were either prepared from cRGD-modified PLA-PEG copolymers or blends of PLA-PEG-cRGD (2k, 3.5k or 5k PEG) and PLA-PEG5k-MeO. Levels of significance are indicated as: (*) $p < 0.05$, (***) $p < 0.001$.

Moreover, uptake of NP-cRGD without additional MeO-PEG-blends significantly increased by using shorter PEG chains. On the one hand combination of high cRGD densities and short PEG linkers result in an increasing tendency of targeted NPs to form agglomerates which enhances NP-receptor interactions *via* cooperative binding of NP clusters [226]. On the other hand, the molecular weight of PEG plays a pivotal role in the formation of a protein corona [214]. In the case of shorter PEG linker, the stealth effect in serum containing media is less pronounced and thus, interactions between ligands and receptors are enhanced.

In summary, polymeric NPs prepared with blends of PLA_{10k}-PEG_{5k}-MeO and PLA_{10k}-PEG_{3.5k}-cRGD were found as a good compromise between a sufficient stealth effect upon administration into the blood stream and an efficient shielding of the secondary ligand and were used for the final design of heteromultiligand-decorated NPs.

3.4 Synergistic targeting of mesangial cells with dual-targeted NPs

In a final experiment, dual-targeted heteromultivalent NPs (NP-Exp/cRGD_{3.5k}), comprising PLA_{10k}-PEG_{5k}-Exp, PLA_{10k}-PEG_{3.5k}-cRGD and fluorescently labeled PLGA were evaluated for their targeting efficiency towards rat mesangial cells in comparison to the two respective single-targeted NPs, modified with either the primary or the secondary ligand (NP-Exp/MeO and NP-cRGD_{3.5k}/MeO). Non-modified NPs (ntNPs) were used to determine the unspecific binding of polymeric NPs to target cells. Receptor binding and cellular uptake into mesangial cells were evaluated by flow cytometry and confocal microscopy, respectively. As shown in Figure 7, ntNPs displayed only minor association with rat mesangial cells which was attributed to unspecific binding to the cell membrane.

Receptor binding of NP-Exp/MeO (347.7 ± 3.2 a.u.), was 3.7-fold increased compared to the control particles (93.8 ± 1.6 a.u.), but NPs were exclusively located on the cell surface not internalized by the cells as confirmed by confocal microscopy. The shielding effect of NP-cRGD_{3.5k}/MeO towards $\alpha_v\beta_3$ integrin receptors was efficient and only a small fraction of the NP dose was internalized by mesangial cells. The fluorescence level of cells treated with a 50/50 mixture of single-targeted NP-Exp/MeO and shielded NP-cRGD_{3.5k}/MeO (227.7 ± 10.0 a.u.) was slightly higher than of NP-cRGD_{3.5k}/MeO (160.9 ± 11.3 a.u.). In contrast, NPs decorated with both, Exp3174 as

Chapter 6: Virus-mimetic heteromultivalent nanoparticles

a primary ligand (PEG5k) and cRGD as a secondary ligand (PEG3.5k), displayed an enhanced cellular binding (546.3 ± 25.1 a.u.) compared to particles prepared with only a single type of ligand (NP-Exp/MeO, NP-cRGD_{3.5k}/MeO).

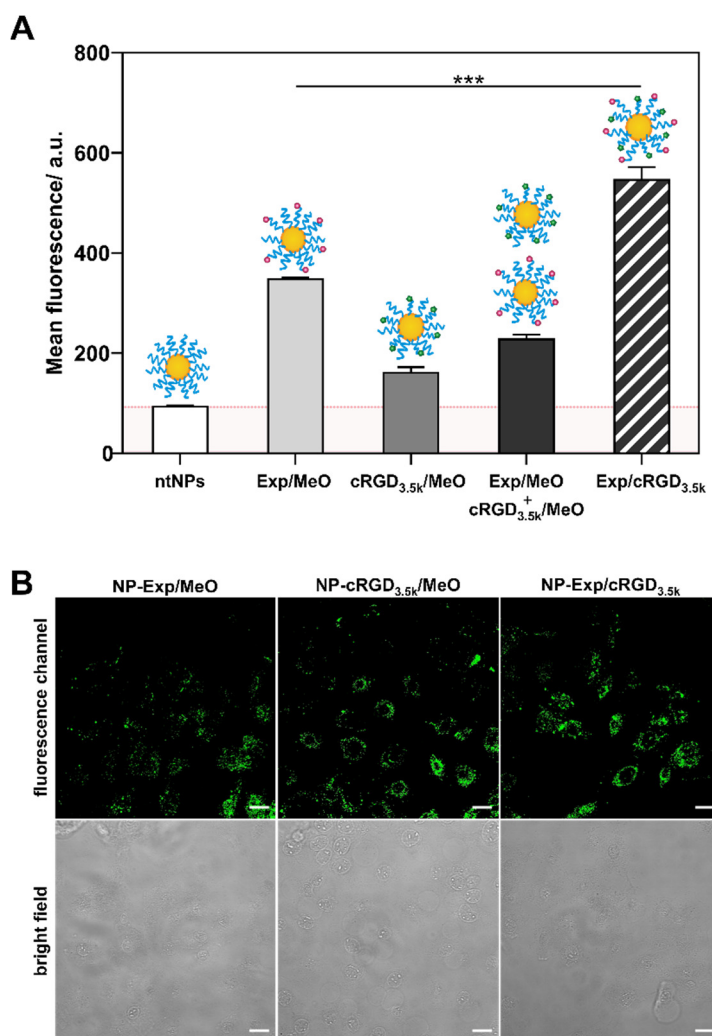


Figure 7. (A) Flow cytometry data for rat mesangial cells incubated with non-targeted NPs, single-targeted NPs, mixtures of both single-targeted NPs, or heteromultiligand binding NPs decorated with Exp3174 and cRGD. Non-targeted NPs and shielded cRGD-decorated NPs displayed only minor association to rat mesangial cells, whereas cellular associated fluorescence was 3.7- and 5.8-fold increased when cells were incubated with Exp3174-decorated and dual-targeted NPs, respectively. Levels of significance are indicated as: (***) $p < 0.001$ compared to non-targeted NPs. (B) Confocal microscopy confirmed, that cRGD-moieties were prerequisites for NP internalization. Exp3174-decorated NPs adhered to the cell surface, but were not internalized. To allow for comparison of all samples, the image contrast was adjusted and fluorescence (CF647) was displayed in false color (green) for better visibility. Scale bars indicate 20 μm .

The specific binding of dual-targeted NPs ($\Delta F = 452.5$ a.u.) as determined by subtracting the fluorescence levels determined for ntNPs was even 1.4-fold higher as the sum of NP-Exp/MeO and NP-cRGD_{3.5k}/MeO ($\Delta F = 321.0$ a.u.) and also enhanced by a factor of 1.7 compared to twice the value of the 50/50 mixture of NP-Exp/MeO and NP-cRGD_{3.5k}/MeO ($\Delta F = 267.8$ a.u.) corresponding to equal amounts of primary and secondary ligands. In addition, NP-Exp/cRGD_{3.5k} did not only display synergistic binding to mesangial cells but were also endocytosed, indicating that the secondary ligand was able to bind to the integrin receptor after the particle was in close proximity to the cell surface.

A summarized overview of the interaction of single- or dual-targeted NPs with mesangial cells is depicted in Figure 8. NPs solely decorated with the primary ligand (Exp3174) could bind to AT₁R on mesangial cells but were not internalized by endocytosis. NPs carrying only the secondary ligand (cRGD) tethered to shorter PEG3.5 linkers displayed poor receptor binding due to cloaking. In contrast, dual-targeted polymeric NPs featured with both receptor ligands were able to target the AT₁ and $\alpha_v\beta_3$ receptor in a time-shifted manner and were subsequently internalized by mesangial cells.

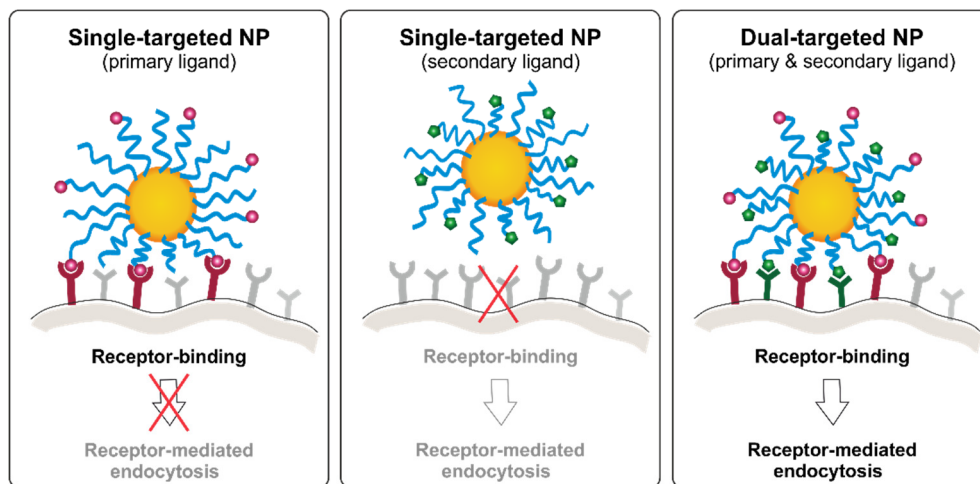


Figure 8. Summary of NP-cell interactions using single-targeted and heteromultivalent NPs.

Chapter 6: Virus-mimetic heteromultivalent nanoparticles

As the $\alpha_v\beta_3$ integrin is an ubiquitous receptor, expressed *inter alia* in endothelial and vascular smooth muscle cells [257], the delayed visibility of the secondary receptor ligand is mandatory to avoid an interaction and uptake by off-target cells exclusively expressing the secondary receptor. These findings clearly demonstrate that, compared to other heteromultivalent binding NPs developed in recent years [258], these polymeric NPs acted in a virus-like fashion with sequential binding to the primary (AT₁) and the secondary ($\alpha_v\beta_3$) receptor, which not only drastically enhanced specificity towards the target cell but also led to synergistic targeting efficiency compared to single-targeted NPs bearing only one of the two receptor ligands.

4 Conclusion

Dual-targeted polymeric NPs were able to target two different types of receptors (AT₁ and $\alpha_v\beta_3$ integrin) in a time-shifted manner. The primary ligand Exp3174, which was conjugated to longer PEG linkers (5 kDa), displayed specific and moderate affinity towards the AT₁R, but did not trigger internalization of the nanocarrier. The secondary ligand (cRGD), attached to shorter PEG linkers (3.5 kDa) with the intention to make the NP “visible” for the cell after a time delay efficiently bound to the $\alpha_v\beta_3$ integrin receptor and triggered endocytosis into the target cells. *In vitro* experiments confirmed, that this strategy not only improved targeting efficiency, but also specificity towards rat mesangial cells since NP bearing only the primary ligand were not endocytosed, whereas NPs bearing only the secondary ligand (cRGD) tethered to shorter PEG linkers displayed poor receptor binding due to cloaking.

In summary, heteromultiligand binding NPs can consecutively bind two types of receptor in a virus-like fashion and thus, possess high potential as advanced drug delivery systems.

**Gold-tagged polymeric nanoparticles with
spatially-controlled composition for
enhanced detectability in biological
environments**

Abstract

Nanoparticles made of organic materials offer the advantage of high biocompatibility for biomedical applications but suffer frequently from poor visibility in biological environments. Reliable and simultaneous qualitative and quantitative detectability in cells and tissues is a largely unmet need. While fluorescent labeling is convenient and allows for fast and extensive histological analysis, fluorescence imaging and quantitative analysis are limited by low resolution and significantly hindered by tissue auto-fluorescence. To overcome this restraint, 2.2 nm gold nanoparticles were introduced as a contrast agent at the interface between the hydrophobic fluorophore-loaded core and the hydrophilic shell of polymeric nanoparticles. Due to the spatially controlled stratified composition of polymer/gold hybrid nanoparticles, fluorescence quenching by gold was minimized to 15.1%, allowing for concomitant detection of both labels *via* confocal scanning fluorescence microscopy. Multilayered hybrid nanoparticles exhibited outstanding detectability in transmission electron microscopy without additional sample staining. Furthermore, they were capable of producing remarkable image contrast inside cells after gold or silver enhancement. The interfacial gold layer increased the hydrodynamic particle size only marginally from 71.8 to 89.5 nm and had no negative impact on biocompatibility *in vitro*. The gold content (0.75% m/m) is sufficiently high for future quantification in tissues after systemic administration. With their superior detectability and their unique properties, multilayered hybrid nanoparticles constitute an outstanding blue print and tool for the development of nanomedicines

1 Introduction

The detection of nanomaterials in biomedical applications is highly challenging. The use of organic materials for better biocompatibility results in poor detectability in cells and tissues. In histological sections polymeric colloids can *per se* not be localized with high resolution by transmission electron microscopy (TEM) or quantified in tissue after administration *in vivo* [259]. Because profound knowledge of pharmacokinetics and biodistribution [260] are key to the successful development of nanomedicines, additional labels are required to evaluate their *in vivo* performance and track their journey from the point of administration to the target site. Radioactive tags [261,262], organic fluorescent dyes [263,264] and inorganic “contrast” agents, such as nanocrystals [265,266] have frequently been used to facilitate the detection of organic nanoparticles (NPs). However, these labels suffer from significant limitations and drawbacks: Preparation, handling, and disposal of radioactive materials is expensive and requires strict safety precautions [267]. The incorporation of organic labels often results in significantly reduced drug loading capacity and unpredictable alteration of physicochemical properties [268]. Organic fluorescent tags are often quenched, degraded in a biological environment [269], or compromised in their detectability by the high auto-fluorescence of natural and fixed tissues [267].

Gold nanoparticles (AuNPs) constitute an ideal contrast agent because AuNPs possess excellent electron scattering properties [270] and are detectable *via* TEM, the method of choice to reveal a NP’s whereabouts in histological sections of cells and tissues [271]. In contrast to previous approaches [272], the use of small 2.2 nm gold tags would allow for labeling of polymeric NP without changing its structure or compromising the tag’s renal elimination after biodegradation of the labeled nanomaterial *in vivo* [21]. In histological samples, the size of gold tags could even be enlarged *via* silver or gold enhancement to increase visibility and permit detectability of hybrid NPs *via* optical microscopy [273,274]. Furthermore, AuNPs can be quantified by inductively coupled plasma optical emission spectroscopy (ICP-OES), which would allow for a quantitative evaluation of the labeled NP’s biodistribution [275]. However, random gold-tagging of fluorescently labeled nanomaterials can impede the concomitant detection of both labels because AuNPs are known to efficiently quench the emission of proximate fluorescent dyes, making the combination of a fluorescent label and a gold marker highly challenging [276]. In addition, most procedures to manufacture hybrid NPs lack

Chapter 7: Hybrid nanoparticles with enhanced detectability

the ability to control the NP composition precisely, such as gold content or surface ligand density, which constitute a major drawback of such hybrid materials.

To overcome these limitations, AuNPs were introduced at the interface between the lipophilic core and the hydrophilic shell of core/shell-type particles by covalently attaching them to a degradable lipophilic nanoparticle component. To this end, hydrophilic monoamine-functionalized small gold nanoparticles (AuNP-NH₂) were covalently conjugated to the carboxy-end of hydrophobic poly(lactic-*co*-glycolic acid) (PLGA) polymers. The gold-grafted polymers were then blended with amphiphilic poly(lactic acid)-poly(ethylene glycol) block copolymers (PLA-PEG), which are known for their ability to self-assemble into core/shell structured NPs and which served as a model for this study. Due to their hydrophilic nature, gold tags were expected to be located at the core/shell interface where they would be sufficiently distant from a fluorescent label in the core to minimize quenching effects.

In the first part of this studies, hybrid NPs were evaluated for their physicochemical properties and their cytotoxicity compared to nanoparticles consisting of unlabeled PLGA and PLA-PEG. In the second part, the dual detectability of particles labeled with gold and fluorescent tags in cells *via* TEM and confocal laser scanning microscopy was investigated. To enhance cellular uptake by $\alpha_v\beta_3$ integrin positive rat mesangial cells, hybrid NPs were additionally surface-decorated with cRGD ligands.

2 Materials and methods

2.1 Materials

1,4-Diazabicyclo[2.2.2]octane hydrochloride (DABCO), 1,8-Diazabicyclo[5.4.0]undec-7-ene (DBU) solution, anhydrous dichloromethane (DCM), 4-(4,6-Dimethoxy-1,3,5-triazin-2-yl)-4-methylmorpholinium chloride (DMTMM), 3,6-Dimethyl-1,4-dioxane-2,5-dione (Lactide), anhydrous dimethyl sulfoxide (DMSO), fluoresceinamine isomer I (FAM), 2-Mercaptoethanol (BME), methoxy poly(ethylene glycol) with a molecular mass of 5000 g mol⁻¹ (MeO-PEG5k-OH), N-(3-Dimethylaminopropyl)-N'-ethylcarbodiimide (EDC), N-hydroxy-succinimide (NHS), N,N-Diisopropylethylamine (DIPEA), Resomer® RG 502 (PLGA) and the Silver Enhancer Kit (SE-100) were received from Sigma-Aldrich (Taufkirchen, Germany). Cyclic RGDfK (cRGD) was purchased from SynPeptide Co. Ltd (Shanghai, China). Hydroxyl polyethylene

glycol carboxylic acid with a molecular mass of 5000 g mol⁻¹ (COOH-PEG5k-OH) was provided by JenKem Technology USA Inc. (Allen, TX, USA). GoldEnhance™ EM Plus was obtained from Nanoprobes Inc. (Yaphank, NY, USA). Monoamino gold nanoparticles (AuNP-NH₂) with an average size of 2.2 nm were purchased from Nanopartz (Loveland, CO, USA). All other materials were reagent grade and obtained from Merck KGaA (Darmstadt, Germany). Ultrapure water was freshly prepared using a Milli-Q water purification system (Millipore, Schwalbach, Germany).

2.2 Synthesis of gold-conjugated PLGA (PLGA-Au)

AuNP-NH₂ were lyophilized from an aqueous 3% (w/v) sucrose solution and reconstituted in anhydrous DMSO. PLGA was dissolved in anhydrous DCM and the terminal carboxylic acid group was converted to an NHS ester intermediate using 50 equivalents (equiv.) of EDC and 50 equiv. of NHS [60]. After two hours of stirring at ambient temperature, DCM was removed under reduced pressure, and the activated PLGA intermediate was dissolved in DMSO. DIPEA (10 equiv.) and the AuNP-NH₂ (0.015 equiv.) were added subsequently, and the polymer solution was stirred for 24 hours. PLGA-Au was precipitated into water, isolated by centrifugation, and lyophilized to yield a dark brown solid.

2.3 Fluorescent labeling of PLGA (PLGA-FAM)

PLGA was dissolved in anhydrous DMF and the carboxylic acid group was activated by addition of DMTMM (25 equiv.) for two hours. Afterwards, three-fold excess of FAM was added and stirred overnight to yield PLGA-FAM. Fluorescently labeled PLGA was purified by multiple precipitation steps in methanol (2x) and water (1x), followed by dialysis against water and subsequent lyophilization of the polymer conjugate.

2.4 Synthesis of PLA-PEG-OMe and PLA-PEG-COOH

PLA-PEG-OMe (10k-b-5k) and PLA-PEG-COOH (10k-b-5k) block copolymers were synthesized by a ring-opening polymerization as previously described in literature [170]. ¹H-NMR spectra were recorded in CDCl₃ at 295 K using a Bruker Avance 300 spectrometer (Bruker BioSpin GmbH, Rheinstetten, Germany).

2.5 Synthesis of PLA-PEG-cRGD

Cyclo(RGDfK) was covalently conjugated to carboxy-modified PLA-PEG block copolymers *via* the lysine residue of the cyclic peptide [60,80]. In brief, PLA-PEG-COOH was dissolved in anhydrous DMF and the carboxylic acid function was activated by EDC (25 equiv.) and NHS (25 equiv.) for 2 hours. Then, BME (30 equiv.) was added to quench the reaction. DIPEA (10 equiv.) and cRGDfK (3 equiv.) were subsequently added and stirred for 24 hours. The ligand-modified copolymer was purified by several precipitation steps in diethyl ether/-methanol mixtures, followed by dialysis against water for 24 hours to remove excess free ligand and reactants.

2.6 Preparation of polymeric nanoparticles

Polymeric NPs were prepared *via* bulk nanoprecipitation [165]. In general, PLA-PEG and PLGA were diluted with acetonitrile to a final polymer concentration of 10 mg mL⁻¹. The copolymer ratio of PLA-PEG to PLGA was kept constant at 60/40 (m/m). The polymer mixture was then added dropwise into 10 volumes of stirred DPBS. NP dispersions were stirred for 3 hours to remove the organic solvent and concentrated by centrifugation using 30 kDa molecular weight cut off Pall Microsep® Advance centrifugal filters (Pall, Dreieich, Germany).

2.7 Physicochemical Characterization

Spectral properties of hybrid NPs were analyzed on a FluoStar Omega fluorescence microplate reader (BMG Labtech, Ortenberg, Germany). Spectra were recorded between 400 and 800 nm. A solution of AuNP-NH₂ served as reference. Size and morphology of hybrid polymer/gold NPs were evaluated on a Zeiss Libra 120 electron microscope (Zeiss, Oberkochen, Germany). NP samples were applied onto carbon-coated nickel grids (300 mesh; Plano, Wetzlar, Germany) and incubated for 3 minutes. Excess sample solution was removed with a filter paper and sample grids were dried and stored in a desiccator before use. Dynamic light scattering (DLS) measurements of polymeric and hybrid NPs were performed with a Malvern Zetasizer Nano ZS (Malvern, Herrenberg, Germany) equipped with a 633 nm He-Ne laser and operating at an angle of 173° and a constant temperature of 25 °C using semi-micro PMMA disposable cuvettes (Brand, Wertheim, Germany). The position from the

cuvette wall was set to 4.65 mm and the attenuator was optimized by the device. Data were collected and analyzed using the Malvern Zetasizer software version 7.11 (Malvern Instruments, Worcestershire, United Kingdom).

2.8 Cytotoxicity

To assess the cytotoxicity of hybrid gold/polymer NPs compared to plain polymeric NPs, a metabolic assay using the reagent 3-(4,5-dimethylthiazol-2-yl)-2,5-diphenyltetrazolium bromide (MTT) was performed according to ISO 10993-5:2009 (Biological evaluation of medical devices, part 5: Tests for *in vitro* cytotoxicity). In brief, mouse fibroblast L-929 cells were seeded in 96-well plates at a density of 10,000 cells per well and allowed to adhere for 24 hours. NP formulations were prepared under aseptic conditions and treated with UV-light prior to the experiment to reduce the microbial burden. Samples with polymer concentrations ranging from 30 to 1000 $\mu\text{g mL}^{-1}$ were prepared in EMEM medium supplemented with 10% FCS and added to the cells. The gold content in hybrid colloids was not considered for quantification; hence, both NP formulations were adjusted to equal PEG molarities which were determined by an iodine complexation assay as described in literature [192]. SDS (0.1%) served as a positive control and pure medium as a negative control ($n = 6$). Cells were incubated with the test media for 24 h, 37 °C and 5% CO₂. Afterwards, sample solutions were gently aspirated and replaced by 50 μL of a solution containing 1.0 mg mL^{-1} MTT in EMEM medium. After 2 h of incubation, the MTT solution was removed and 100 μL isopropanol were added to each well. After 30 min of incubation under gentle shaking and light exclusion, absorbance at 570 and 690 nm was measured for each well using a FluoStar Omega fluorescence microplate reader (BMG Labtech, Ortenberg, Germany). The difference in absorbance at 570 and 690 nm was used to calculate the viability of cells. The viability of treated cells was normalized to the value of the control media samples. Microscope images were recorded with a Nikon SD-U1 camera (Nikon, Düsseldorf, Germany) connected to a Leica DM IRB microscope (Leica, Wetzlar, Germany).

2.9 Confocal laser scanning microscopy (CLSM)

To evaluate the enhanced detectability of hybrid NPs which were co-labeled with the gold tag and an additional fluorescent marker, uptake in rat mesangial cells was

Chapter 7: Hybrid nanoparticles with enhanced detectability

assessed by CLSM. For this experiment, cRGD-decorated hybrid NPs consisting of PLA-PEG-cRGD, PLGA-Au and PLGA-FAM at a ratio of 60/26.7/13.3 (m/m) were prepared *via* bulk nanoprecipitation into 10 mM borate buffer (pH 8.5) and the dispersant was changed to DPBS during the ultracentrifugation step. Rat mesangial cells were seeded into 8-well Nunc® Lab-Tek® Chamber Slide™ systems (Nunc, Inc., Naperville, IL) at a density of 15,000 cells per well. After overnight incubation to allow time for cell adhesion, cells were washed with PBS and treated with pre-warmed NP test solutions ($200 \mu\text{g mL}^{-1}$) for 45 min at 37 °C. To suppress specific NP-receptor interactions, cells were simultaneously incubated with NPs and excess free cRGD ($500 \mu\text{M}$). Untreated cells served as control. Then, cells were rinsed in DPBS, fixed with 2% paraformaldehyde in DPBS for 10 min, washed twice with DPBS, permeabilized with 0.1% Triton X-100 in DPBS for 10 min, and washed extensively with DPBS. The silver enhancement of gold tags was conducted according to the manufacturer's specification. In brief, cells were thoroughly rinsed in ultrapure water, covered with staining solution and incubated for 3 minutes at room temperature. Cells were subsequently washed with water, fixed with a 2.5% sodium thiosulfate solution for 2 min and washed with DPBS. Samples were embedded in Mowiol aqueous embedding medium supplemented with 2.5% (w/v) DABCO and analyzed with a Zeiss Axiovert 200 microscope combined with an LSM 510 laser-scanning device at 63-fold magnification. NP fluorescence was excited with an argon laser at 488 nm and the emission was recorded using a 530/30 nm bandpass (BP) filter. The brightfield channel was used to detect the NP-associated silver-enhanced gold tags.

2.10 Transmission electron microscopy to assess cellular uptake

For TEM experiments, rat mesangial cells were seeded into 24-well plates at a density of 70,000 cells per well and cultivated for 24 h. Peptide-decorated hybrid NPs were diluted with RGD binding buffer (20 mM TRIS, 150 mM NaCl, 2 mM CaCl₂, 1 mM MgCl₂, 1 mM MnCl₂, 0.1% BSA) supplemented with 10 % FCS and incubated for 15 min at 37 °C to induce the formation of a protein corona. The pre-warmed NP test solutions ($300 \mu\text{g mL}^{-1}$) were pipetted onto the cells and incubated for 45 min at 37 °C. Then, cells were washed, fixed with 2.5% paraformaldehyde and 2.5% glutaraldehyde in 0.1 M sodium cacodylate buffer for 2 hours at room temperature, and rinsed with cacodylate buffer. Samples were washed with a solution of 50 mM glycine in DPBS, rinsed with water, and permeabilized with 0.1% Triton X-100 in DPBS for 10 minutes. After

extensive washing steps with DPBS and water, samples were gold enhanced according to the manufacturer's specification. In brief, cells were thoroughly rinsed in ultrapure water, covered with staining solution and incubated for 6 minutes at room temperature. Cells were subsequently washed with water, fixed with a 2.5% sodium thiosulfate solution for 2 min and washed with DPBS. Postfixation was performed for 30 min in 0.5% osmium tetroxide at 4 °C. After several washing steps with 0.1 M cacodylate buffer, samples were dehydrated in a graded series of ethanol (50, 70, 80, 90, 99.5%). En-bloc staining with 2% uranyl acetate in ethanol 70% was performed after dehydration with 70% ethanol. Afterwards, samples were embedded in Epon. Ultrathin sections with a thickness of about 150 nm were imaged without further contrasting at 120 kV using a Zeiss Libra 120 electron microscope (Zeiss, Oberkochen, Germany).

2.11 Determination of gold content by ICP-OES

The gold content of the hybrid NPs was determined using ICP-OES. NP samples were prepared in ultrapure water, lyophilized, and weighed out. Samples were dissolved in freshly prepared *aqua regia* and diluted to 5 mL with ultrapure water. Polymer precipitates were removed by centrifugation at 5000 rpm for 10 min and subsequent filtration of the supernatant through a 0.45 µm PES filter. The Au³⁺ content of the solution was determined by ICP-OES analysis on a Spectro Flame-EOP (Analytical Instruments GmbH, Kleve, Germany). Gold(III) chloride solutions with concentrations of 1, 5, 10, 20 and 25 ppm were used for calibration.

2.12 Statistical analysis

All results are presented as mean ± standard deviation, based on the data obtained from at least $n = 3$ samples. Statistical significances between two groups were evaluated by Student's *t*-test using GraphPad Prism 6.0 (GraphPad Software Inc., La Jolla, CA, USA). Statistical significances were set as indicated.

3 Results and discussion

3.1 Synthesis of block copolymers and preparation of nanoparticles

Pre-modification of block copolymers with ligands, gold- or fluorescent tags enable the combination of different polymers during NP manufacturing and thus allow for precise control over gold content and NP composition. Figure 1A outlines the synthesis strategies of functionalized copolymers and conjugates. Hydrophilic AuNPs were covalently conjugated to hydrophobic PLGA by EDC/NHS chemistry [277]. In contrast to the highly water soluble AuNP-NH₂, the PLGA-Au conjugate was soluble in organic solvents (Figure S9).

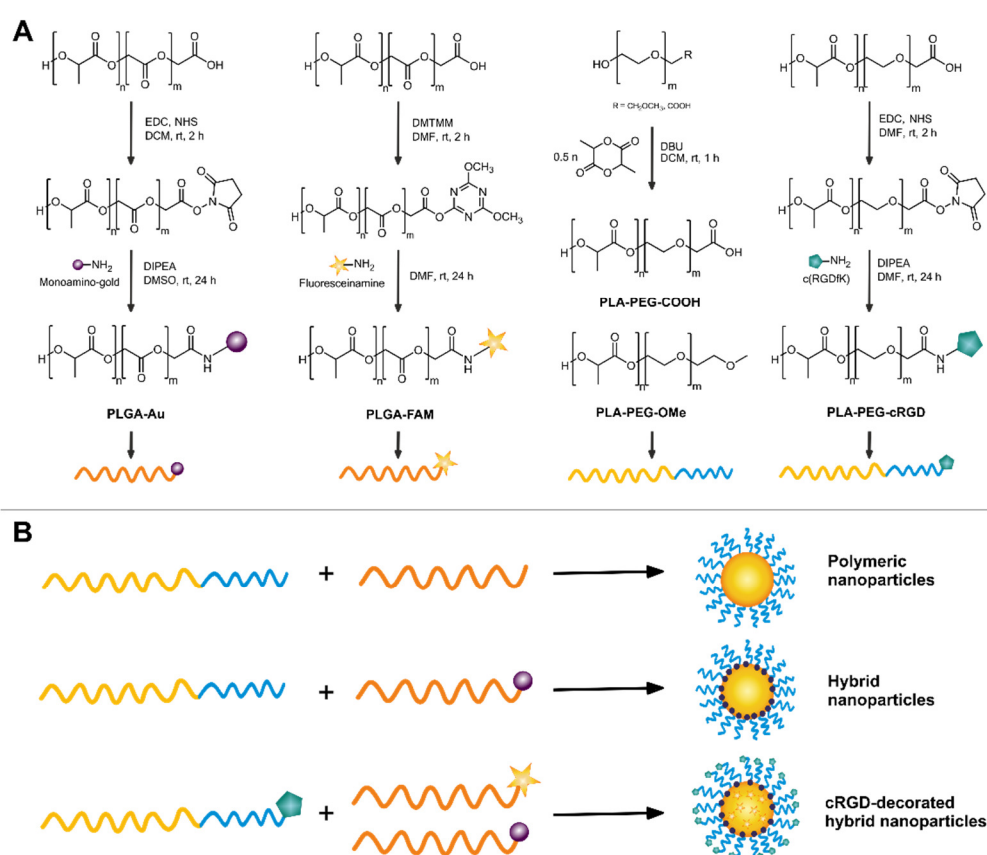


Figure 1. (A) Synthesis of PLGA-Au, PLGA-FAM, PLA-PEG-OMe and PLA-PEG-cRGD (B) Preparation of different NP formulations by mixing various functionalized PLGA and PLA-PEG block copolymers.

For the preparation of fluorescently labeled PLGA a novel conjugation strategy was applied, using DMTMM which is already established as highly efficient coupling reagent [278]. In contrast to EDC/NHS activation, addition of DIPEA is not necessary since the reaction proceeds independently of pH. PLA-PEG-OMe and PLA-PEG-COOH block copolymers were synthesized by a ring-opening polymerization according to literature [170], and the carboxylic acid function was further modified with a c(RGDfK) ligand. Complete conjugation was confirmed using a 9,10-phenanthrenequinone assay [83].

In this work, three different NP formulations were prepared, as depicted in Figure 1B. Plain polymeric and polymer/gold hybrid NPs were composed of PLA-PEG-OMe and PLGA terminated with either free carboxylic acid groups or conjugated gold tags, respectively. These two formulations were analyzed and compared regarding their physicochemical properties and cytotoxicity towards L-929 cells. In contrast, cRGD-decorated hybrid NPs also contained an additional fluorescence tag inside the particle core and were further decorated with an $\alpha_v\beta_3$ integrin binding ligand to enhance cellular uptake. This particular NP formulation was used to demonstrate the advanced detectability of gold/polymer hybrid NPs in optical and transmission electron microscopy.

3.2 Comparative characteristics of hybrid nanoparticles

In principle, the resulting block copolymer NPs display a core/shell structure, with a hydrophobic core consisting of PLGA and PLA and a hydrophilic PEG shell. In the case of the gold-tagged hybrid NPs, TEM images revealed a stratified composition with an additional gold layer at the core/shell interface (Figure 2A). Due to this gold layer, nanoscaled hybrid colloids were detectable in TEM even without further staining. As PEG is highly radiation sensitive, it depolymerizes and evaporates rapidly in the electron beam. As a result, the hydrophilic particle shell is not visible without further staining [279]. Because gold nanoparticles display discrete spectral properties depending on their size and shape, the absorbance spectra of gold (AuNP-NH₂) and hybrid NPs, which were assembled by nanoprecipitation of gold-tagged PLGA and PLA-PEG block copolymers, were recorded and evaluated regarding their absorbance maxima. AuNP-NH₂ exhibited localized surface plasmon resonance (LSPR) absorption with a maximum at approximately 505 nm. Nonetheless, the intensity of the LSPR absorption was quite low, which is characteristic of AuNPs with a size smaller than 3

Chapter 7: Hybrid nanoparticles with enhanced detectability

nm [280]. Compared to unconjugated 2.2 nm AuNPs, hybrid NPs displayed a slight red-shift of the absorbance maximum to 512 nm (Figure 2B). In the case of hybrid NPs, the small gold particles, which are embedded in the polymer matrix, are in close proximity to each other, pretending an aggregated state in the absorbance spectrum. Moreover, previous studies have reported that a red-shift of the LSPR band does not exclusively occur in case of aggregation, but also if the refractive index in the surrounding of the AuNP is increased [281].

In a further experiment, physicochemical characteristics of hybrid and polymeric NPs, consisting of plain PLGA and PLA-PEG copolymers, were determined. Dynamic light scattering was used to evaluate the impact of incorporated nanogold on size and size distribution of hybrid NPs.

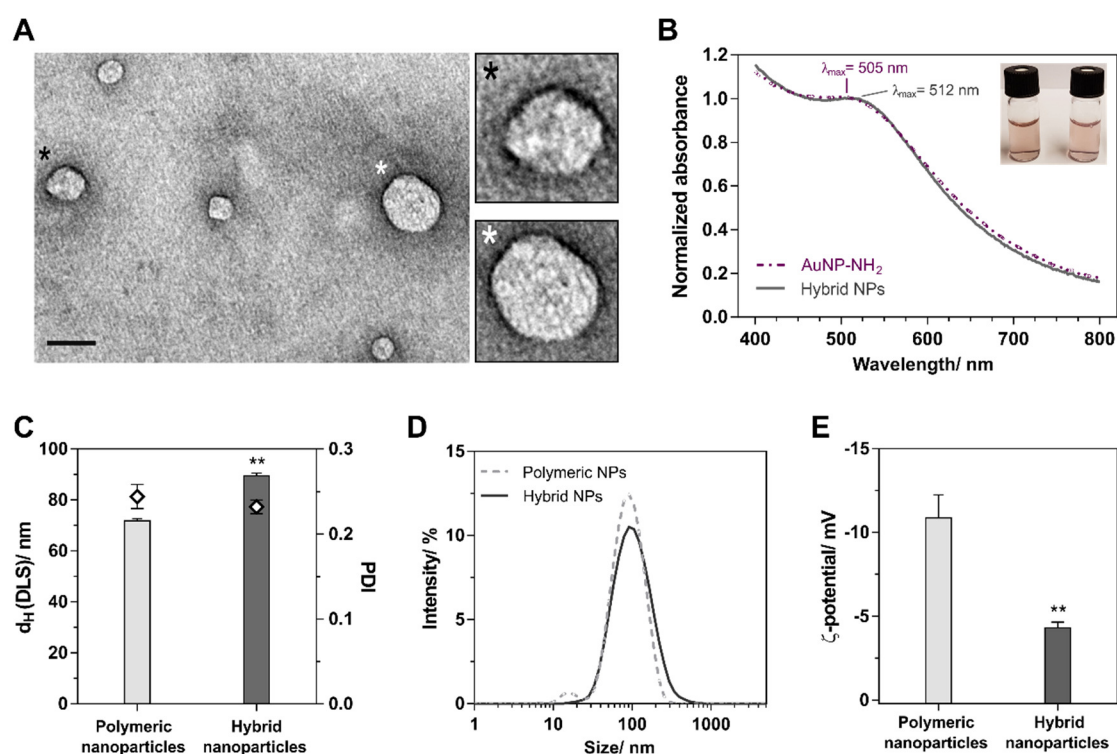


Figure 2. (A) Unstained TEM images of hybrid NPs revealed a stratified composition with an additional gold layer at the core/shell interface. Scale bar indicates 100 nm. Black and white asterisks indicate magnified picture sections. (B) Absorbance spectra of AuNP-NH₂ and hybrid NPs. Incorporation of AuNP-NH₂ into the polymer matrix led to a slight red-shift of LSPR absorbance which was also confirmed by the optical appearance. (C) Hydrodynamic diameter and PDI, (D) intensity-weighted size distribution and (E) ζ-potential of plain polymeric NPs and gold/polymer hybrid NPs. Levels of significance are indicated as: (**) $p < 0.01$, comparing polymeric NPs and hybrid NPs.

Compared to polymeric NPs, hybrid NPs displayed a moderate increase in hydrodynamic size from 71.8 to 89.5 nm and a slight decrease in PDI from 0.244 to 0.223 (Figure 2C). The average intensity-weighted size distribution of hybrid NPs was only slightly shifted towards larger particle sizes. In contrast to hybrid NPs, polymeric NPs showed an additional peak at around 10 to 20 nm, which could be attributed to a small fraction of polymeric micelles (Figure 2D). Although the increase in size could be explained by the introduction of an additional gold layer, it has to be considered that the hydrodynamic diameter, as measured by DLS, is also influenced by the particle charge and hydrophilicity of the surface which determines the extent of hydration. Nonetheless, these results indicate that the introduction of gold tags into the polymer matrix caused only minor changes in size and size distribution. Compared to polymeric NPs (-10.9 mV), hybrid NPs displayed less pronounced negative charge (-4.3 mV). This might be the result of amide bond formation *via* gold conjugation to the carboxylic acid groups of the PLGA polymer, leading to a less negatively-charged core of the polymeric particles (Figure 2E).

3.3 Cytotoxicity

Although, colloids consisting of biodegradable PLGA and PLA-PEG are considered biocompatible and safe for medical applications [282], insertion of gold tags can alter cytotoxicity of NPs. For instance, addition of the gold layer can influence particle integrity and thus, might trigger the release of amphiphilic polymer chains, which could then integrate into cell membranes and cause membrane damage and cell death [283,284]. To assess the cytotoxicity of the hybrid NPs in comparison to polymeric NPs, an MTT assay was performed in accordance with the ISO guideline 10993-5:2009. Neither polymeric nor gold/polymer hybrid NPs exhibited considerable cytotoxicity (Figure 3A) or changes in cell morphology (Figure 3B) over the tested range of concentrations. Viability of L-929 cells treated with NP dispersions was above 70%, which is the threshold of biocompatibility after a 24 h incubation period according to the ISO guideline.

As demonstrated in Figure 3, introduction of small 2.2 nm AuNPs into the colloidal system had no negative influence on cell viability (Figure 3A) or cell morphology (Figure 3B) at doses up to 1000 $\mu\text{g mL}^{-1}$. Due to covalent conjugation to the core polymers, gold particles are located at the core/shell interface. As a result, the gold tags are efficiently covered by the PEG chains, which impede direct contact between gold

Chapter 7: Hybrid nanoparticles with enhanced detectability

NPs and cell membranes and, furthermore, diminish nonspecific NP uptake. Although hybrid NPs can be considered non-toxic *in vitro*, the *in vivo* biocompatibility needs to be further assessed.

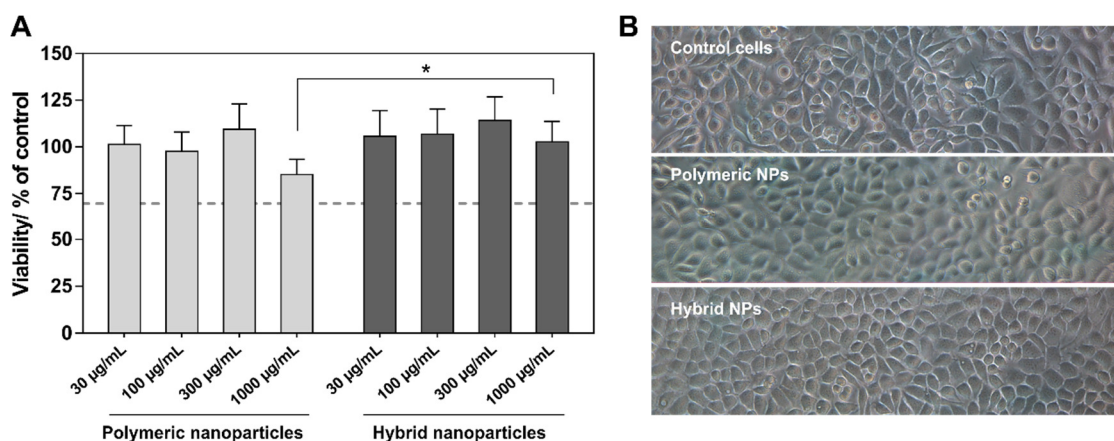


Figure 3. L-929 cell viability after 24 h incubation with polymeric and hybrid NPs. (A) Cell viability after treatment with different NP concentrations. The dotted line indicates cytotoxicity according to the ISO guideline. Levels of statistical significance are indicated as: (*) $p < 0.05$, comparing polymeric NPs with hybrid NPs at equal polymer concentrations. (B) Morphology of untreated control cells and L-929 cells incubated with either $1000 \mu\text{g mL}^{-1}$ of polymeric or hybrid NPs.

3.4 Simultaneous detection of fluorescence and gold tags in CLSM

To evaluate enhanced detectability in optical microscopy, fluoresceinamine-labeled cRGD-decorated hybrid NPs were used for an uptake study in rat mesangial cells. After incubation with sample solutions, cells were further treated with a silver enhancer kit to induce particle growth of the gold tags to a visible size. Cellular uptake was investigated and detected by recording the fluorescence image for detection of the fluorescein tag, the bright-field image for detection of the silver enhanced gold label, and merged images to evaluate colocation of both imaging tags. Compared to the control, cells incubated with cRGD-decorated hybrid NPs displayed efficient uptake of NPs, which accumulated in endosomes (Figure 4). Addition of excess free ligand resulted in complete suppression of NP-cell interaction, demonstrating that the fluorescence and gold/silver signal could be attributed to the specific integrin receptor-mediated uptake and did not derive from non-specific adhesion to the cellular

membrane. This receptor-mediated endocytosis pathway of cRGD-modified colloids has been reported in previous studies [217]. Interestingly, this NP uptake could be simultaneously detected by fluorescence and transmitted light microscopy. Furthermore, overlays of the fluorescence and the bright field channels demonstrated, that gold/silver precipitates were clearly colocalized with the fluorescence signals, indicating that the particles were still intact and that the gold/silver signals were not derived from nonspecific auto-nucleation of silver ions on the well surface. This observation was confirmed by the control cell sample, which was also treated with the silver enhancer and exhibited no auto-nucleation of the silver ions as well.

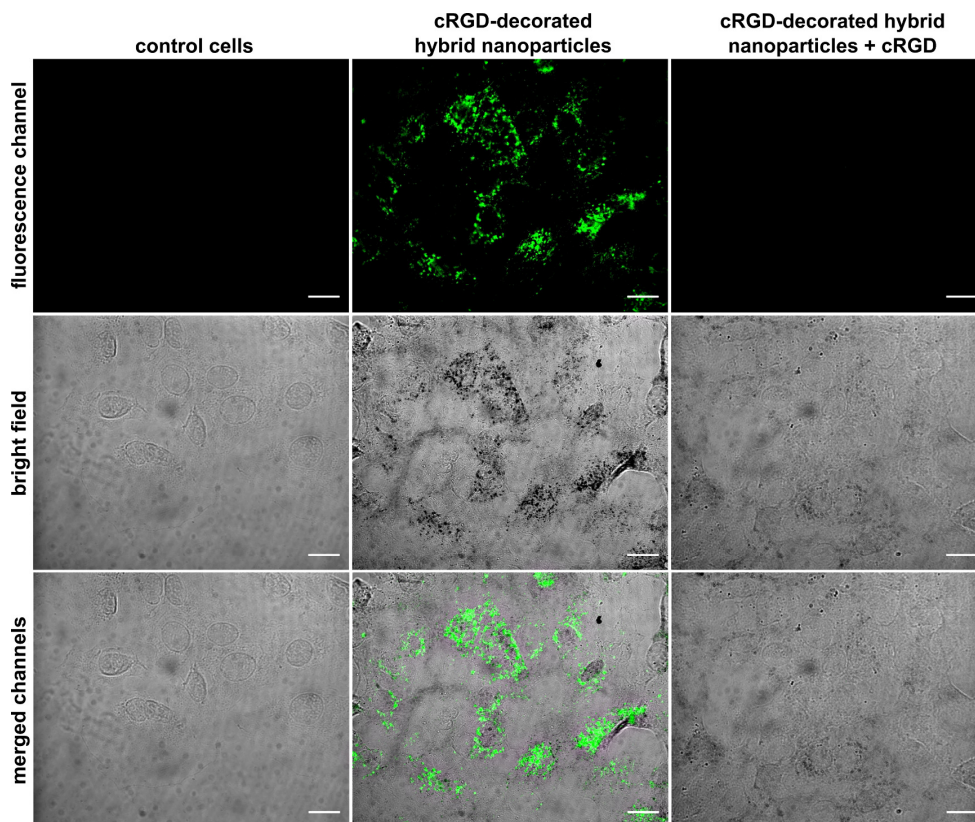


Figure 4. CLSM images of untreated control cells (left) and rat mesangial cells after incubation with cRGD-decorated hybrid NPs (middle). Excess free cRGD was used to suppress specific NP-receptor interaction (right). Cells were subsequently fixed, permeabilized and silver enhanced. Scale bars indicate 20 μm .

Chapter 7: Hybrid nanoparticles with enhanced detectability

These results are particularly interesting because previous studies have shown, that the combination of fluorescent dyes and AuNPs often results in strong quenching of fluorescence emission due to nonradiative energy transfer from the energy donor (e.g. a fluorescein derivative) to the gold particle, which acts as an energy acceptor [285-287]. In the case of AuNPs, two mechanisms for the energy transfer have been extensively discussed, fluorescence resonance energy transfer (FRET) and nanometal surface energy transfer (NSET). In both cases, the energy transfer is strongly distance dependent with d^{-6} and d^{-4} correlations, respectively, where d is the center-to-center distance between the fluorophore and the metal NP [288,289]. Since FRET requires a distinct LSPR band [290], it is the predominant process for samples containing gold particles larger than 5 nm, while NSET prevails for smaller NPs with a low intensity or even absence of the LSPR [280]. While AuNPs are located at the core/shell interface of the hybrid NPs due to their hydrophilic properties, fluorescein becomes more hydrophobic after grafting to the PLGA polymer and, as a result, is assumed to be localized in the particle core. Hence, most of the fluorophores inside the polymeric core are spared from quenching because the distance is too far for efficient energy transfer (Figure S10). Since the small AuNPs only exhibited weak LSPR absorbance, FRET will probably not occur. Emission spectra of hybrid NPs revealed that the maximum fluorescence intensity was reduced by only 15.1% upon introduction of AuNPs compared to fluorescein-labeled hybrid NPs with no gold tag (Figure S11).

This uptake experiment demonstrates the advanced detectability of hybrid NPs in optical microscopy, since fluorescence and enlarged AuNPs can be detected at the same time.

3.5 Enhanced detection of cRGD-decorated hybrid NPs in TEM

Gold particles have become an important tool for immunostaining of tissue sections because they display excellent contrast in TEM images due to their high electron density and allow for localization of cellular nanostructures by conjugating the gold tags to primary or secondary antibodies. Since TEM analysis provides a higher resolution compared to conventional fluorescence analysis, it is commonly used to investigate uptake of AuNPs into cells or biodistribution in tissues after systemic administration. In contrast, TEM visualization of polymeric NPs in tissue sections often requires a lot of effort and time, and is only feasible for NPs bearing a fluorescent tag

used for the photoconversion of a substrate to an electron-dense precipitate after embedding samples in epoxy and acrylic resins [291]. Therefore, cRGD-decorated hybrid NPs were utilized to evaluate the enhanced detectability in TEM (Figure 5). Uptake of cRGD-decorated hybrid NPs was again investigated using rat mesangial cells, followed by treatment with a gold enhancer kit. In contrast to the silver enhancement, particle growth of the gold enhancement proceeds in a slower and more controlled manner. Besides, the additional gold layer which is formed around the AuNP has a lower propensity to dissolve upon fixation and staining with osmium tetroxide compared to the silver enhanced counterparts [292]. Due to the gold enhancement, enlarged gold-tagged hybrid NPs were clearly visible even at lower magnifications and had a size in the range of 80 to 150 nm. For gold enhancement, samples were incubated for six minutes which was expected to increase the gold tags to a single particle size of approximately 5 nm.

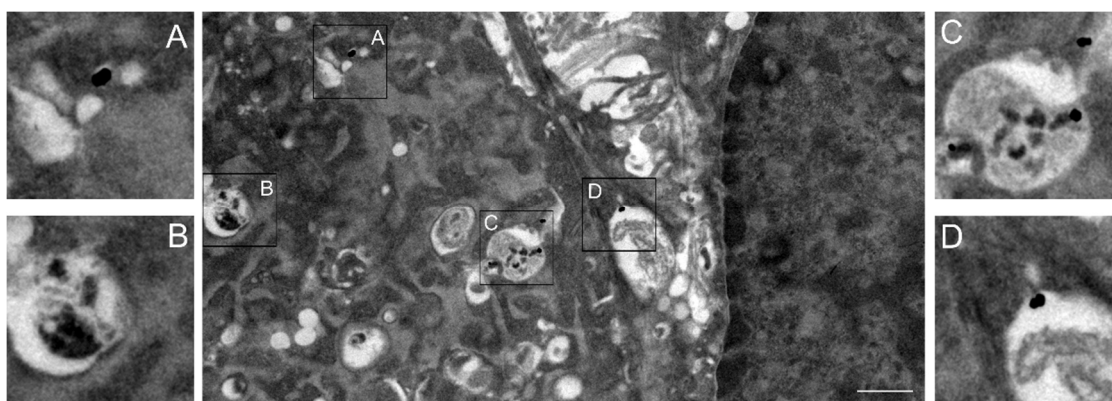


Figure 5. TEM images of rat mesangial cells treated with cRGD-decorated hybrid NPs and subsequent gold enhancement. Picture sections A-D show magnifications of gold-enhanced hybrid NPs within vesicles. Images were acquired at 6300-fold magnification. Scale bar indicates 1000 nm.

Since NPs are multi-tagged with numerous AuNPs at the core/shell interface, hybrid NPs are not only enlarged, but display excellent contrast in this biological setting. As depicted in Figure 5, cRGD-decorated hybrid NPs were internalized by the cells and accumulated in intracellular vesicles, which were homogeneously distributed in the cytoplasm. In contrast, untreated control cells did not form intracellular vesicles and showed no formation of gold deposits caused by nonspecific auto-nucleation of the gold enhancement (Figure S12).

3.6 Quantification of gold content by ICP-OES

ICP-OES was used to quantify the gold content of both NP formulations that were used for *in vitro* studies. For hybrid NPs consisting of 40% (m/m) PLGA-Au, the gold content was $(0.75 \pm 0.01)\%$. For preparation of cRGD-decorated hybrid NPs, 13.3% (m/m) of PLGA-Au were substituted by PLGA-FAM, resulting in a lower gold content of $(0.50 \pm 0.01)\%$ (Table 1). A detailed list of single results and calculations of the gold content can be found in the supplemental information (Table S3). These results clearly demonstrate that the gold content can be adjusted using different amounts of PLGA-Au during NPs manufacturing. To further increase the gold content, a higher stoichiometric ratio of monoamine gold NPs to PLGA can be used in the conjugation reaction. Depending on the gold content, as well as the dose applied, hybrid NPs might even enable quantitative biodistribution analysis by inductively coupled plasma mass spectrometry (ICP-MS) after systemic administration. For instance, laser ablation inductively-coupled plasma mass spectrometry (LA-ICP-MS) has already been used to quantify the distribution of 2 nm monolayer-protected AuNPs in tissues after intravenous injection into mice. The total dose of injected gold was as low as 4000 ng per mouse and even small gold amounts of approximately 10 ng g^{-1} (i.e. 10 ppb) could be quantified in tissue sections [293].

Table 1: Gold content of hybrid NP formulations with different copolymer ratios measured by ICP-OES.

Formulation	Copolymers	Polymer Ratio (m/m)	Au content/ %
Hybrid NPs	PLA-PEG/PLGA-Au	60/40	0.75 ± 0.01
cRGD-decorated hybrid NPs	PLA-PEG-cRGD/ PLGA-Au/PLGA-FAM	60/26.7/13.3	0.50 ± 0.01

Since polymeric NPs are generally utilized at polymer quantities up to 5 mg for intravenous administration in mice [294], the dose of gold present in the hybrid NPs is considered high enough for this experimental design. Henceforth, it would be of great interest to evaluate the *in vivo* biodistribution of hybrid NPs after systemic administration in the future.

4 Conclusion

In this study a multifunctional self-assembling nanocarrier system was developed in which targeting ligands and fluorescently labeled polymers can be combined with an additional gold tag. Introduction of small gold nanoparticles had only minor impact on particle size and no effect on the biocompatibility compared to plain polymeric NPs. Hybrid NPs exhibited only a weak LSPR, allowing combination with an additional fluorescent tag and the concomitant detection of both labels by optical microscopy. Furthermore, targeted hybrid NPs could be localized and detected after receptor-mediated internalization in cells by transmission electron microscopy after enlargement of gold tags *via* gold enhancement. The gold content incorporated into hybrid NPs was high enough to enable future quantification in tissue after systemic administration, e.g. *via* (LA)-ICP-MS. Pre-modification of polymers with gold or fluorophores, as well as conjugation of targeting ligands enables precise control of physicochemical properties, such as size, PEG density, ligand modification, and the content of gold and fluorescent tags. With their superior detectability, hybrid gold/polymer NPs open up new paths of detection for polymeric colloids. Since they can be further loaded with hydrophobic drugs or surface-decorated with multiple types of ligands, hybrid NPs represent an outstanding nanocarrier system for biomedical applications which require both, tunable drug targeting abilities and excellent imaging properties.

Chapter 8

Summary and Conclusion

Chapter 8: Summary and Conclusion

8.1 Summary

The use of conventional small-molecular drugs is often accompanied by undesired side effects derived from their intrinsic toxicity and their non-specificity. As introduced in **Chapter 1**, colloidal drug delivery systems have outstanding potential to deliver therapeutics more safely and more efficiently [9]. In particular, receptor-mediated targeting can be used to direct nanoparticles (NPs) to the site of disease and trigger their endocytosis [11]. This approach holds great promise to treat a variety of severe diseases. Among those, diseased kidneys are particularly promising targets since the renal filter integrity is often impaired in the diseased state. However, a myriad of parameters have to be taken into account when designing colloidal delivery systems for renal targeting [12]. This complexity explains why effective renal targeting remains an unmet medical need.

The targeting ability of NPs is largely determined by target-ligand interactions. However, the extent of interaction is governed by various particle attributes. Besides ligand density, NP size and shape are without doubt both essential key factors since they determine the interfacial contact area between a particle and its target site [65,212]. Therefore, manufacturing of NPs with uniform shape and size is mandatory to ensure successful and reliable targeting. To this end, microfluidic NP synthesis was evaluated and compared to the standard procedure in the field: bulk nanoprecipitation. It was found that nanoprecipitation generally results in formation of larger particles with a wide size distribution, whereas microfluidic synthesis allowed for the manufacturing of highly monodisperse NPs of defined size. Among the critical process parameters of microfluidic manufacturing, the flow rate ratio was identified to be the key determinant for tuning the size distribution, whereas particle size was mainly controlled by the total flow rate. In summary, it was demonstrated that the microfluidic synthesis of NPs is clearly superior to nanoprecipitation and has outstanding potential for the scalable preparation of NPs with reproducible attributes (**Chapter 3**).

While physicochemical characteristics certainly play a pivotal role for the NPs' performance as a delivery vehicle, their influence on the interactions with their environment *in vivo* should not be overlooked. For example, serum proteins are known to be deposited at the NP surface resulting in formation of a protein corona which has a major impact on the *in vivo* performance of colloidal drug delivery systems [29]. For instance, adsorption of opsonins on the colloidal surface substantially enhance NP sequestration by the reticuloendothelial system and can severely compromise colloidal

stability. Therefore, it is truly surprising how little is known about the influence of NP characteristics on the interaction with serum proteins. In order to gain a better understanding in this area, the impact of particle charge (negative, positive, zwitterionic) and hydrophobicity (non-charged) on the interaction with serum proteins was studied. Due to strong attractive electrostatic interactions, positively charged NPs formed the most distinct protein corona, followed by uncharged and negatively charged NPs, and finally zwitterionic NPs with the lowest amount of deposited protein. This enhanced interaction with serum proteins significantly impaired the colloidal integrity since the lipophilic cargo was continuously leached out of the hydrophobic NP core. In summary, these findings highlight the critical influence of protein-particle interactions on NP integrity and colloidal stability (**Chapter 4**).

Although there is a large number of studies available evaluating the therapeutic efficacy of targeted polymeric NPs, little is known about the critical attributes that can further influence their uptake into target cells. In literature, the degree of functionalization [59] is widely considered the main determinant for controlling uptake efficiency of targeted colloids while the linker length is often overlooked. In order to gain a deeper understanding of the combinational influence of both parameters the impact of varying cRGD ligand densities and poly(ethylene glycol) (PEG) spacer lengths on the specific receptor binding of core/shell structured polymeric NPs was investigated. When NPs with complete surface functionalization and short versus long linkers were compared, short PEG chains displayed a significantly higher tendency to form colloidal clusters which facilitated cooperative binding to integrin receptors on the cell membrane. In contrast, the use of longer and more flexible PEG chains enhanced the chance of ligand shrouding which significantly impeded ligand-receptor interactions. These results highlight the importance to consider the role of the linker length when designing targeted NPs (**Chapter 5**).

There are numerous examples where nature has inspired researchers to create high performance materials for medicine, engineering and other fields. For targeted delivery, viruses could serve as blueprints to optimize selective targeting of NPs. In order to mimic the binding sequence of viruses and utilize this selective targeting strategy for the treatment of renal diseases, polymeric core/shell structured nanocarriers were prepared and decorated with two mesangial cell-specific targeting ligands. In this system, the primary ligand (AT₁R blocker) was used for the first recognition of the target cell *via* binding to the AT₁R, whereas the secondary ligand

Chapter 8: Summary and Conclusion

(cRGD) was initially “invisible” for the cell and interacted with the secondary receptor ($\alpha_v\beta_3$ integrin) in a time-shifted manner, following endocytosis of the colloid. Laser scanning confocal microscopy and flow cytometry experiments confirmed that dual-targeted NPs displayed synergistic targeting effects with enhanced selectivity as compared to NPs decorated with a single type of targeting ligand. Consequently, such virus-inspired heteromultivalent NPs offer a versatile platform for delivering therapeutic cargos to a target site with significantly improved specificity and targeting efficiency (**Chapter 6**).

All previous chapters were focused on generating a better understanding for factors that can impact the performance of targeted NPs and use this knowledge to create optimized colloidal delivery systems. However, in order to proof a NP's efficacy *in vivo* its fate after intravenous injection has to be tracked precisely. In this context it should be mentioned that the simultaneous qualitative and quantitative detection of polymeric NPs in cells and tissues is a largely unmet need which is owed to their poor visibility in biological environments [259]. As this is a main factor which compromises the transition of polymeric NPs from preclinical research to clinical trials, NPs that can both be visualized with transmission electron microscopy and fluorescence imaging were developed. Small gold NPs were attached to poly(lactic-*co*-glycolic acid) (PLGA-Au) and introduced as a contrast agent into poly(lactic acid)-poly(ethylene glycol) (PLA- PEG) block-copolymer NPs. Due to their unique stratified composition with a hydrophobic PLA/PLGA core, a single gold layer at the core/shell interface and an outer PEG shell, these hybrid NPs exhibited outstanding detectability by transmission electron microscopy, even without the addition of contrast agents. Combination with an additional fluorescence label resulted in a negligible degree of fluorescence quenching which allowed for concomitant detection of the gold and the fluorescent label by optical microscopy. Moreover, the gold content of hybrid NPs is sufficiently high for the quantification in tissues after systemic administration. Due to their superior detectability and their unique properties, hybrid PLGA-Au/PLA-PEG NPs constitute an outstanding blueprint and tool for the development of nanomedicines (**Chapter 7**).

8.2 Conclusion

In this study, various novel concepts have been established that will facilitate the development of effective nanomedicines or improve existing delivery strategies. For example, the gained knowledge about protein corona formation should be applied to develop polymeric NPs with reduced serum protein deposition, which can circumvent impairment of the *in vivo* performance. Sequential binding of dual-targeted nanocarriers has been demonstrated to enhance targeting specificity and efficiency and therefore, can be of high value for the development of advanced drug delivery systems with significantly reduced systemic toxicity. Finally, gold/polymer hybrid NPs could serve as a powerful instrument to track polymeric NPs after administration and thereby contribute to gain a better understanding for their biodistribution. Future studies should be focused on applying these concepts in preclinical studies to assess their potential in animal models. In particular, drug loaded polymeric NPs with virus-mimetic binding should be employed in combination with a disease models of diabetic nephropathy to investigate their therapeutic potential.

References

1. Davis ME, Chen Z, Shin DM. Nanoparticle therapeutics: an emerging treatment modality for cancer. *Nat Rev Drug Discov.* 2008;7(9):771–82.
2. Kadam RS, Bourne DW, Kompella UB. Nano-advantage in enhanced drug delivery with biodegradable nanoparticles: contribution of reduced clearance. *Drug Metab Dispos.* 2012;40(7):1380–8.
3. Marcato PD, Durán N. New aspects of nanopharmaceutical delivery systems. *J Nanosci Nanotechnol.* 2008;8(5):2216–29.
4. Kang H, Mintri S, Menon AV, Lee HY, Choi HS, Kim J. Pharmacokinetics, pharmacodynamics and toxicology of theranostic nanoparticles. *Nanoscale.* 2015;7(45):18848–62.
5. Kalaydina RV, Bajwa K, Qorri B, Decarlo A, Szewczuk MR. Recent advances in „smart“ delivery systems for extended drug release in cancer therapy. *Int J Nanomed.* 2018;13:4727–45.
6. Wang J, Byrne JD, Napier ME, DeSimone JM. More effective nanomedicines through particle design. *Small.* 2011;7(14):1919–31.
7. Onoue S, Yamada S, Chan HK. Nanodrugs: pharmacokinetics and safety. *Int J Nanomed.* 2014;9:1025–37.
8. Liu L, Ye Q, Lu M, Lo YC, Hsu YH, Wei MC, *et al.* A New Approach to Reduce Toxicities and to Improve Bioavailabilities of Platinum-Containing Anti-Cancer Nanodrugs. *Sci Rep.* 2015;5:10881.
9. Farokhzad OC, Langer R. Impact of Nanotechnology on Drug Delivery. *ACS Nano.* 2009;3(1):16–20.
10. Kamaly N, Yameen B, Wu J, Farokhzad OC. Degradable Controlled-Release Polymers and Polymeric Nanoparticles: Mechanisms of Controlling Drug Release. *Chem Rev.* 2016;116(4):2602–63.
11. Kamaly N, Xiao Z, Valencia PM, Radovic-Moreno AF, Farokhzad OC. Targeted polymeric therapeutic nanoparticles: design, development and clinical translation. *Chem Soc Rev.* 2012;41(7):2971–3010.

References

12. Kamaly N, He JC, Ausiello DA, Farokhzad OC. Nanomedicines for renal disease: current status and future applications. *Nat Rev Nephrol.* 2016;12(12):738–53.
13. Wang AZ, Langer R, Farokhzad OC. Nanoparticle Delivery of Cancer Drugs. *Annu Rev Med.* 2012;63(1):185–98.
14. Salmaso S, Caliceti P. Stealth properties to improve therapeutic efficacy of drug nanocarriers. *J Drug Deliv.* 2013;2013:374252.
15. Amoozgar Z, Yeo Y. Recent advances in stealth coating of nanoparticle drug delivery systems. *Wiley Interdiscip Rev Nanomed Nanobiotechnol.* 2012;4(2):219–33.
16. Babu A, Templeton AK, Munshi A, Ramesh R. Nanodrug Delivery Systems: A Promising Technology for Detection, Diagnosis, and Treatment of Cancer. *AAPS PharmSciTech.* 2014;15(3):709–21.
17. Friedman AD, Claypool SE, Liu R. The smart targeting of nanoparticles. *Curr Pharm Des.* 2013;19(35):6315–29.
18. Chen H, Chen Y, Yang H, Xu W, Zhang M, Ma Y, *et al.* A dual-targeting nanocarrier based on modified chitosan micelles for tumor imaging and therapy. *Polym Chem.* 2014;5(16):4734–46.
19. Wei Y, Quan L, Zhou C, Zhan Q. Factors relating to the biodistribution & clearance of nanoparticles & their effects on in vivo application. *Nanomedicine (Lond).* 2018;13(12):1495–512.
20. Almeida JP, Chen AL, Foster A, Drezek R. In vivo biodistribution of nanoparticles. *Nanomedicine (Lond).* 2011;6(5):815–35.
21. Liu J, Yu M, Zhou C, Zheng J. Renal clearable inorganic nanoparticles: a new frontier of bionanotechnology. *Mater Today.* 2013;16(12):477–86.
22. Zuckerman JE, Davis ME. Targeting Therapeutics to the Glomerulus With Nanoparticles. *Adv Chronic Kidney Dis.* 2013;20(6):500–7.
23. Choi HS, Liu W, Misra P, Tanaka E, Zimmer JP, Itty Ipe B, *et al.* Renal clearance of quantum dots. *Nat Biotechnol.* 2007;25(10):1165–70.
24. Longmire M, Choyke PL, Kobayashi H. Clearance properties of nano-sized particles and molecules as imaging agents: considerations and caveats. *Nanomedicine (Lond).* 2008;3(5):703–17.

25. Alexis F, Pridgen E, Molnar LK, Farokhzad OC. Factors Affecting the Clearance and Biodistribution of Polymeric Nanoparticles. *Mol Pharm*. 2008;5(4):505–15.
26. Chrastina A, Massey KA, Schnitzer JE. Overcoming in vivo barriers to targeted nanodelivery. *Wiley Interdiscip Rev Nanomed Nanobiotechnol*. 2011;3(4):421–37.
27. Gustafson HH, Holt-Casper D, Grainger DW, Ghandehari H. Nanoparticle Uptake: The Phagocyte Problem. *Nano Today*. 2015;10(4):487–510.
28. Aggarwal P, Hall JB, McLeland CB, Dobrovolskaia MA, McNeil SE. Nanoparticle interaction with plasma proteins as it relates to particle biodistribution, biocompatibility and therapeutic efficacy. *Adv Drug Deliv Rev*. 2009;61(6):428–37.
29. Caracciolo G, Farokhzad OC, Mahmoudi M. Biological Identity of Nanoparticles : Clinical Implications of the Protein Corona. *Trends Biotechnol*. 2017;35(3):257–64.
30. Lundqvist M, Stigler J, Elia G, Lynch I, Cedervall T, Dawson KA. Nanoparticle size and surface properties determine the protein corona with possible implications for biological impacts. *Proc Natl Acad Sci U S A*. 2008;105(38):14265–70.
31. Cedervall T, Lynch I, Lindman S, Berggård T, Thulin E, Nilsson H, *et al*. Understanding the nanoparticle–protein corona using methods to quantify exchange rates and affinities of proteins for nanoparticles. *Proc Natl Acad Sci U S A*. 2007;104(7):2050–5.
32. Wurster EC, Liebl R, Michaelis S, Robelek R, Wastl DS, Giessibl FJ, *et al*. Oligolayer-Coated Nanoparticles: Impact of Surface Topography at the Nanobio Interface. *ACS Appl Mater Interfaces*. 2015;7(15):7891–900.
33. Hu Z, Zhang H, Zhang Y, Wu R, Zou H. Nanoparticle size matters in the formation of plasma protein coronas on Fe₃O₄ nanoparticles. *Colloids Surf B Biointerfaces*. 2014;121:354–61.
34. Lindman S, Lynch I, Thulin E, Nilsson H, Dawson KA, Linse S. Systematic investigation of the thermodynamics of HSA adsorption to N-iso-propylacrylamide/N-tert-butylacrylamide copolymer nanoparticles. Effects of particle size and hydrophobicity. *Nano Lett*. 2007;7(4):914–20.
35. Vonarbourg A, Passirani C, Saulnier P, Simard P, Leroux JC, Benoit JP. Evaluation of pegylated lipid nanocapsules versus complement system activation and macrophage uptake. *J Biomed Mater Res A*. 2006;78(3):620–8.

References

36. Fang J, Nakamura H, Maeda H. The EPR effect: Unique features of tumor blood vessels for drug delivery, factors involved, and limitations and augmentation of the effect. *Adv Drug Deliv Rev.* 2011;63(3):136–51.
37. Senger DR, Galli SJ, Dvorak AM, Perruzzi CA, Harvey VS, Dvorak HF. Tumor cells secrete a vascular permeability factor that promotes accumulation of ascites fluid. *Science.* 1983;219(4587):983–5.
38. Maeda H. The enhanced permeability and retention (EPR) effect in tumor vasculature: the key role of tumor-selective macromolecular drug targeting. *Adv Enzyme Regul.* 2001;41(1):189–207.
39. Yuan F, Leunig M, Huang SK, Berk DA, Papahadjopoulos D, Jain RK. Microvascular Permeability and Interstitial Penetration of Sterically Stabilized (Stealth) Liposomes in a Human Tumor Xenograft. *Cancer Res.* 1994;54(13):3352–6.
40. Carmeliet P, Jain RK. Angiogenesis in cancer and other diseases. *Nature.* 2000;407(6801):249–57.
41. Padera TP, Meijer EFJ, Munn LL. The Lymphatic System in Disease Processes and Cancer Progression. *Annu Rev Biomed Eng.* 2016;18:125–58.
42. Chow EK, Ho D. Cancer Nanomedicine: From Drug Delivery to Imaging. *Sci Transl Med.* 2013;5(216):216rv4.
43. Hatakeyama H, Akita H, Harashima H. A multifunctional envelope type nano device (MEND) for gene delivery to tumours based on the EPR effect: A strategy for overcoming the PEG dilemma. *Adv Drug Deliv Rev.* 2011;63(3):152–60.
44. Mishra S, Webster P, Davis M. PEGylation significantly affects cellular uptake and intracellular trafficking of non-viral gene delivery particles. *Eur J Cell Biol.* 2004;83(3):97–111.
45. Nakamura Y, Mochida A, Choyke PL, Kobayashi H. Nanodrug Delivery: Is the Enhanced Permeability and Retention Effect Sufficient for Curing Cancer? *Bioconjug Chem.* 2016;27(10):2225–38.
46. Nobs L, Buchegger F, Gurny R, Allemann E. Current methods for attaching targeting ligands to liposomes and nanoparticles. *J Pharm Sci.* 2004;93(8):1980–92.
47. Chou LY, Ming K, Chan WC. Strategies for the intracellular delivery of nanoparticles. *Chem Soc Rev.* 2011;40(1):233–45.

48. Xu S, Olenyuk BZ, Okamoto CT, Hamm-Alvarez SF. Targeting receptor-mediated endocytotic pathways with nanoparticles: rationale and advances. *Adv Drug Deliv Rev.* 2013;65(1):121–38.
49. Yameen B, Choi WI, Vilos C, Swami A, Shi J, Farokhzad OC. Insight into nanoparticle cellular uptake and intracellular targeting. *J Control Release.* 2014;190:485-99.
50. Montet X, Funovics M, Montet-Abou K, Weissleder R, Josephson L. Multivalent Effects of RGD Peptides Obtained by Nanoparticle Display. *J Med Chem.* 2006;49(20):6087–93.
51. Hong S, Leroueil PR, Majoros IJ, Orr BG, Baker JR Jr, Banaszak Holl MM. The Binding Avidity of a Nanoparticle-Based Multivalent Targeted Drug Delivery Platform. *Chem Biol.* 2007;14(1):107–15.
52. Shokeen M, Pressly ED, Hagooly A, Zheleznyak A, Ramos N, Fiamengo AL, *et al.* Evaluation of multivalent, functional polymeric nanoparticles for imaging applications. *ACS Nano.* 2011;5(2):738–47.
53. Tassa C, Duffner JL, Lewis TA, Weissleder R, Schreiber SL, Koehler AN, *et al.* Binding Affinity and Kinetic Analysis of Targeted Small Molecule-Modified Nanoparticles. *Bioconjug Chem.* 2010;21(1):14–9.
54. Hennig R, Pollinger K, Vesper A, Breunig M, Goepferich A. Nanoparticle multivalency counterbalances the ligand affinity loss upon PEGylation. *J Control Release.* 2014;194:20–7.
55. Fishburn CS. The Pharmacology of PEGylation: Balancing PD with PK to Generate Novel Therapeutics. *J Pharm Sci.* 2008;97(10):4167–83.
56. Laing BM, Guo P, Bergstrom DE. Optimized method for the synthesis and purification of adenosine--folic acid conjugates for use as transcription initiators in the preparation of modified RNA. *Methods.* 2011;54(2):260–6.
57. Martinez-Veracoechea FJ, Frenkel D. Designing super selectivity in multivalent nano-particle binding. *Proc Natl Acad Sci U S A.* 2011;108(27):10963–8.
58. Silpe JE, Sumit M, Thomas TP, Huang B, Kotlyar A, van Dongen MA, *et al.* Avidity Modulation of Folate-Targeted Multivalent Dendrimers for Evaluating Biophysical Models of Cancer Targeting Nanoparticles. *ACS Chem Biol.* 2013;8(9):2063–71.

References

59. Elias DR, Poloukhtine A, Popik V, Tsourkas A. Effect of ligand density, receptor density, and nanoparticle size on cell targeting. *Nanomedicine*. 2013;9(2):194–201.
60. Valencia PM, Hanewich-Hollatz MH, Gao W, Karim F, Langer R, Karnik R, *et al*. Effects of ligands with different water solubilities on self-assembly and properties of targeted nanoparticles. *Biomaterials*. 2011;32(26):6226–33.
61. Valencia PM, Pridgen EM, Rhee M, Langer R, Farokhzad OC, Karnik R. Microfluidic Platform for Combinatorial Synthesis and Optimization of Targeted Nanoparticles for Cancer Therapy. *ACS Nano*. 2013;7(12):10671–80.
62. Pereira Gomes C, Leiro V, Ferreira Lopes CD, Spencer AP, Pêgo AP. Fine tuning neuronal targeting of nanoparticles by adjusting the ligand grafting density and combining PEG spacers of different length. *Acta Biomater*. 2018;78:247–59.
63. Shewmake TA, Solis FJ, Gillies RJ, Caplan MR. Effects of Linker Length and Flexibility on Multivalent Targeting. *Biomacromolecules*. 2008;9(11):3057–64.
64. Gao H, Shi W, Freund LB. Mechanics of receptor-mediated endocytosis. *Proc Natl Acad Sci U S A*. 2005;102(27):9469–74.
65. Zhang S, Li J, Lykotrafitis G, Bao G, Suresh S. Size-Dependent Endocytosis of Nanoparticles. *Adv Mater*. 2009;21:419–24.
66. Yu B, Tai HC, Xue W, Lee LJ, Lee RJ. Receptor-targeted nanocarriers for therapeutic delivery to cancer. *Mol Membr Biol*. 2010;27(7):286–98.
67. Nobs L, Buchegger F, Gurny R, Allemann E. Biodegradable Nanoparticles for Direct or Two-Step Tumor Immunotargeting. *Bioconjug Chem*. 2006;17(1):139–45.
68. Nobs L, Buchegger F, Gurny R, Allemann E. Poly(lactic acid) nanoparticles labeled with biologically active Neutravidin™ for active targeting. *Eur J Pharm Biopharm*. 2004;58(3):483–90.
69. Weinberg WC, Frazier-Jessen MR, Wu WJ, Weir A, Hartsough M, Keegan P, *et al*. Development and regulation of monoclonal antibody products: Challenges and opportunities. *Cancer Metastasis Rev*. 2005;24(4):569–84.
70. Brennan FR, Shaw L, Wing MG, Robinson C. Preclinical safety testing of biotechnology-derived pharmaceuticals. *Mol Biotechnol*. 2004;27(1):59–74.

71. Kirpotin DB, Drummond DC, Shao Y, Shalaby MR, Hong K, Nielsen UB, *et al.* Antibody Targeting of Long-Circulating Lipidic Nanoparticles Does Not Increase Tumor Localization but Does Increase Internalization in Animal Models. *Cancer Res.* 2006;66(13):6732–40.
72. Peer D, Karp JM, Hong S, Farokhzad OC, Margalit R, Langer R. Nanocarriers as an emerging platform for cancer therapy. *Nat Nanotechnol.* 2007;2:751–60.
73. Acharya S, Dilnawaz F, Sahoo SK. Targeted epidermal growth factor receptor nanoparticle bioconjugates for breast cancer therapy. *Biomaterials.* 2009;30(29):5737–50.
74. Zhang Q, Reinhard BM. Ligand Density and Nanoparticle Clustering Cooperate in the Multivalent Amplification of Epidermal Growth Factor Receptor Activation. *ACS Nano.* 2018;12(10):10473–85.
75. Thomas TP, Shukla R, Kotlyar A, Liang B, Ye JY, Norris TB, *et al.* Dendrimer–Epidermal Growth Factor Conjugate Displays Superagonist Activity. *Biomacromolecules.* 2008;9(2):603–9.
76. Stern ST, McNeil SE. Nanotechnology Safety Concerns Revisited. *Toxicol Sci.* 2008;101(1):4–21.
77. Zhao N, Qin Y, Liu H, Cheng Z. Tumor-Targeting Peptides: Ligands for Molecular Imaging and Therapy. *Anticancer Agents Med Chem.* 2018;18(1):74–86.
78. Wang J, Masehi-Lano JJ, Chung EJ. Peptide and antibody ligands for renal targeting: nanomedicine strategies for kidney disease. *Biomater Sci.* 2017;5(8):1450–9.
79. Gu FX, Karnik R, Wang AZ, Alexis F, Levy-Nissenbaum E, Hong S, *et al.* Targeted nanoparticles for cancer therapy. *Nano Today.* 2007;2(3):14–21.
80. Diou O, Fattal E, Delplace V, Mackiewicz N, Nicolas J, Mériaux S, *et al.* RGD decoration of PEGylated polyester nanocapsules of perfluorooctyl bromide for tumor imaging: Influence of pre or post-functionalization on capsule morphology. *Eur J Pharm Biopharm.* 2014;87(1):170–7.
81. Hennig R, Kuespert S, Haunberger A, Goepferich AM, Fuchshofer R. Cyclic RGD peptides target human trabecular meshwork cells while ameliorating connective tissue growth factor-induced fibrosis. *J Drug Target.* 2016;24(10):952–9.

References

82. Guan X, Guan X, Tong H, Ma J, Sun X. Target Delivery of Daunorubicin to Glioblastoma by Cyclic RGD-Linked PEG-PLA Micelles. *J Macromol Sci, Part A*. 2015;52(5):401–6.
83. Graf N, Bielenberg DR, Kolishetti N, Muus C, Banyard J, Farokhzad OC, *et al.* $\alpha(V)\beta(3)$ integrin-targeted PLGA-PEG nanoparticles for enhanced anti-tumor efficacy of a Pt(IV) prodrug. *ACS Nano*. 2012;6(5):4530–9.
84. Reiser J, Gupta V, Kistler AD. Toward the development of podocyte-specific drugs. *Kidney Int*. 2010;77(8):662–8.
85. Pollinger K, Hennig R, Breunig M, Tessmar J, Ohlmann A, Tamm ER, *et al.* Kidney Podocytes as Specific Targets for cyclo(RGDfC)-Modified Nanoparticles. *Small*. 2012;8(21):3368–75.
86. Yan AC, Levy M. Aptamers and aptamer targeted delivery. *RNA Biol*. 2009;6(3):316–20.
87. Wu Z, Tang LJ, Zhang XB, Jiang JH, Tan W. Aptamer-Modified Nanodrug Delivery Systems. *ACS Nano*. 2011;5(10):7696–9.
88. Lakhin AV, Tarantul VZ, Gening LV. Aptamers: problems, solutions and prospects. *Acta Naturae*. 2013;5(4):34–43.
89. Stella B, Arpicco S, Peracchia MT, Desmaële D, Hoebcke J, Renoir M, *et al.* Design of Folic Acid-Conjugated Nanoparticles for Drug Targeting. *J Pharm Sci*. 2000;89(11):1452–64.
90. Xia W, Low PS. Folate-Targeted Therapies for Cancer. *J Med Chem*. 2010;53(19):6811–24.
91. Kohler N, Sun C, Wang J, Zhang M. Methotrexate-Modified Superparamagnetic Nanoparticles and Their Intracellular Uptake into Human Cancer Cells. *Langmuir*. 2005;21(19):8858–64.
92. Van Dongen MA, Rattan R, Silpe J, Dougherty C, Michmerhuizen NL, Van Winkle M, *et al.* Poly(amidoamine) Dendrimer–Methotrexate Conjugates: The Mechanism of Interaction with Folate Binding Protein. *Mol Pharm*. 2014;11(11):4049–58.
93. Saul JM, Annapragada AV, Bellamkonda RV. A dual-ligand approach for enhancing targeting selectivity of therapeutic nanocarriers. *J Control Release*. 2006;114(3):277–87.

94. Liu Y, Sun J, Cao W, Yang J, Lian H, Li X, *et al.* Dual targeting folate-conjugated hyaluronic acid polymeric micelles for paclitaxel delivery. *Int J Pharm.* 2011;421(1):160-9.
95. Levine RM, Kokkoli E. Dual-ligand $\alpha 5\beta 1$ and $\alpha 6\beta 4$ integrin targeting enhances gene delivery and selectivity to cancer cells. *J Control Release* 2017;251:24–36.
96. Laginha K, Mumbengegwi D, Allen T. Liposomes targeted via two different antibodies: Assay, B-cell binding and cytotoxicity. *Biochim Biophys Acta.* 2005;1711(1):25–32.
97. Kluza E, van der Schaft DWJ, Hautvast PAI, Mulder WJM, Mayo KH, Griffioen AW, *et al.* Synergistic Targeting of $\alpha v\beta 3$ Integrin and Galectin-1 with Heteromultivalent Paramagnetic Liposomes for Combined MR Imaging and Treatment of Angiogenesis. *Nano Lett.* 2010;10(1):52–8.
98. Kluza E, Jacobs I, Hectors SJ, Mayo KH, Griffioen AW, Strijkers GJ, *et al.* Dual-targeting of $\alpha v\beta 3$ and galectin-1 improves the specificity of paramagnetic/fluorescent liposomes to tumor endothelium in vivo. *J Control Release.* 2012;158(2):207–14.
99. Rangger C, Helbok A, Sosabowski J, Kremser C, Koehler G, Prassl R, *et al.* Tumor targeting and imaging with dual-peptide conjugated multifunctional liposomal nanoparticles. *Int J Nanomed.* 2013;8:4659–71.
100. García-Sastre A. Influenza Virus Receptor Specificity : Disease and Transmission. *Am J Pathol.* 2010;176(4):1584–5.
101. Grove J, Marsh M. The cell biology of receptor-mediated virus entry. *J Cell Biol.* 2011;195(7):1071–82.
102. Ploss A, Rice CM. Towards a small animal model for hepatitis C. *EMBO Rep.* 2009;10(11):1220–7.
103. Moradpour D, Penin F, Rice CM. Replication of hepatitis C virus. *Nat Rev Microbiol.* 2007;5:453–63.
104. Smith AE, Helenius A. How Viruses Enter Animal Cells. *Science.* 2004;304(5668):237–42.
105. Miao Z, Xie Z, Miao J, Ran J, Feng Y, Xia X. Regulated Entry of Hepatitis C Virus into Hepatocytes. *Viruses.* 2017;9(5):E100.

References

106. Bhella D. The role of cellular adhesion molecules in virus attachment and entry. *Philos Trans R Soc Lond B Biol Sci.* 2015;370(1661):20140035.
107. Edinger TO, Pohl MO, Stertz S. Entry of influenza A virus: host factors and antiviral targets. *J Gen Virol.* 2014;95(Pt 2):263–77.
108. Dou D, Revol R, Östbye H, Wang H, Daniels R. Influenza A Virus Cell Entry, Replication, Virion Assembly and Movement. *Front Immunol.* 2018;9:1581.
109. Ni R, Zhou J, Hossain N, Chau Y. Virus-inspired nucleic acid delivery system: Linking virus and viral mimicry. *Adv Drug Deliv Rev.* 2016;106(Pt A):3–26.
110. Xu H, Shaw DE. A Simple Model of Multivalent Adhesion and Its Application to Influenza Infection. *Biophys J.* 2016;110(1):218–33.
111. Hamilton BS, Whittaker GR, Daniel S. Influenza virus-mediated membrane fusion: determinants of hemagglutinin fusogenic activity and experimental approaches for assessing virus fusion. *Viruses.* 2012;4(7):1144–68.
112. Böttcher-Friebertshäuser E, Klenk HD, Garten W. Activation of influenza viruses by proteases from host cells and bacteria in the human airway epithelium. *Pathog Dis.* 2013;69(2):87–100.
113. Mei L, Fu L, Shi K, Zhang Q, Liu Y, Tang J, *et al.* Increased tumor targeted delivery using a multistage liposome system functionalized with RGD, TAT and cleavable PEG. *Int J Pharm.* 2014;468(1):26–38.
114. Sawant RM, Hurley JP, Salmaso S, Kale A, Tolcheva E, Levchenko TS, *et al.* “SMART” Drug Delivery Systems: Double-Targeted pH-Responsive Pharmaceutical Nanocarriers. *Bioconjug Chem.* 2006;17(4):943–9.
115. Doolittle E, Peiris PM, Doron G, Goldberg A, Tucci S, Rao S, *et al.* Spatiotemporal Targeting of a Dual-Ligand Nanoparticle to Cancer Metastasis. *ACS Nano.* 2015;9(8):8012–21.
116. Zhu L, Kate P, Torchilin VP. Matrix metalloprotease 2-responsive multifunctional liposomal nanocarrier for enhanced tumor targeting. *ACS Nano.* 2012;6(4):3491–8.
117. Romagnani P, Remuzzi G, Glassock R, Levin A, Jager KJ, Tonelli M, *et al.* Chronic kidney disease. *Nat Rev Dis Primers.* 2017;3:17088.

118. Whiting DR, Guariguata L, Weil C, Shaw J. IDF Diabetes Atlas: Global estimates of the prevalence of diabetes for 2011 and 2030. *Diabetes Res Clin Pract.* 2011;94(3):311-21.
119. Schena FP, Gesualdo L. Pathogenetic Mechanisms of Diabetic Nephropathy. *J Am Soc Nephrol.* 2005;16(Suppl 1):S30-3.
120. Ahmad J. Management of diabetic nephropathy: Recent progress and future perspective. *Diabetes Metab Syndr.* 2015;9(4):343-58.
121. Roshan B, Stanton RC. A story of microalbuminuria and diabetic nephropathy. *J Nephropathol.* 2013;2(4):234-40.
122. Scott RP, Quaggin SE. The cell biology of renal filtration. *J Cell Biol.* 2015;209(2):199-210.
123. Puelles VG, Hoy WE, Hughson MD, Diouf B, Douglas-Denton RN, Bertram JF. Glomerular number and size variability and risk for kidney disease. *Curr Opin Nephrol Hypertens.* 2011;20(1):7-15.
124. Pollak MR, Quaggin SE, Hoenig MP, Dworkin LD. The glomerulus: the sphere of influence. *Clin J Am Soc Nephrol.* 2014;9(8):1461-9.
125. Haraldsson B, Nyström J, Deen WM. Properties of the Glomerular Barrier and Mechanisms of Proteinuria. *Physiol Rev.* 2008;88(2):451-87.
126. Haraldsson B, Nyström J. The glomerular endothelium: new insights on function and structure. *Curr Opin Nephrol Hypertens.* 2012;21(3):258-63.
127. Miner JH. The glomerular basement membrane. *Exp Cell Res.* 2012;318(9):973-8.
128. Endlich K, Kriz W, Witzgall R. Update in podocyte biology. *Curr Opin Nephrol Hypertens.* 2001;10(3):331-40.
129. Menon MC, Chuang PY, He CJ. The glomerular filtration barrier: components and crosstalk. *Int J Nephrol.* 2012;2012:749010.
130. Bulger RE, Eknoyan G, Purcell DJ 2nd, Dobyan DC. Endothelial characteristics of glomerular capillaries in normal, mercuric chloride-induced, and gentamicin-induced acute renal failure in the rat. *J Clin Invest.* 1983;72(1):128-41.

References

131. Satchell SC, Braet F. Glomerular endothelial cell fenestrations: an integral component of the glomerular filtration barrier. *Am J Physiol Renal Physiol*. 2009;296(5):F947–56.
132. Curry FE, Adamson RH. Endothelial glycocalyx: permeability barrier and mechanosensor. *Ann Biomed Eng*. 2012;40(4):828–39.
133. Kanwar YS, Farquhar MG. Presence of heparan sulfate in the glomerular basement membrane. *Proc Natl Acad Sci U S A*. 1979;76(3):1303–7.
134. Kanwar YS, Danesh FR, Chugh SS. Contribution of proteoglycans towards the integrated functions of renal glomerular capillaries: a historical perspective. *Am J Pathol*. 2007;171(1):9–13.
135. Ogawa S, Ota Z, Shikata K, Hironaka K, Hayashi Y, Ota K, *et al*. High-Resolution Ultrastructural Comparison of Renal Glomerular and Tubular Basement Membranes. *Am J Nephrol*. 1999;19(6):686–93.
136. Pavenstädt H, Kriz W, Kretzler M. Cell Biology of the Glomerular Podocyte. *Physiol Rev*. 2003;83(1):253–307.
137. Reiser J, Altintas MM. Podocytes. *F1000Research*. 2016;5(F1000 Faculty Rev):114.
138. Fukasawa H, Bornheimer S, Kudlicka K, Farquhar MG. Slit diaphragms contain tight junction proteins. *Clin J Am Soc Nephrol*. 2009;20(7):1491–503.
139. Schlöndorff D, Banas B. The Mesangial Cell Revisited: No Cell Is an Island. *J Am Soc Nephrol*. 2009;20(6):1179–87.
140. Abboud HE. Mesangial cell biology. *Exp Cell Res*. 2012;318(9):979–85.
141. Lennon R, Hosawi S. Glomerular cell crosstalk. *Curr Opin Nephrol Hypertens*. 2016;25(3):187–93.
142. Choi CH, Zuckerman JE, Webster P, Davis ME. Targeting kidney mesangium by nanoparticles of defined size. *Proc Natl Acad Sci U S A*. 2011;108(16):6656–61.
143. Zuckerman JE, Choi CH, Han H, Davis ME. Polycation-siRNA nanoparticles can disassemble at the kidney glomerular basement membrane. *Proc Natl Acad Sci U S A*. 2012;109(8):3137–42.

144. Bennett KM, Zhou H, Sumner JP, Dodd SJ, Bouraoud N, Doi K, *et al.* MRI of the basement membrane using charged nanoparticles as contrast agents. *Magn Reson Med.* 2008;60(3):564–74.
145. Kodaira H, Tsutsumi Y, Yoshioka Y, Kamada H, Kaneda Y, Yamamoto Y, *et al.* The targeting of anionized polyvinylpyrrolidone to the renal system. *Biomaterials.* 2004;25(18):4309–15.
146. Lacerda L, Herrero MA, Venner K, Bianco A, Prato M, Kostarelos K. Carbon-Nanotube Shape and Individualization Critical for Renal Excretion. *Small.* 2008;4(8):1130–2.
147. Ruggiero A, Villa CH, Bander E, Rey DA, Bergkvist M, Batt CA, *et al.* Paradoxical glomerular filtration of carbon nanotubes. *Proc Natl Acad Sci U S A.* 2010;107(27):12369-74.
148. Kobayashi H, Kawamoto S, Saga T, Sato N, Hiraga A, Ishimori T, *et al.* Positive effects of polyethylene glycol conjugation to generation-4 polyamidoamine dendrimers as macromolecular MR contrast agents. *Magn Reson Med.* 2001;46(4):781–8.
149. Ogawa M, Regino CAS, Marcelino B, Williams M, Kosaka N, Bryant LH Jr., *et al.* New nano-sized biocompatible MR contrast agents based on lysine-dendri-graft macromolecules. *Bioconjug Chem.* 2010;21(5):955–60.
150. Longmire MR, Ogawa M, Choyke PL, Kobayashi H. Biologically optimized nanosized molecules and particles: more than just size. *Bioconjug Chem.* 2011;22(6):993-1000.
151. Kolset SO, Reinholt FP, Jenssen T. Diabetic Nephropathy and Extracellular Matrix. *J Histochem Cytochem.* 2012;60(12):976–86.
152. Neal CR. Podocytes ... What's Under Yours? (Podocytes and Foot Processes and How They Change in Nephropathy). *Front Endocrinol (Lausanne).* 2015;6:9.
153. Brunskill EW, Potter SS. Changes in the gene expression programs of renal mesangial cells during diabetic nephropathy. *BMC Nephrol.* 2012;13:70.
154. Scindia YM, Deshmukh US, Bagavant H. Mesangial pathology in glomerular disease: targets for therapeutic intervention. *Adv Drug Deliv Rev.* 2010;62(14):1337–43.

References

155. Pollinger K, Hennig R, Bauer S, Breunig M, Tessmar J, Buschauer A, *et al.* Biodistribution of Quantum Dots in the Kidney After Intravenous Injection. *J Nanosci Nanotechnol.* 2014;14(5):3313–9.
156. Li S, Zeng YC, Peng K, Liu C, Zhang ZR, Zhang L. Design and evaluation of glomerulus mesangium-targeted PEG-PLGA nanoparticles loaded with dexamethasone acetate. *Acta Pharmacol Sin.* 2019;40:143-50
157. Scindia Y, Deshmukh U, Thimmalapura PR, Bagavant H. Anti- α 8 integrin immunoliposomes in glomeruli of lupus-susceptible mice: a novel system for delivery of therapeutic agents to the renal glomerulus in systemic lupus erythematosus. *Arthritis Rheum.* 2008;58(12):3884–91.
158. Jin DK, Fish AJ, Wayner EA, Mauer M, Setty S, Tsilibary E, *et al.* Distribution of integrin subunits in human diabetic kidneys. *J Am Soc Nephrol.* 1996;7(12):2636–45.
159. Maile LA, Gollahon K, Wai C, Dunbar P, Busby W, Clemmons D. Blocking α V β 3 integrin ligand occupancy inhibits the progression of albuminuria in diabetic rats. *J Diabetes Res.* 2014;2014:421827.
160. Ásgeirsdóttir SA, Zwiers PJ, Morselt HW, Moorlag HE, Bakker HI, Heeringa P, *et al.* Inhibition of proinflammatory genes in anti-GBM glomerulonephritis by targeted dexamethasone-loaded AbEsel liposomes. *Am J Physiol Renal Physiol.* 2008;294(3):F554-F561.
161. Hans ML, Lowman AM. Biodegradable nanoparticles for drug delivery and targeting. *Curr Opin Solid State Mater Sci.* 2002;6(4):319–27.
162. Xiao RZ, Zeng ZW, Zhou GL, Wang JJ, Li FZ, Wang AM. Recent advances in PEG-PLA block copolymer nanoparticles. *Int J Nanomed.* 2010;5:1057–65.
163. Shin HC, Alani AW, Cho H, Bae Y, Kolesar JM, Kwon GS. A 3-in-1 Polymeric Micelle Nanocontainer for Poorly Water-Soluble Drugs. *Mol Pharm.* 2011;8(4):1257–65.
164. Wilkosz N, Łazarski G, Kovacik L, Gargas P, Nowakowska M, Jamróz D, *et al.* Molecular Insight into Drug-Loading Capacity of PEG–PLGA Nanoparticles for Itraconazole. *J Phys Chem B.* 2018;122(28):7080–90.
165. Fessi H, Puisieux F, Devissaguet JP, Ammoury N, Benita S. Nanocapsule formation by interfacial polymer deposition following solvent displacement. *Int J Pharm.* 1989;55(1):R1–R4.

166. Gu F, Zhang L, Teply BA, Mann N, Wang A, Radovic-Moreno AF, *et al.* Precise engineering of targeted nanoparticles by using self-assembled biointegrated block copolymers. *Proc Natl Acad Sci U S A.* 2008;105(7):2586–91.
167. Lim JM, Swami A, Gilson LM, Chopra S, Choi S, Wu J, *et al.* Ultra-High Throughput Synthesis of Nanoparticles with Homogeneous Size Distribution Using a Coaxial Turbulent Jet Mixer. *ACS Nano.* 2014;8(6):6056–65.
168. Valencia PM, Farokhzad OC, Karnik R, Langer R. Microfluidic technologies for accelerating the clinical translation of nanoparticles. *Nat Nanotechnol.* 2012;7(10):623-9.
169. Lim JM, Bertrand N, Valencia PM, Rhee M, Langer R, Jon S, *et al.* Parallel microfluidic synthesis of size-tunable polymeric nanoparticles using 3D flow focusing towards in vivo study. *Nanomedicine.* 2014;10(2):401–9.
170. Qian H, Wohl AR, Crow JT, Macosko CW, Hoye TR. A Strategy for Control of “Random” Copolymerization of Lactide and Glycolide: Application to Synthesis of PEG-b-PLGA Block Polymers Having Narrow Dispersity. *Macromolecules.* 2011;44(18):7132–40.
171. Bertrand N, Grenier P, Mahmoudi M, Lima EM, Appel EA, Dormont F, *et al.* Mechanistic understanding of in vivo protein corona formation on polymeric nanoparticles and impact on pharmacokinetics. *Nat Commun.* 2017;8(1):777.
172. Lee J, Cho EC, Cho K. Incorporation and release behavior of hydrophobic drug in functionalized poly(D,L-lactide)-block-poly(ethylene oxide) micelles. *J Control Release.* 2004;94(2):323–35.
173. Owen SC, Chan DPY, Shoichet MS. Polymeric micelle stability. *Nano Today.* 2012;7(1):53–65.
174. Brandl F, Bertrand N, Lima EM, Langer R. Nanoparticles with photoinduced precipitation for the extraction of pollutants from water and soil. *Nature Commun.* 2015;6:7765.
175. Xu Z, Lu C, Riordon J, Sinton D, Moffitt MG. Microfluidic Manufacturing of Polymeric Nanoparticles: Comparing Flow Control of Multiscale Structure in Single-Phase Staggered Herringbone and Two-Phase Reactors. *Langmuir.* 2016;32(48):12781-9.
176. Stroock AD, Dertinger SKW, Ajdari A, Mezić I, Stone HA, Whitesides GM. Chaotic Mixer for Microchannels. *Science.* 2002;295(5555):647–51.

References

177. Schubert S, Delaney JT Jr, Schubert US. Nanoprecipitation and nanoformulation of polymers: from history to powerful possibilities beyond poly(lactic acid). *Soft Matter*. 2011;7(5):1581–8.
178. Baby T, Liu Y, Middelberg APJ, Zhao CX. Fundamental studies on throughput capacities of hydrodynamic flow-focusing microfluidics for producing monodisperse polymer nanoparticles. *Chem Eng Sci*. 2017;169:128–39.
179. Pustulka KM, Wohl AR, Lee HS, Michel AR, Han J, Hoyer TR, *et al.* Flash Nanoprecipitation: Particle Structure and Stability. *Mol Pharm*. 2013;10(11):4367–77.
180. Zhu Z. Flash Nanoprecipitation: Prediction and Enhancement of Particle Stability via Drug Structure. *Mol Pharm*. 2014;11(3):776–86.
181. Wills JW, Summers HD, Hondow N, Soorash A, Meissner KE, White PA, *et al.* Characterizing Nanoparticles in Biological Matrices: Tipping Points in Agglomeration State and Cellular Delivery In Vitro. *ACS Nano*. 2017;11(12):11986–2000.
182. Monopoli MP, Walczyk D, Campbell A, Elia G, Lynch I, Baldelli Bombelli F, *et al.* Physical–Chemical Aspects of Protein Corona: Relevance to in Vitro and in Vivo Biological Impacts of Nanoparticles. *J Am Chem Soc*. 2011;133(8):2525–34.
183. Lynch I, Dawson KA. Protein-nanoparticle interactions. *Nano Today*. 2008;3(1):40–7.
184. Walczyk D, Baldelli Bombelli F, Monopoli MP, Lynch I, Dawson KA. What the Cell “Sees” in Bionanoscience. *J Am Chem Soc*. 2010;132(16):5761–8.
185. Wolfram J, Yang Y, Shen J, Moten A, Chen C, Shen H, *et al.* The nano-plasma interface: implications of the protein corona. *Colloids Surf B Biointerfaces*. 2014;124:17–24.
186. Yang ST, Liu Y, Wang YW, Cao A. Biosafety and Bioapplication of Nanomaterials by Designing Protein–Nanoparticle Interactions. *Small*. 2013;9(9–10):1635–53.
187. Shannahan JH, Lai X, Ke PC, Podila R, Brown JM, Witzmann FA. Silver Nanoparticle Protein Corona Composition in Cell Culture Media. *PLoS ONE*. 2013;8(9):e74001.
188. Tenzer S, Docter D, Kuharev J, Musyanovych A, Fetz V, Hecht R, *et al.* Rapid formation of plasma protein corona critically affects nanoparticle pathophysiology. *Nat Nanotechnol*. 2013;8:772–81.

189. Moore TL, Rodriguez-Lorenzo L, Hirsch V, Balog S, Urban D, Jud C, *et al.* Nanoparticle colloidal stability in cell culture media and impact on cellular interactions. *Chem Soc Rev.* 2015;44(17):6287–305.
190. Lee YK, Choi E-J, Webster TJ, Kim S-H, Khang D. Effect of the protein corona on nanoparticles for modulating cytotoxicity and immunotoxicity. *Int J Nanomed.* 2014;10:97–113.
191. Chen H, Kim S, He W, Wang H, Low PS, Park K, *et al.* Fast Release of Lipophilic Agents from Circulating PEG-PDLLA Micelles Revealed by in Vivo Förster Resonance Energy Transfer Imaging. *Langmuir.* 2008;24(10):5213–7.
192. Childs CE. The determination of polyethylene glycol in gamma globulin solutions. *Microchem J.* 1975;20(2):190–2.
193. Strojan K, Leonardi A, Bregar VB, Križaj I, Svete J, Pavlin M. Dispersion of Nanoparticles in Different Media Importantly Determines the Composition of Their Protein Corona. *PLoS ONE.* 2017;12(1):e0169552.
194. Aguilar-Castillo BA, Santos JL, Luo H, Aguirre-Chagala YE, Palacios-Hernández T, Herrera-Alonso M. Nanoparticle stability in biologically relevant media: influence of polymer architecture. *Soft Matter.* 2015;11(37):7296–307.
195. Rafiei P, Haddadi A. Docetaxel-loaded PLGA and PLGA-PEG nanoparticles for intravenous application: pharmacokinetics and biodistribution profile. *Int J Nanomed.* 2017;12:935–47.
196. Babcock JJ, Brancalion L. Bovine serum albumin oligomers in the E- and B-forms at low protein concentration and ionic strength. *Int J Biol Macromol.* 2013;53:42–53.
197. Fleischer CC, Payne CK. Nanoparticle–Cell Interactions: Molecular Structure of the Protein Corona and Cellular Outcomes. *Acc Chem Res.* 2014;47(8):2651–9.
198. Hirayama K, Akashi S, Furuya M, Fukuhara K-I. Rapid confirmation and revision of the primary structure of bovine serum albumin by ESIMS and frit-FAB LC/MS. *Biochem Biophys Res Commun.* 1990;173(2):639–46.
199. Satzer P, Svec F, Sekot G, Jungbauer A. Protein adsorption onto nanoparticles induces conformational changes: Particle size dependency, kinetics, and mechanisms. *Eng Life Sci.* 2015;16(3):238–46.

References

200. Brun E, Sicard-Roselli C. Could nanoparticle corona characterization help for biological consequence prediction? *Cancer Nanotechnol.* 2014;5(1):7.
201. Zou P, Chen H, Paholak HJ, Sun D. Noninvasive Fluorescence Resonance Energy Transfer Imaging of in Vivo Premature Drug Release from Polymeric Nanoparticles. *Mol Pharm.* 2013;10(11):4185–94.
202. Carrillo-Carrion C, Carril M, Parak WJ. Techniques for the experimental investigation of the protein corona. *Curr Opin Biotechnol.* 2017;46:106–13.
203. Anderson NL, Anderson NG. The Human Plasma Proteome. *Mol Cell Proteomics.* 2002;1(11):845-67.
204. Walkey CD, Chan WC. Understanding and controlling the interaction of nanomaterials with proteins in a physiological environment. *Chem Soc Rev.* 2012;41(7):2780–99.
205. Lu J, Owen SC, Shoichet MS. Stability of Self-Assembled Polymeric Micelles in Serum. *Macromolecules.* 2011;44(15):6002–8.
206. Li Y, Yang G, Mei Z. Spectroscopic and dynamic light scattering studies of the interaction between pterodonic acid and bovine serum albumin. *Acta Pharm Sin B.* 2012;2(1):53–9.
207. Renninger N, Knopp R, Nitsche H, Clark DS, Keasling JD. Uranyl Precipitation by *Pseudomonas aeruginosa* via Controlled Polyphosphate Metabolism. *Appl Environ Microbiol.* 2004;70(12):7404–12.
208. Scarff CA, Fuller MJG, Thompson RF, Iadaza MG. Variations on Negative Stain Electron Microscopy Methods: Tools for Tackling Challenging Systems. *J Vis Exp.* 2018;(132):57199.
209. Chithrani BD, Ghazani AA, Chan WCW. Determining the Size and Shape Dependence of Gold Nanoparticle Uptake into Mammalian Cells. *Nano Lett.* 2006;6(4):662–8.
210. Jiang W, Kim BYS, Rutka JT, Chan WCW. Nanoparticle-mediated cellular response is size-dependent. *Nat Nanotechnol.* 2008;3:145–50.
211. Shen Z, Nieh M-P, Li Y. Decorating Nanoparticle Surface for Targeted Drug Delivery: Opportunities and Challenges. *Polymers.* 2016;8(3):83.

212. Shuvaev VV, Ilies MA, Simone E, Zaitsev S, Kim Y, Cai S, *et al.* Endothelial Targeting of Antibody-Decorated Polymeric Filomicelles. *ACS Nano*. 2011;5(9):6991–9.
213. Yamamoto Y, Nagasaki Y, Kato Y, Sugiyama Y, Kataoka K. Long-circulating poly(ethylene glycol)–poly(d,l-lactide) block copolymer micelles with modulated surface charge. *J Control Release*. 2001;77(1-2):27–38.
214. Gref R, Lück M, Quellec P, Marchand M, Dellacherie E, Harnisch S, *et al.* ‘Stealth’ corona-core nanoparticles surface modified by polyethylene glycol (PEG): influences of the corona (PEG chain length and surface density) and of the core composition on phagocytic uptake and plasma protein adsorption. *Colloids Surf B Biointerfaces*. 2000;18(3-4):301–13.
215. Cruje C, Chithrani DB. Polyethylene glycol density and length affects nanoparticle uptake by cancer cells. *J Nanomed Res*. 2014;1(1):00006.
216. Miura Y, Takenaka T, Toh K, Wu S, Nishihara H, Kano MR, *et al.* Cyclic RGD-linked polymeric micelles for targeted delivery of platinum anticancer drugs to glioblastoma through the blood–brain tumor barrier. *ACS Nano*. 2013;7(10):8583–92.
217. Liu P, Qin L, Wang Q, Sun Y, Zhu M, Shen M, *et al.* cRGD-functionalized mPEG-PLGA-PLL nanoparticles for imaging and therapy of breast cancer. *Biomaterials*. 2012;33(28):6739–47.
218. Perry JL, Reuter KG, Kai MP, Herlihy KP, Jones SW, Luft JC, *et al.* PEGylated PRINT Nanoparticles: The Impact of PEG Density on Protein Binding, Macrophage Association, Biodistribution, and Pharmacokinetics. *Nano Lett*. 2012;12(10):5304–10.
219. Gambinossi F, Mylon SE, Ferri JK. Aggregation kinetics and colloidal stability of functionalized nanoparticles. *Adv Colloid Interface Sci*. 2015;222:332–49.
220. Abe K, Higashi K, Watabe K, Kobayashi A, Limwikrant W, Yamamoto K, *et al.* Effects of the PEG molecular weight of a PEG-lipid and cholesterol on PEG chain flexibility on liposome surfaces. *Colloids Surf A Physicochem Eng Asp*. 2015;474:63–70.
221. Arjonen A, Alanko J, Veltel S, Ivaska J. Distinct recycling of active and inactive β 1 integrins. *Traffic*. 2012;13(4):610–25.
222. De Franceschi N, Hamidi H, Alanko J, Sahgal P, Ivaska J. Integrin traffic - the update. *J Cell Sci*. 2015;128(5):839–52.

References

223. Li Y, Kröger M, Liu WK. Endocytosis of PEGylated nanoparticles accompanied by structural and free energy changes of the grafted polyethylene glycol. *Biomaterials*. 2014;35(30):8467–78.
224. Zhdanov VP. Multivalent ligand-receptor-mediated interaction of small filled vesicles with a cellular membrane. *Phys Rev E*. 2017;96(1-1):012408.
225. Zhdanov VP. Physical aspects of the initial phase of endocytosis. *Phys Rev E Stat Nonlin Soft Matter Phys*. 2013;88(6):064701.
226. Shang L, Nienhaus K, Jiang X, Yang L, Landfester K, Mailänder V, *et al*. Nanoparticle interactions with live cells: Quantitative fluorescence microscopy of nanoparticle size effects. *Beilstein J Nanotechnol*. 2014;5:2388–97.
227. Tang H, Ye H, Zhang H, Zheng Y. Wrapping of nanoparticles by the cell membrane: the role of interactions between the nanoparticles. *Soft Matter*. 2015;11(44):8674–83.
228. Stefanick JF, Ashley JD, Kiziltepe T, Bilgicer B. A systematic analysis of peptide linker length and liposomal polyethylene glycol coating on cellular uptake of peptide-targeted liposomes. *ACS Nano*. 2013;7(4):2935–47.
229. Duskey JT, Rice KG. Nanoparticle Ligand Presentation for Targeting Solid Tumors. *AAPS PharmSciTech*. 2014;15(5):1345–54.
230. Parveen N, Rimkute I, Block S, Rydell GE, Midtvedt D, Larson G, *et al*. Membrane Deformation Induces Clustering of Norovirus Bound to Glycosphingolipids in a Supported Cell-Membrane Mimic. *J Phys Chem Lett*. 2018;9(9):2278–84.
231. Sancey L, Garanger E, Foillard S, Schoehn G, Hurbin A, Albiges-Rizo C, *et al*. Clustering and Internalization of Integrin $\alpha(v)\beta(3)$ With a Tetrameric RGD-synthetic Peptide. *Mol Ther*. 2009;17(5):837–43.
232. Barua S, Mitragotri S. Challenges associated with Penetration of Nanoparticles across Cell and Tissue Barriers: A Review of Current Status and Future Prospects. *Nano Today*. 2014;9(2):223–43.
233. Hennig R, Ohlmann A, Staffel J, Pollinger K, Haunberger A, Breunig M, *et al*. Multivalent nanoparticles bind the retinal and choroidal vasculature. *J Control Release*. 2015;220:265–74.

234. Liu J, Agrawal NJ, Calderon A, Ayyaswamy PS, Eckmann DM, Radhakrishnan R. Multivalent Binding of Nanocarrier to Endothelial Cells under Shear Flow. *Biophys J* 2011;101(2):319–26.
235. Fasting C, Schalley CA, Weber M, Seitz O, Hecht S, Kokschi B, *et al.* Multivalency as a Chemical Organization and Action Principle. *Angew Chem, Int Ed.* 2012;51(42):10472–98.
236. Hild W, Pollinger K, Caporale A, Cabrele C, Keller M, Pluym N, *et al.* G protein-coupled receptors function as logic gates for nanoparticle binding and cell uptake. *Proc Natl Acad Sci U S A.* 2010;107(23):10667–72.
237. Hennig R, Vesper A, Kirchhof S, Goepferich A. Branched Polymer–Drug Conjugates for Multivalent Blockade of Angiotensin II Receptors. *Mol Pharm.* 2015;12(9):3292–302.
238. Ma X, Xiong Y, Lee LTO. Application of Nanoparticles for Targeting G Protein-Coupled Receptors. *Int J Mol Sci.* 2018;19(7):E2006.
239. Ruoslahti E, Bhatia SN, Sailor MJ. Targeting of drugs and nanoparticles to tumors. *J Cell Biol.* 2010;188(6):759–68.
240. Xu Q, Liu Y, Su S, Li W, Chen C, Wu Y. Anti-tumor activity of paclitaxel through dual-targeting carrier of cyclic RGD and transferrin conjugated hyperbranched copolymer nanoparticles. *Biomaterials.* 2012;33(5):1627–39.
241. Stockand JD, Sansom SC. Glomerular Mesangial Cells: Electrophysiology and Regulation of Contraction. *Physiol Rev.* 1998;78(3):723–44.
242. Kirchhof S, Brandl F, Hammer N, Goepferich AM. Investigation of the Diels–Alder reaction as a cross-linking mechanism for degradable poly(ethylene glycol) based hydrogels. *J Mater Chem B.* 1:4855–64.
243. Russo MA, Paolillo M, Sanchez-Hernandez Y, Curti D, Ciusani E, Serra M, *et al.* A small-molecule RGD-integrin antagonist inhibits cell adhesion, cell migration and induces anoikis in glioblastoma cells. *Int J Oncol.* 2013;42(1):83–92.
244. Grynkiewicz G, Poenie M, Tsien RY. A new generation of Ca²⁺ indicators with greatly improved fluorescence properties. *J Biol Chem.* 1985;260(6):3440–50.
245. Kobori H, Mori H, Masaki T, Nishiyama A. Angiotensin II Blockade and Renal Protection. *Curr Pharm Des.* 2013;19(17):3033–42.

References

246. Anderson LR, Owens TW, Naylor MJ. Integrins in development and cancer. *Biophys Rev.* 2013;6(2):191–202.
247. Desgrosellier JS, Cheresh DA. Integrins in cancer: biological implications and therapeutic opportunities. *Nat Rev Cancer.* 2010;10(1):9–22.
248. Kreidberg JA, Symons JM. Integrins in kidney development, function, and disease. *Am J Physiol Renal Physiol.* 2000;279(2):F233–42.
249. Fierensa FLP, Vanderheyden PML, Roggeman C, De Backer JP, Thekkumkara TJ, Vauquelin G. Tight binding of the angiotensin AT₁ receptor antagonist [³H]candesartan is independent of receptor internalization. *Biochem Pharmacol.* 2001;61(10):1227–35.
250. Hein L, Meinel L, Pratt RE, Dzau VJ, Kobilka BK. Intracellular Trafficking of Angiotensin II and its AT₁ and AT₂ Receptors: Evidence for Selective Sorting of Receptor and Ligand. *Mol Endocrinol.* 1997;11(9):1266–77.
251. Oparil S. Newly Emerging Pharmacologic Differences in Angiotensin II Receptor Blockers. *Am J Hypertens* 2000;13(1 Pt 2):18S–24S.
252. Vanderheyden PML, Fierens FLP, Vauquelin G, Verheijen I. The In Vitro Binding Properties of Non-Peptide AT₁ Receptor Antagonists. *J Clin Basic Cardiol.* 2002;5(1):75–82.
253. Burnier M, Brunner HR. Angiotensin II receptor antagonists. *Lancet* 2000;355(9204):637–45.
254. Mire DE, Silfani TN, Pugsley MK. A Review of the Structural and Functional Features of Olmesartan Medoxomil, An Angiotensin Receptor Blocker. *J Cardiovasc Pharmacol.* 2005;46(5):585–93.
255. Santella JB, Duncia JV, Ensinger CL, VanAtten MK, Carini DJ, Wexler RR, *et al.* Balanced angiotensin II receptor antagonists. III. The effects of substitution at the imidazole 5-position. *Bioorg Med Chem Lett.* 1994;4(18):2235–40.
256. Carpenter KA, Wilkes BC, Schiller PW. The octapeptide angiotensin II adopts a well-defined structure in a phospholipid environment. *Eur J Biochem.* 2001;251(1-2):448–53.
257. Cayrol F, Díaz Flaqué MC, Fernando T, Yang SN, Sterle HA, Bolontrade M, *et al.* Integrin $\alpha\beta 3$ acting as membrane receptor for thyroid hormones mediates angiogenesis in malignant T cells. *Blood.* 2015;125(5):841–51.

258. Modery-Pawlowski CL, Gupta AS. Heteromultivalent ligand-decoration for actively targeted nanomedicine. *Biomaterials*. 2014;35(9):2568–79.
259. Qiu H, Rieger J, Gilbert B, Jérôme R, Jérôme C. PLA-Coated Gold Nanoparticles for the Labeling of PLA Biocarriers. *Chem Mater*. 2004;16(5):850–6.
260. Li S-D, Huang L. Pharmacokinetics and Biodistribution of Nanoparticles. *Mol Pharm*. 2008;5(4):496–504.
261. Banerjee SR, Foss CA, Horhota A, Pullambhatla M, McDonnell K, Zale S, *et al*. 111In- and IRDye800CW-Labeled PLA-PEG Nanoparticle for Imaging Prostate-Specific Membrane Antigen-Expressing Tissues. *Biomacromolecules*. 2017;18(1):201–9.
262. Johnstone S, Ansell S, Xie S, Mayer L, Tardi P. The use of radioactive marker as a tool to evaluate the drug release in plasma and particle biodistribution of block copolymer nanoparticles. *J Drug Deliv*. 2011;2011:349206.
263. Wu J, Zhao J, Zhang B, Qian Y, Gao H, Yu Y, *et al*. Polyethylene glycol-poly(lactide acid) nanoparticles modified with cysteine-arginine-glutamic acid-lysine-alanine fibrin-homing peptide for glioblastoma therapy by enhanced retention effect. *Int J Nanomed*. 2014;9:5261–71.
264. Shalgunov V, Zaytseva-Zotova D, Zintchenko A, Levada T, Shilov Y, Andreyev D, *et al*. Comprehensive study of the drug delivery properties of poly(l-lactide)-poly(ethylene glycol) nanoparticles in rats and tumor-bearing mice. *J Control Release*. 2017;261:31–42.
265. Mieszawska AJ, Gianella A, Cormode DP, Zhao Y, Meijerink A, Langer R, *et al*. Engineering of lipid-coated PLGA nanoparticles with a tunable payload of diagnostically active nanocrystals for medical imaging. *Chem Commun (Camb)*. 2012;48(47):5835–7.
266. Sailor MJ, Park J-H. Hybrid Nanoparticles for Detection and Treatment of Cancer. *Adv Mater*. 2012;24(28):3779–802.
267. Liu Y, Tseng Y-C, Huang L. Biodistribution studies of nanoparticles using fluorescence imaging: a qualitative or quantitative method? *Pharm Res*. 2012;29(12):3273–7.

References

268. Yang J, Lee J, Kang J, Oh SJ, Ko HJ, Son JH, *et al.* Smart Drug-Loaded Polymer Gold Nanoshells for Systemic and Localized Therapy of Human Epithelial Cancer. *Adv Mater.* 2009;21(43):4339–42.
269. He X, Gao J, Gambhir SS, Cheng Z. Near-infrared fluorescent nanoprobes for cancer molecular imaging: status and challenges. *Trends Mol Med.* 2010;16(12):574–83.
270. Jong WH, Burger MC, Verheijen MA, Geertsma RE. Detection of the Presence of Gold Nanoparticles in Organs by Transmission Electron Microscopy. *Materials (Basel).* 2010;3(9):4681–94.
271. Chen Y, Dai J, Morris JG Jr, Johnson JA. Genetic analysis of the capsule polysaccharide (K antigen) and exopolysaccharide genes in pandemic *Vibrio parahaemolyticus* O3:K6. *BMC Microbiol.* 2010;10(1):274.
272. Schneider G, Decher G, Nerambourg N, Praho R, Werts MHV, Blanchard-Desce M. Distance-Dependent Fluorescence Quenching on Gold Nanoparticles Ensheathed with Layer-by-Layer Assembled Polyelectrolytes. *Nano Lett.* 2006;6(3):530–6.
273. Weipoltshammer K, Schöfer C, Almeder M, Wachtler F. Signal enhancement at the electron microscopic level using Nanogold and gold-based autometallography. *Histochem Cell Biol.* 2000;114(6):489–95.
274. Otsuki Y, Maxwell LE, Magari S, Kubo H. Immunogold-silver staining method for light and electron microscopic detection of lymphocyte cell surface antigens with monoclonal antibodies. *J Histochem Cytochem.* 1990;38(8):1215–21.
275. Tiwari PM, Eroglu E, Bawage SS, Vig K, Miller ME, Pillai S, *et al.* Enhanced intracellular translocation and biodistribution of gold nanoparticles functionalized with a cell-penetrating peptide (VG-21) from vesicular stomatitis virus. *Biomaterials.* 2014;35(35):9484–94.
276. Dulkeith E, Morteaux AC, Niedereichholz T, Klar TA, Feldmann J, Levi SA, *et al.* Fluorescence Quenching of Dye Molecules near Gold Nanoparticles: Radiative and Nonradiative Effects. *Phys Rev Lett.* 2002;89(20):203002.
277. Cheng J, Teply BA, Sherifi I, Sung J, Luther G, Gu FX, *et al.* Formulation of functionalized PLGA-PEG nanoparticles for in vivo targeted drug delivery. *Biomaterials.* 2006;28(5):869–76.

278. Pelet JM, Putnam D. An In-Depth Analysis of Polymer-Analogous Conjugation using DMTMM. *Bioconjug Chem.* 2011;22(3):329–37.
279. Zhang K, Yi J, Chen D. Bimodal porous superparticles with the optimized structure prepared by self-limited aggregation of PEG-coated mesoporous nanofibers for purification of protein-dye conjugates. *J Mater Chem A.* 2013;1:14649–57.
280. Li M, Cushing SK, Wang Q, Shi X, Hornak LA, Hong Z, *et al.* Size-Dependent Energy Transfer between CdSe/ZnS Quantum Dots and Gold Nanoparticles. *J Phys Chem Lett.* 2011;2(17):2125–9.
281. Novo C, Funston AM, Pastoriza-Santos I, Liz-Marzán LM, Mulvaney P. Influence of the Medium Refractive Index on the Optical Properties of Single Gold Triangular Prisms on a Substrate. *J Phys Chem C.* 2008;112(1):3–7.
282. Makadia HK, Siegel SJ. Poly Lactic-co-Glycolic Acid (PLGA) as Biodegradable Controlled Drug Delivery Carrier. *Polymers (Basel).* 2011;3(3):1377–97.
283. Koley D, Bard AJ. Triton X-100 concentration effects on membrane permeability of a single HeLa cell by scanning electrochemical microscopy (SECM). *Proc Natl Acad Sci U S A.* 2010;107(39):16783–7.
284. Budkina OA, Demina TV, Dorodnykh TY, Melik-Nubarov NS, Grozdova ID. Cytotoxicity of nonionic amphiphilic copolymers. *Polym Sci Ser A.* 2012;54(9):707–17.
285. Loumagne M, Praho R, Nutarelli D, Werts MHV, Débarre A. Fluorescence correlation spectroscopy reveals strong fluorescence quenching of FITC adducts on PEGylated gold nanoparticles in water and the presence of fluorescent aggregates of desorbed thiolate ligands. *Phys Chem Chem Phys.* 2010;12(36):11004–14.
286. Lim SY, Kim JH, Lee JS, Park CB. Gold Nanoparticle Enlargement Coupled with Fluorescence Quenching for Highly Sensitive Detection of Analytes. *Langmuir.* 2009;25(23):13302–5.
287. Singh MP, Strouse GF. Involvement of the LSPR Spectral Overlap for Energy Transfer between a Dye and Au Nanoparticle. *J Am Chem Soc.* 2010;132(27):9383–91.
288. Chatterjee S, Lee JB, Valappil NV, Luo D, Menon VM. Investigating the distance limit of a metal nanoparticle based spectroscopic ruler. *Biomed Opt Express.* 2011;2(6):1727–33.

References

289. Bhowmick S, Saini S, Shenoy VB, Bagchi B. Resonance energy transfer from a fluorescent dye to a metal nanoparticle. *J Chem Phys.* 2006;125(18):181102.
290. Jennings TL, Singh MP, Strouse GF. Fluorescent Lifetime Quenching near $d = 1.5$ nm Gold Nanoparticles: Probing NSET Validity. *J Am Chem Soc.* 2006;128(16):5462–7.
291. Malatesta M, Pellicciari C, Cisterna B, Costanzo M, Galimberti V, Biggiogera M, *et al.* Tracing nanoparticles and photosensitizing molecules at transmission electron microscopy by diaminobenzidine photo-oxidation. *Micron.* 2013;59:44–51.
292. Owen GR, Meredith DO, Ap Gwynn I, Richards RG. Enhancement of immunogold-labelled focal adhesion sites in fibroblasts cultured on metal substrates: Problems and solutions. *Cell Biol Int.* 2013;25(12):1251–9.
293. Elci SG, Yan B, Kim ST, Saha K, Jiang Y, Klemmer GA, *et al.* Quantitative imaging of 2 nm monolayer-protected gold nanoparticle distributions in tissues using laser ablation inductively-coupled plasma mass spectrometry (LA-ICP-MS). *Analyst.* 2016;141:2418–25.
294. Reul R, Tsapis N, Hillaireau H, Sancey L, Mura S, Recher M, *et al.* Near infrared labeling of PLGA for in vivo imaging of nanoparticles. *Polym Chem.* 2012;3:694–702.

Appendix

Supplementary Data

A) Supplementary data to chapter 4

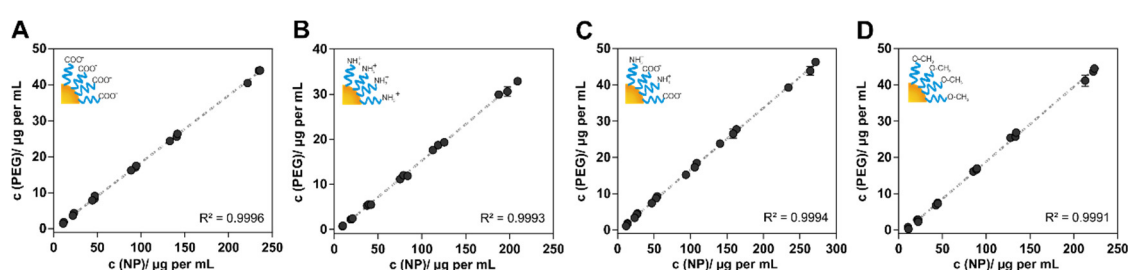


Figure S1. Determination of the NP concentration by an iodine assay. The linear correlation of PEG content and total polymer concentration of (A) NP510C, (B) NP510N, (C) NP510CN and (D) NP510m allows for an absorbance based quantification of PLA-PEG/PLGA NPs.

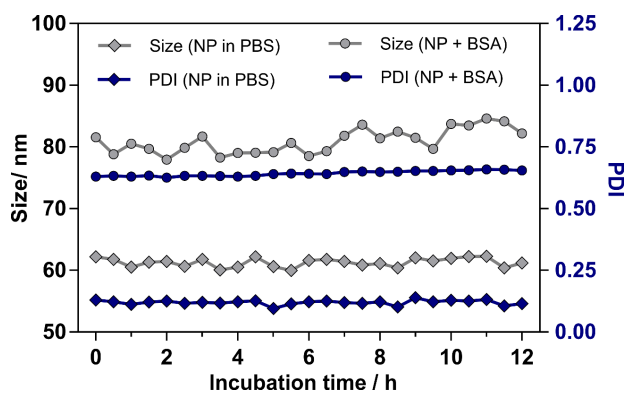


Figure S2. Particle size and PDI of NP510N in either DPBS pH 7.4 (diamonds) or DPBS supplemented with 45 mg mL⁻¹ BSA (circles). NP samples were incubated at 37 °C for up to 12 hours and size was measured in 0.5 h intervals.

B) Supplementary data to chapter 5

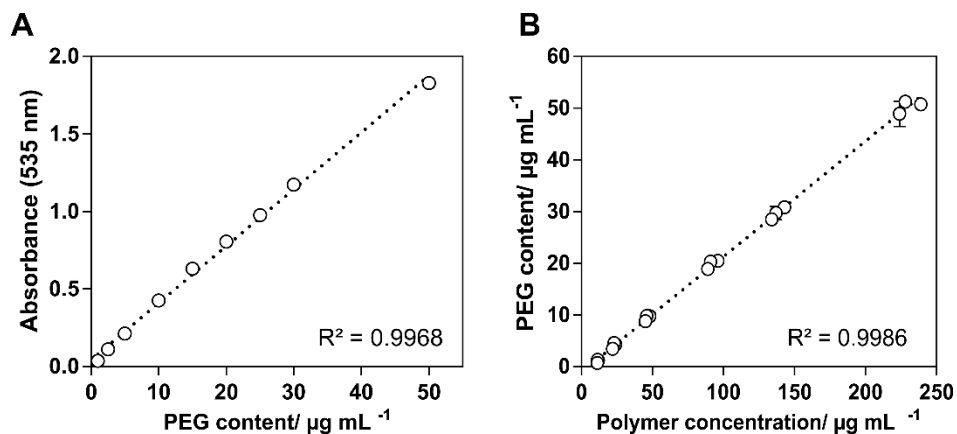


Figure S3: Determination of NP concentration using an iodine complexation assay. (A) Absorbance intensity as a function of PEG content (1-50 µg mL⁻¹). (B) The linear correlation of polymer concentration in formulated NPs (PLA-PEG-COOH, 10k-b-5k and PLGA at a mass ratio of 70/30) and PEG content allows for a quantification of the NP concentration. Since NPs with different block copolymers (PLA-PEG-COOH, 10k-b-3.5k and 10k-b-2k) were prepared using a constant ratio of PLA-PEG to PLGA molarity, NP concentrations of NP-cRGD-5k, NP-cRGD-3.5k and NP-cRGD-2k were adjusted to equal PEG molarities (based on Mw_(PEG) provided by material specification sheets).

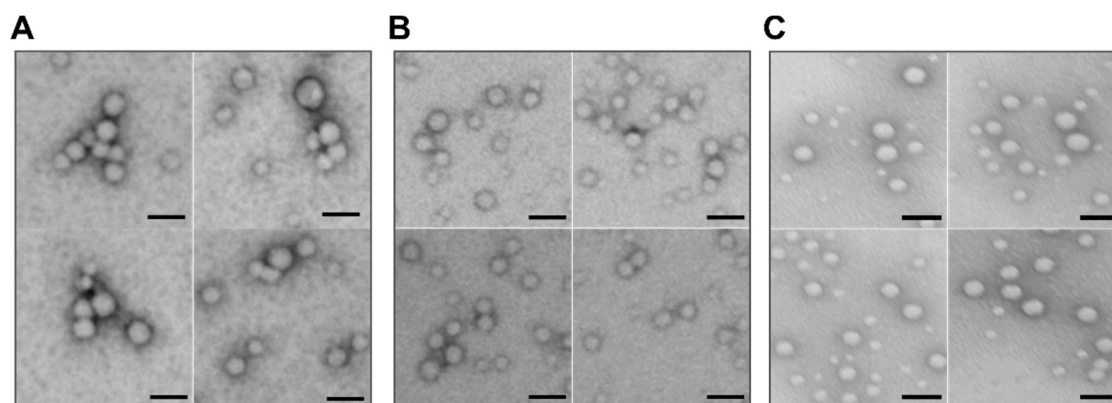


Figure S4: TEM image of cRGD-decorated NPs with different PEG-linker lengths: (A) 2 kDa, (B) 3.5 kDa, (C) 5 kDa. Particle size and aggregation tendency increased with decreasing PEG-linker length. Scale bar indicates 200 nm.

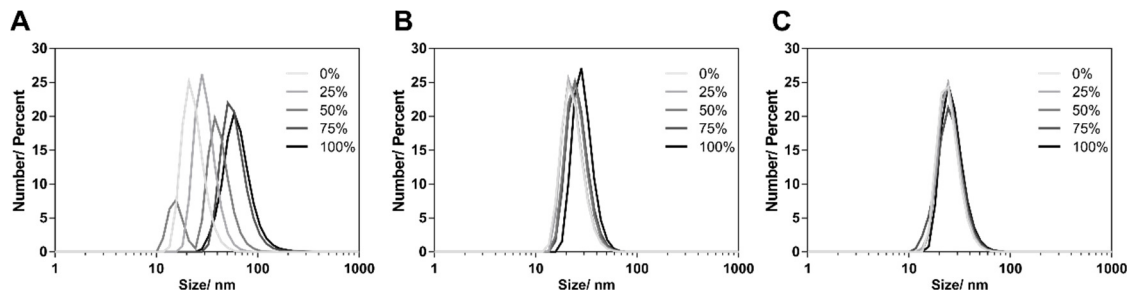


Figure S5. Number-weighted particle size distribution of (A) NP-cRGD-2k, (B) NP-cRGD-3.5k and (C) NP-cRGD-5k with different ligand densities (0-100 %) determined by DLS. Preparation of targeted NPs with shorter PEG-linkers resulted in an increase in nanoparticle size and a broader particle size distribution.

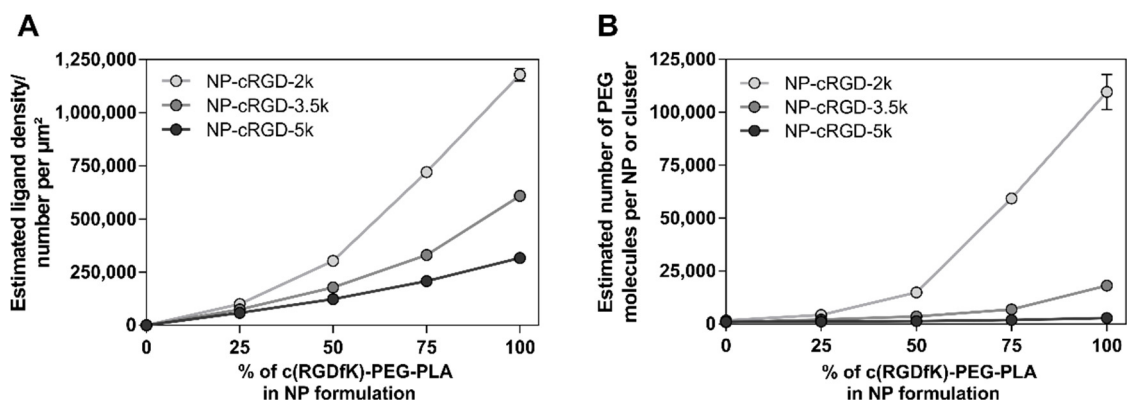


Figure S6. Quantification of targeted NP surface composition. (A) Estimated ligand density expressed as number of ligands per μm^2 and (B) estimated number of ligands per NP or cluster. Values were calculated based on the number of functionalized-PEG molecules of each formulation and the z-average size of NPs and colloidal clusters.

Appendix

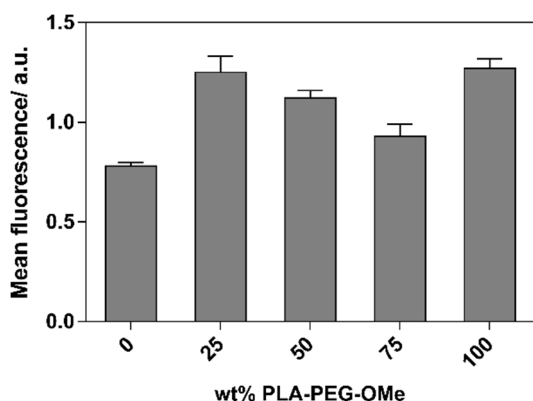


Figure S7. Cellular uptake of NPs consisting of a constant amount of PLGA and different ratios of PLA-PEG-COOH and PLA-PEG-OMe. The charged carboxylic acid groups were gradually substituted by uncharged methoxy-groups leading to control NPs with varying surface charge. All NP formulations were prepared and handled as described for cRGD-decorated NPs. Independent of their charge, all five control NP formulations did not bind to integrin receptor on U87MG cells.

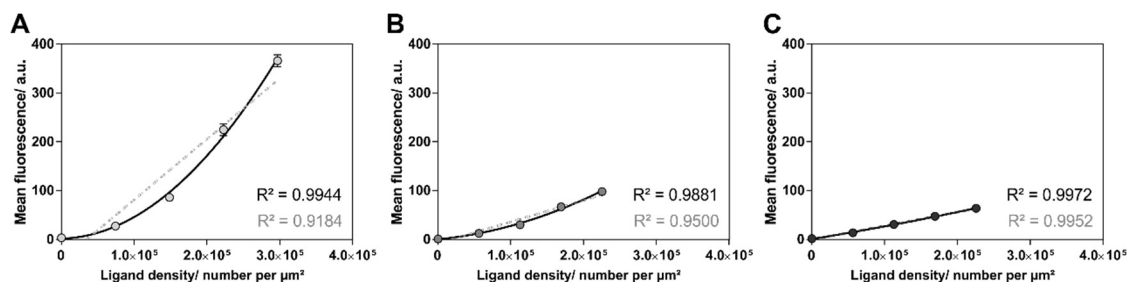


Figure S8. Mean cell-associated fluorescence as a function of ligand density of (A) NP-cRGD-2k, (B) NP-cRGD-3.5k and (C) NP-cRGD-5k. The ligand density was calculated based on the grafting density of non-modified NP-cRGD₀-2k, NP-cRGD₀-3.5k and NP-cRGD₀-5k multiplied with the respective surface functionalization degree (%) as determined by PCA. Changes in particle size and rearrangement of PEG linkers upon cluster formation were not taken into consideration. Data were fitted with a first (dotted light grey line) and second order (solid dark grey line) polynomial.

Table S1: Absolute ligand densities (number per μm^2) of different NP formulations were correlated with corresponding cell-associated fluorescence levels. Data were fitted with second order polynomial.

NP formulation	First order polynomial fit	R ²
NP-cRGD-2k	$y = -2.054 + 0.0003116x$	0.9970
NP-cRGD-3.5k	$y = 2.498 + 0.0001645x$	0.9732
NP-cRGD-5k	$y = 3.332 + 0.0001995x$	0.9877

Table S2: First order polynomial fit of uptake kinetics.

NP formulation	First order polynomial 15-120 min	R ²	First order polynomial 15-180 min	R ²
NP-cRGD ₁₀₀ -2k	$y = 33.36 + 4.745x$	0.9999	$y = 57.37 + 4.255x$	0.9925
NP-cRGD ₁₀₀ -3.5k	$y = 24.48 + 1.195x$	0.9998	$y = 32.15 + 1.038x$	0.9873
NP-cRGD ₁₀₀ -5k	$y = 11.11 + 0.9720x$	0.9998	$y = 24.34 + 0.7014x$	0.9230
NP-cRGD ₀ -5k	$y = 0.2965 + 0.04739x$	0.9985	$y = 0.4018 + 0.04523x$	0.9982

C) Supplementary data to chapter 7

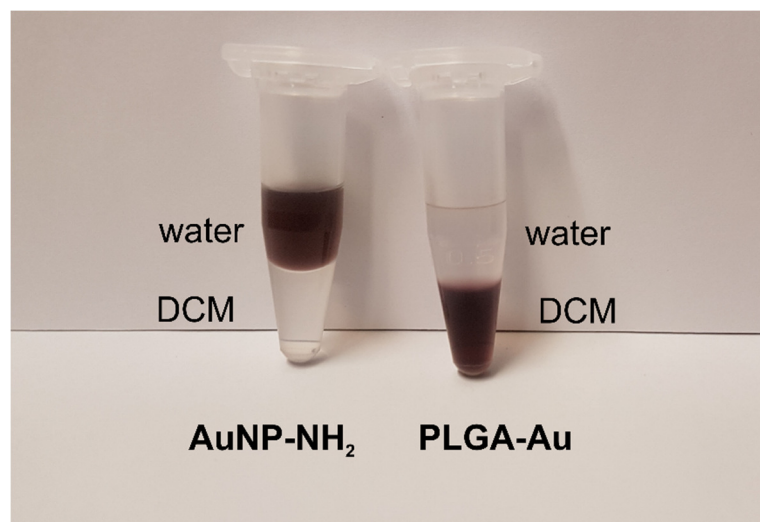
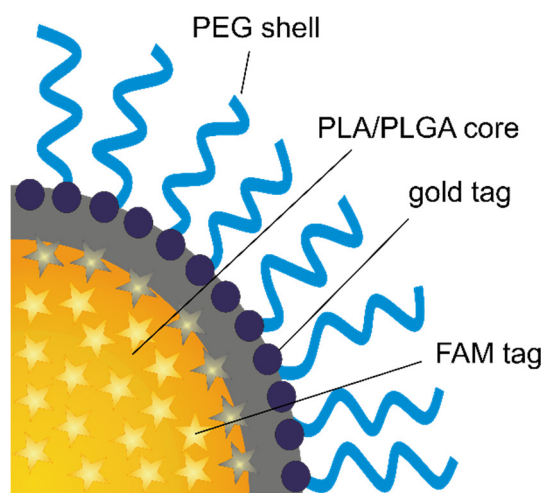


Figure S9. Partitioning of AuNP-NH₂ before (left) and after (right) covalent conjugation to PLGA in water and dichloromethane. Unconjugated AuNP-NH₂ were primarily present in the aqueous phase, whereas PLGA-Au conjugates were primarily present to the organic phase.



FAM fluorescence ET

Figure S10. Scheme illustrating the structure of fluorescent and gold labeled NPs. The grey area indicates the maximum distance of energy transfer. Most of the fluoresceinamine molecules inside the NP core are spared from quenching due to the long distance from the gold particles.

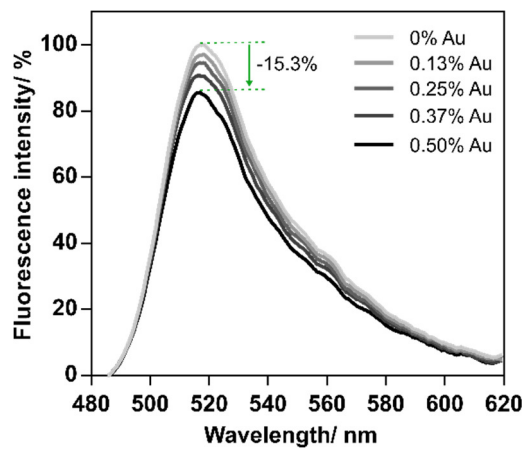


Figure S11. Fluorescence intensity of fluorescein-labeled NPs as a function of gold content. The contents of PLA-PEG-MeO and PLGA-FAM were kept constant at 60.0% and 13.3% (m/m), respectively, whereas PLGA-Au (27.7%) was gradually replaced by unlabeled PLGA (0, 25, 50, 75, 100% referring to PLGA-Au) to manufacture NP with gold contents of 0, 0.13, 0.25, 0.38, 0.50 wt%. NP-associated fluorescence was excited at 460 nm and spectra were recorded between 485 and 620 nm. Spectra smoothing was performed using a Savitzky-Golay polynomial.

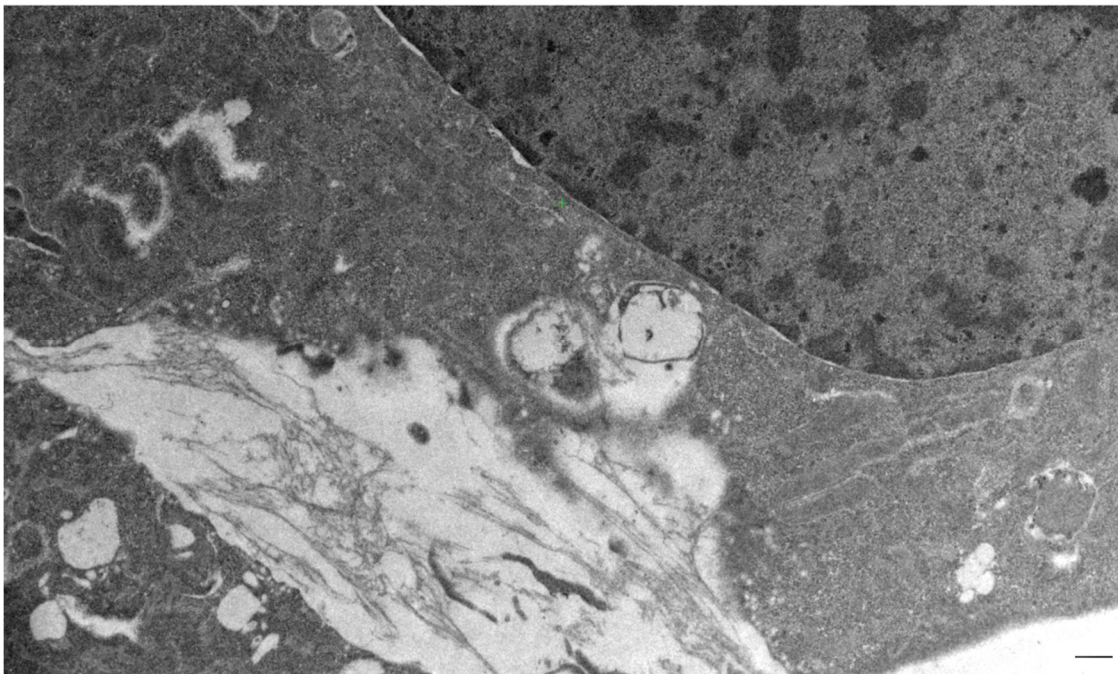


Figure S12. TEM image of untreated rat mesangial cells after gold enhancement. Control cells did not form intracellular vesicles and showed no formation of gold deposits caused by nonspecific auto-nucleation during gold enhancement. Scale bar indicates 500 nm.

Appendix

Table S3: Calculation of the relative gold content in different hybrid NP formulations determined by ICP-OES.

NP formulation	Gold content		NP content		Mass (Au) per mass (NP)	Gold content
	ppm ⁽¹⁾	mg mL ⁻¹ ⁽²⁾	mg ⁽³⁾	mg mL ⁻¹ ⁽⁴⁾	μg mg ⁻¹ ⁽⁵⁾	% ⁽⁶⁾
Polymeric NPs (no gold) [#]	0.12	0.00012	7.92	1.58	0.07	0.01
	0.11	0.00011	7.92	1.58	0.07	0.01
	0.12	0.00012	7.92	1.58	0.07	0.01
	0.13	0.00013	7.92	1.58	0.08	0.01
	0.09	0.00009	7.92	1.58	0.06	0.01
Hybrid NPs	13.67	0.01367	9.15	1.83	7.47	0.75
	13.62	0.01362	9.15	1.83	7.44	0.74
	13.73	0.01373	9.15	1.83	7.50	0.75
	13.74	0.01374	9.15	1.83	7.51	0.75
	13.92	0.01392	9.15	1.83	7.61	0.76
cRGD-decorated polymeric NPs (no gold) [#]	0.19	0.00019	8.05	1.61	0.12	0.01
	0.17	0.00017	8.05	1.61	0.11	0.01
	0.14	0.00014	8.05	1.61	0.08	0.01
	0.14	0.00014	8.05	1.61	0.09	0.01
	0.12	0.00012	8.05	1.61	0.07	0.01
cRGD-decorated hybrid NPs	5.60	0.00560	5.73	1.15	4.89	0.49
	5.66	0.00566	5.73	1.15	4.94	0.49
	5.76	0.00576	5.73	1.15	5.03	0.50
	5.83	0.00583	5.73	1.15	5.09	0.51
	5.73	0.00573	5.73	1.15	5.00	0.50

⁽¹⁾ Determined by ICP-OES, ⁽²⁾ Calculated as gold concentration in 1 mL of sample solution, ⁽³⁾ Weighed out after lyophilization, ⁽⁴⁾ Calculated as NP concentration in 5 mL of sample solution, ⁽⁵⁾ Calculated as mass of gold per mass of NP, ⁽⁶⁾ Gold content in NP formulation.

[#] Unlabeled NPs were used as blanks to determine the background signal of respective hybrid NP samples.

Abbreviations

ACN	acetonitrile
ANOVA	analysis of variance
Anx	anginex
APS	ammonium persulfate
ARB	angiotensin receptor blocker
AT ₁ R	angiotensin II receptor type I
AuNP	gold nanoparticle
BME	2-Mercaptoethanol
BP	band pass
BSA	bovine serum albumin
CDCl ₃	deuterated chloroform
CE	conjugation efficiency
cyclo(RGDfK)	cyclo(Arg-Gly-Asp-D-Phe-Lys)
CLSM	confocal laser scanning microscopy
DABCO	1,4-Diazabicyclo[2.2.2]octane hydrochloride
DBU	1,8-Diazabicyclo[5.4.0]undec-7-ene
DCM	dichloromethane
DLS	dynamic light scattering
DiD	1,1'-dioctadecyl-3,3,3',3'-tetramethylindodicarbocyanine perchlorate

Appendix

DiI	1,1'-Dioctadecyl-3,3,3',3'-tetramethylindocarbocyanine perchlorate
DiO	3,3'-dioctadecyloxacarbocyanine perchlorate
DIPEA	N,N-Diisopropylethylamine
DMEM	Dulbecco's modified Eagle's medium
DMF	N,N-Dimethylformamide
DMSO	dimethyl sulfoxide
DN	diabetic nephropathy
D ₂ O	deuterium oxide
DPBS	Dulbecco's phosphate buffered saline
EC ₅₀	half maximal effective concentration
EC ₈₀	concentration that leads to 80% of the maximum response
EDC	N-(3-dimethylaminopropyl)-N'-ethylcarbodiimide hydrochloride
EGF	epidermal growth factor
EGTA	ethylene glycol-bis(2-aminoethylether)-N,N,N',N'-tetraacetic acid
EMEM	Eagle's minimal essential medium
EPR	enhanced permeation and retention
ESRD	end-stage renal disease
FACS	fluorescence activated cell sorting
FAM	fluoresceinamine
FCS	fetal calf serum
FRET	fluorescence resonance energy transfer
FRR	flow rate ratio
GBM	glomerular basement membrane
GFB	glomerular filtration barrier

Abbreviations

GPCR	G protein-coupled receptor
HA	hemagglutinin
HC	hard corona
IA	iodine complexation assay
IC ₅₀	half maximal inhibitory concentration
LA-ICP-MS	laser ablation inductively-coupled plasma mass spectrometry
ICP-MS	inductively coupled plasma mass spectrometry
ICP-OES	inductively coupled plasma optical emission spectroscopy
LP	long pass
LSPR	localized surface plasmon resonance
mAb	monoclonal antibody
MPS	mononuclear phagocyte system
MTT	3-(4,5-dimethylthiazol-2-yl)-2,5-diphenyltetrazolium bromide
MW	molecular weight
NA	neuraminidase
NHS	N-hydroxysuccinimide
NP	nanoparticle
NSET	nanometal surface energy transfer
ntNP	non-targeted nanoparticles
PC	protein corona
PCA	9,10-phenanthrenequinone assay
PDI	polydispersity index
PEG	poly(ethylene glycol)
PFA	paraformaldehyde
PLA	poly(lactic acid)
PLGA	poly(lactic- <i>co</i> -glycolic acid)

Appendix

ppb	parts per billion
ppm	parts per million
PVP	polyvinylpyrrolidone
RAAS	renin-angiotensin-aldosteron system
Re	Reynold's number
RES	reticuloendothelial system
RGD	(Arg-Gly-Asp)
RT	room temperature
SC	soft corona
SDS	sodium dodecyl sulfate
SDS-PAGE	sodium dodecyl sulfate-polyacrylamide gel electrophoresis
SFD	surface functionalization degree
SPR	surface plasmon resonance
TEM	transmission electron microscopy
TEMED	tetramethylethylenediamin
TFA	trifluoroacetic acid
TFR	total flow rate
TMS	tetramethylsilane
TMSP	3-(Trimethylsilyl)propionic-2,2,3,3-d4 acid sodium salt

Curriculum Vitae

Personal Information

Name: Kathrin Irene Abstiens
Date of birth: 7th of September 1988
Place of birth: Schwaebisch Gmuend
Nationality: German

Professional Training

11/2013 – 09/2017 **Graduate Student**
Department of Pharmaceutical Technology,
University of Regensburg

01/2014 – 04/2017 **Specialist Pharmacist in Pharmaceutical Technology**
Department of Pharmaceutical Technology,
University of Regensburg

12/2013 **Licensure as Pharmacist**

05/2013 - 10/2013 **Practical Training**
Marien Apotheke, Moosburg

10/2012 - 04/2013 **Practical Training**
Department of Biomedical Engineering,
Cornell University, Ithaca, NY, USA

10/2007 - 10/2012 **Studies of Pharmacy**
Ludwig-Maximilian University of Munich
Joint degree with Pharmaceutical Sciences (B.Sc./M.Sc.)

10/2007 - 10/2010 **Studies of Pharmaceutical Sciences (M.Sc.)**
Ludwig-Maximilian University of Munich
Master's thesis: "*Application of Microscale Thermophoresis for Protein Formulation Development*" supervised by Prof. Dr. Gerhard Winter

Curriculum Vitae

10/2010 - 04/2012 **Studies of Pharmaceutical Sciences (B.Sc.)**
Ludwig-Maximilian University of Munich
Bachelor's thesis: "*Chlorinated carbazole-1-carboxylic acid amides as potential kinase inhibitors*" supervised by Prof. Dr. Franz Bracher

Scientific Work Experience

11/2018 – Present **Scientist/ Pharmaceutical Project Leader**
Late-Stage Pharmaceutical and Processing
Development, F. Hoffmann-La Roche, Basel,
Switzerland

01/2018 - 09/2018 **Postdoc/ QC Specialist**
Biocenter of Excellence, Quality Control Aseptics,
Novartis Pharma, Stein AG, Switzerland

07/2012 - 09/2012 **Research Intern**
NanoTemper Technologies, Munich

04/2012 - 08/2012 **Undergraduate Research Assistant**
Institute of Stem Cell Research, Helmholtz Center
Munich

10/2011 - 03/2012 **Master's Thesis**
NanoTemper Technologies, Munich

07/2011 - 12/2011 **Undergraduate Research Assistant**
Beckman Coulter Biomedical, Munich

05/2010 - 03/2011 **Undergraduate Research Assistant**
Walther-Straub-Institute for Pharmacology and
Toxicology, Munich

Education

06/2007 **Abitur**

09/1999 - 06/2007 **Grammar School**
Karl-Ritter-von-Frisch-Gymnasium, Moosburg

List of Publications

Peer-reviewed publications

1. Abstiens Kathrin, Goepferich Achim. Microfluidic manufacturing improves polydispersity of multicomponent polymeric nanoparticles. *J. Drug Deliv. Sci. Technol.* 2019, 49:433-439. (**Chapter 3**)
2. Abstiens Kathrin, Maslanka Figueroa Sara, Gregoritzka Manuel, Goepferich Achim. Interaction of functionalized nanoparticles with serum proteins and its impact on colloidal stability and cargo leaching. *Soft Matter* 2019, 15:709-720 (**Chapter 4**)
3. Abstiens Kathrin, Gregoritzka Manuel, Goepferich Achim. Ligand density and linker length are critical factors for multivalent nanoparticle–receptor interactions. *ACS Appl. Mater. Interfaces* 2019, 11(1):1311-1320 (**Chapter 5**)
4. Abstiens Kathrin, Fleischmann Daniel, Gregoritzka Manuel, Goepferich Achim M. Spatially-controlled hybrid nanoparticles with enhanced detectability in biological environments. *Accepted in ACS Appl. Nano Mater.* 2019 (**Chapter 7**)
5. Maslanka Figueroa Sara, Abstiens Kathrin, Veser Anika, Fleischmann Daniel, Beck Sebastian, Goepferich Achim. Influenza A Virus Mimetic Nanoparticles Trigger Selective Cell Uptake. *Submitted for publication*
6. Gregoritzka Manuel, Abstiens Kathrin, Graf Moritz, Goepferich Achim M. Fabrication of antibody-loaded microgels using microfluidics and thiol-ene photoclick chemistry. *Eur. J. Pharm. Biopharm.* 2018, 127(17):194-203.
7. Gregoritzka Manuel, Messmann Viktoria, Abstiens Kathrin, Brandl Ferdinand P., Goepferich Achim M. Controlled antibody release from degradable thermoresponsive hydrogels cross-linked by Diels-Alder chemistry. *Biomacromolecules* 2017; 18(8):2410-2418.

Conference abstracts

1. Maslanka Figueroa Sara, Abstiens Kathrin, Goepferich Achim M. Angiotensin I-decorated nanoparticles target mesangial cells after enzymatic activation. *11th World Meeting on Pharmaceutics, Biopharmaceutics and Pharmaceutical Technology*, Granada, Spain, 2018.
2. Beck Sebastian, Abstiens Kathrin, Goepferich Achim M. In vitro evaluation of multivalent binding nanoparticles for the treatment of neovascularization in the eye. *11th World Meeting on Pharmaceutics, Biopharmaceutics and Pharmaceutical Technology*, Granada, Spain, 2018.
3. Abstiens Kathrin, Goepferich Achim M. Synthesis and characterization of hybrid gold/polymer nanoparticles for biomedical applications. *254th ACS National Meeting*, Washington DC, USA, 2017.
4. Abstiens Kathrin, Liebl Renate, Goepferich Achim M. Influence of ligand density, concentration and incubation time on uptake efficiency of c(RGDfK)-decorated polymeric nanoparticles. *2nd European Conference on Pharmaceutics*, Krakow, Poland, 2017.
5. Abstiens Kathrin, Goepferich Achim M. Interaction of functionalized PEG-PLA/PLGA nanoparticles with serum proteins and impact on nanoparticle stability and cell toxicity. *10th World Biomaterials Congress*, Montréal, Canada, 2016.
6. Abstiens Kathrin, Goepferich Achim M. Microfluidic synthesis improves polydispersity of PLGA blended PEG-PLA nanoparticles. *10th World Meeting on Pharmaceutics, Biopharmaceutics and Pharmaceutical Technology*, Glasgow, UK, 2016

Acknowledgements

First and foremost, I would like to express my sincerest gratitude to Prof. Dr. Achim Göpferich for giving me the opportunity to be part of his research group and for committing this engaging project to me. I am deeply thankful for all his time and support, for providing an outstanding working environment and for the opportunity to attend several international conferences. I appreciate all his contributions of time and ideas to make my PhD experience productive and stimulating.

Furthermore, I express my deepest gratitude to all of my colleagues in the research group of the Department of Pharmaceutical Technology. They created an atmosphere of companionship and made the past few years a highly memorable time. In this regard a special 'thank you' goes out for the following colleagues:

My lab mate Dr. Vanessa Haas for the great time and a very harmonious atmosphere in the lab, our climbing adventures and for her genuine friendship.

Alexandra Haunberger for the many great training sessions in the gym, many unforgettable 'Gin and Stenz Eis sessions' and for her genuine friendship.

Sara Maslanka Figueroa and Sebastian Beck for inspiring and motivating conversations in- and outside the lab.

I furthermore thank Eva Wrobel for her excellent organizational skills and her excellent restaurant recommendations.

Moreover, I thank Renate Liebl, Viktoria Messmann, Angelika Berié, Edith Schindler and Stefan Kolb for their excellent technical assistance and for many delightful coffee sessions. I also thank Andrea Blaimer for her great support with the AFL practical course.

I further thank Margit Schimmel for her technical assistance with the electron microscope.

Acknowledgements

The German Research Foundation (DFG) is acknowledged for providing financial support for my project.

The international PhD program at the University of Regensburg (iPUR) is acknowledged for providing funding for the attendance at the international conference in Montréal.

My greatest thanks go to Manu. Thank you for always being there for me, for your never ending encouragement, all your support, your patience and your love.

Finally, I want to thank my family for their unconditional love, their infinite support and for encouraging me to follow this path.

Statement in Lieu of an Oath

I hereby confirm that I have written this thesis on my own and that I have not used any other media or materials than the ones referred to in this thesis.

Basel, 30.11.2018

.....

(Kathrin Abstiens)